DESIGN AND SYNTHESIS OF STABLE, ALIGNED AND WELDED MAGNESIUM SILICIDE NANOWIRE ASSEMBLIES FOR FABRICATION OF EFFICIENT AND RELIABLE THERMOELECTRICS

A Dissertation

by

VENKATA RAVI KIRAN VASIRAJU

Submitted to the Office of Graduate and Professional Studies of
Texas A&M University
in partial fulfillment of the requirements for the degree of

DOCTOR OF PHILOSOPHY

Chair of Committee,	Sreeram Vaddiraju
Committee Members,	Ibrahim Karaman
	Arun Srinivasa
	Mustafa Akbulut
Head of Department,	Ibrahim Karaman

December 2016

Major Subject: Materials Science and Engineering

ABSTRACT

The ever-increasing energy needs of humanity, coupled with geopolitics of fossil fuels, are imposing demand on the energy supply. A perennial supply of energy is possible by tapping into renewable sources as well as making the current process more efficient. This can be achieved via the use of thermoelectrics, i.e. they can be used to generate energy by converting sunlight into electricity via solar thermoelectrics and increase the efficiency of current processes by converting the wasted heat into electricity. However, the current state-of-the-art thermoelectrics are inefficient and expensive due to the use of rare earth materials.

Nanomaterials, especially nanowires, are on the forefront of advancement in thermoelectrics. Recent theoretical and experimental reports indicate the superior energy conversion performances of nanowires compared to their bulk counter parts. However, this superior performance is only observed in single-nanowire devices. Despite more than two decades of research, macro-devices based on large-scale nanowire assemblies, have not been realized. The three main roadblocks for fabricating such large-scale assemblies are lack of 1) methods for mass producing nanowires of any desired chemical composition, 2) techniques for assembling these nanowires into energy conversion devices in an interface engineered manner, and 3) techniques to stabilize the nanowires at higher temperatures against air- water- and acid-assisted degradation. In this context, the objective of this work is to design a strategy to obtain stable and efficient nanowire-based thermoelectric devices. The material systems chosen for this effort are Zinc Phosphide Zn_3P_2, Magnesium Silicide, Mg_2Si, and Manganese Silicide $MnSi_{1.75}$.

Methods for mass production of Zn_3P_2 and Mg_2Si nanowires have been realized previously via a combination of chemical vapor deposition, electroless etching and solid-state diffusion. The assembly and aligning of nanowires was achieved using shear forces via Equal Channel Angular Extrusion (a severe plastic deformation technique). Assembly of the nanowires was also achieved via welding of nanowires utilizing the solid-state diffusion. The nanowires were chemically stabilized by nonconformally decorating them with boron nitride. The stabilization and welding of nanowires helped to achieve decreased thermal conductivity thereby improving their thermoelectric performance compared to the as-obtained nanowire pellets.

ACKNOWLEDGEMENTS

I would like to sincerely thank my advisor, Dr. Sreeram Vaddiraju, for his constant and consistent help, encouragement, and support throughout my doctoral program. It was a great learning opportunity for me to conduct this research under his guidance. He helped me not only as a mentor but also as a friend. I also would like to thank my committee members, Dr. Ibrahim Karaman, Dr. Arun Srinivasa, and Dr. Mustafa Akbulut, for their guidance and support throughout the course of this research. I also extended my gratitude to Dr. Rakesh Agrawal from Purdue who also guided me through the end phase of my doctoral work.

Additionally, I would like to thank my past and current lab mates, Dr. Lance Brockway, Dr. Yongmin Kang, Mr. Jinmoo Lee, Mr. Pranav Kannan, Mr. Azhar Ali, Mr. Yixi Chen, Mr. Rakesh Polinnaya and Mr. Nirup Nagabandi, for their cooperation and friendship throughout my research. In addition, thanks to NSF/DOE thermoelectrics partnership (CBET# 1048702) program for financial support. I would also like extend my appreciation to Texas A&M Institute of Advanced Study (TIAS), which provided me financial support via the HEEP fellowship.

Finally, thanks to my mother Parvathi and father Vishwanadham for their encouragement and patience.

NOMENCLATURE

C_p	Heat Capacity
CVD	Chemical Vapor Deposition
D	Diameter
DSC	Differential Scanning Calorimetry
ECAE	Equal Channel Angular Extrusion
EDS	Energy Dispersive Spectroscopy
E_g	Band-gap
FTIR	Fourier-transform Infrared Spectroscopy
HF	Hydrofluoric Acid
k_B	Boltzmann’s Constant
L	Lorenz Number
LFA	Laser Flash Analyzer
LLNL	Lawrence Livermore National Laboratory
m_e	Theoretical Electron Mass
m^*	Effective Electron Mass
n	Carrier Concentration
NW	Nanowire
P	Pressure
S	Seebeck Coefficient
SAED	Small Angle Electron Diffraction
SEM	Scanning Electron Microscopy

T	Temperature
TE	Thermoelectric
TEG	Thermoelectric Generator
TEM	Transmission Electron Microscopy
UV-Vis	Ultra-violet/Visible Spectroscopy
XRD	X-ray Diffraction
zT	Dimensionless Thermoelectric Figure of Merit
α	Thermal Diffusivity
κ	Total Thermal Conductivity
κ_l	Lattice Thermal Conductivity
κ_e	Electronic Thermal Conductivity
ρ	Density
σ	Electrical Conductivity
υ	Phonon Group Velocity
l	Phonon Mean Free Path.

TABLE OF CONTENTS

Page

ABSTRACT ii

ACKNOWLEDGEMENTS iv

NOMENCLATURE v

TABLE OF CONTENTS vii

LIST OF FIGURES x

LIST OF TABLES xvi

CHAPTER I INTRODUCTION 1

- Introduction to thermoelectrics 3
  - Thermoelectrics for energy conversion 6
  - A case for efficient and cost effective thermoelectric materials 8
  - Materials for thermoelectrics 9
  - History of thermoelectrics 10
  - Magnesium silicide for thermoelectrics 11

CHAPTER II LITERATURE REVIEW 13

- Nanowires for thermoelectrics 14
  - zT enhancement due to quantum confinement 15
  - Thermal engineering in nanowires for enhanced zT 17
- Previous work on nanowires 18
  - Power factor enhancement 18
  - Thermal investigations 19
  - Investigations on nanowire arrays 21
- Material selection criteria 23
  - Zinc phosphide 24
  - Manganese and magnesium silicides 26

CHAPTER III PROBLEM STATEMENT AND HYPOTHESIS 31

- Hypothesis 33
- Goals 35

CHAPTER IV MASS PRODUCTION OF ZINC PHOSPHIDE SILICON AND MAGNESIUM SILICIDE NANOWIRES 37

Mass production of Zn_3P_2 and ZnO nanowires 37
Mass production of contaminant free silicon nanowires 41
  Silver removal from nanowire surfaces 41

CHAPTER V SIMULTANEOUS ALIGNMENT AND CONSOLIDATION OF RIGID NANOWIRES VIA SHEAR FORCE USING EQUAL CHANNEL ANGULAR EXTRUSION 45

Introduction 46
Materials and methods 50
Results and discussion 53
Conclusions 61

CHAPTER VI STABILITY ENHANCEMENT OF ZINC PHOSPHIDE, ZINC OXIDE AND MAGNESIUM SILICIDE NANOWIRES VIA NONCONFORMAL BORON NITRIDE DECORATION 63

Introduction 63
Experimental methods 66
Results and discussion 68
Conclusions 82

CHAPTER VII THERMAL ENGINEERING IN NANOWIRE AND MICRON PARTICLE ASSEMBLIES VIA NONCONFORMAL BN DECORATION 84

Introduction 84
Experimental methods 87
Results and discussion 89
Conclusions 98

CHAPTER VIII THERMOELECTRIC PROPERTIES OF STABILIZED MANGANESE SILICIDE AND WELDED MAGNESIUM SILICIDE 100

Introduction 100
Experimental methods 101
  Fabrication of welded Mg_2Si nanowire pellets 101
  Fabrication of BN decorated $MnSi_{1.75}$ micron pellets 103
Results and discussion 104
  Thermoelectric characterization 109
Conclusion 113

CHAPTER IX CONCLUSIONS 115

CHAPTER X FUTURE WORK 119

REFERENCES 123

APPENDIX A: THERMAL CONDUCTIVITY IN NANOWIRES 161

  Matthiessen's rule 161
  Deviation from mathession rule: 163
  Temperature dependence on thermal conductivity 164
  Widemann-Franz law 165
  Phonon and electron confinement in silicon nanowires 165

APPENDIX B: ROLE OF CONTAMINATION IN SILICON NANOWIRES 167

LIST OF FIGURES

Page

Figure 1 Increase in the rate of energy over the century as predicted by LLNL[1] 2

Figure 2 Expected energy demand in the future and the contribution of fossil fuels to the supply.[1] 3

Figure 3 Spaghetti diagram showing the various sources of energy generation in United States in 2013. It is notable that from 97.4 quads of energy generated in the U.S. 59 Quads (about 60%) of energy is wasted as rejected heat energy.[1] 4

Figure 4 A schematic of the first experiments done by Seebeck to discover Seebeck effect[6] 5

Figure 5 A schematic shown a) the Seebeck effect and b) the Peltier effect 5

Figure 6 Calculated zT vs efficiency for various hot side temperature, the cold side temperature is 300K 7

Figure 7 Thermoelectric figures of merit for (a) n-type and (b) p-type state of art materials.[7] Reprinted by permission from Macmillan Publishers Ltd: *Nat. Mater*. 2008, *7*, 105-114 9

Figure 8 A schematic showing the relation between seebeck coefficient, electrical conductivity, thermal conductivity and zT with respect to the career concentration of a material[7] Reprinted by permission from Macmillan Publishers Ltd: *Nat. Mater.* 2008, *7*, 105-114 13

Figure 9 zT vs year, showing the slow increase in zT before 2000 and increase in zT due to nanostructuring[14, 27, 28, 51, 56-61] 15

Figure 10 Density of states of (a) bulk material and (b) nanowires.[65] Reproduced with permission from WILEY-VCH Verlag GmbH & Co. 16

Figure 11 (a) The plot showing an increase in power factor as the diameter of the nanowire according to the Hicks – Dresselhaus in which only one sub-band is considered and (b) plot showing the change of power factor then an increase with decreasing nanowire diameter as per the calculations done by Rabin in which 300 sub-bands were considered.[63, 64] 17

Figure 12 A schematic showing a nanowire array based thermoelectric device.[88] Reproduced with permission from TMS, 2012 22

Figure 13 zT per dollar value for prominent thermoelectric materials. The yellow bar shows the zT/cost value of the current state of the material. The green bar and the red bars shows the achieved and expected zT/cost value of thermoelectric materials composed of earth abundant. The cost of the compounds were calculated from elemental costs provided in USGS 2013 survey.[29, 33, 54, 80, 94] 24

Figure 14 The tetragonal crystal structure of zinc phosphide.[100] Reprinted from, Elrod et al., Journal of Crystal Growth 1984, 67, 195-201., with permission from Elsevier 28

Figure 15 Nowotny chimney-ladder structure of higher manganese silicide.[101] Reprinted by permission from Macmillan Publishers Ltd: *Nature Communications* 2015, *6*, 6723. 29

Figure 16 Schematic showing the fields in which advances are needed to achieve materials with commercialization of thermoelectrics for domestic applications 32

Figure 17 Schematic of 3 zone furnace for chemical vapor deposition chamber of elemental phosphorous onto rolled zinc foil for production of Zn_3P_2 nanowires 38

Figure 18 The scanning electron micrograph of the zinc phosphide nanowires synthesized by reacting the (a) zinc foil with elemental red phosphorous to result in (b) a completely converted foil with (c) nanowires of 20 – 50 nm in diameter.[127] Reproduced from Physical Chemistry Chemical Physics 2013, 15, 6260-6267 with permission of The Royal Society of Chemistry. 39

Figure 19 Schematic of silicon nanowire synthesis from a single crystalline (100) silicon wafer by etching in a solution of hydrofluoric acid and silver nitrate 40

Figure 20 Scanning electron micrograph showing the a) top view and b) crossectional view of silicon nanowires fibricated via electroless etching. High resolution TEM images showing single crystalline nanowires with c) [110] and d) [100] growth directions.[125] Reprinted from Materials Letters 2013, 100, 106-110., with permission from Elsevier 43

Figure 21 Silicon nanowires obtained from electroless etching of single crystalline (100) silicon wafers 43

Figure 22 SEM image and corresponding EDS spectrum of particles observed on top of consolidated and aligned nanowire pellets. The particle is primarily composed of silver contaminant, a by-product obtained during the electroless etching of silicon wafers into nanowires 44

Figure 23 A schematic showing the basic working of equal channel angular extrusion 50

Figure 24 Schematic representing (a) ECAE experimental setup, (b) billet used for the ECAE experimentation, and (c) steps involved in Route A processing of nanowires.. 53

Figure 25 Optical micrographs representing all the steps involved in the simultaneous consolidation and alignment of nanowires using ECAE. (a) Raw materials used for consolidating and aligning nanowires, including copper billet, silicon nanowire powders and copper rods, (b) billet containing the copper nanowires before ECAE, (c) copper billets after ECAE processing, and (d) silicon pellet obtained by the ECAE. 55

Figure 26 Scanning electron micrographs of (a) as-obtained nanowires, (b) and (c) as-obtained aligned and consolidated nanowires obtained by ECAE, and (d) aligned and consolidated silicon nanowires after grain boundary etching. Images shown in (b) and (c) are obtained from consolidated and silicon nanowire pellets. 58

Figure 27 A schematic representing the mechanism proposed to explain the mechanical robustness of the consolidated and aligned nanowire pellets. The interlocking of the rough surfaces of the electroless etched nanowires is believed to be responsible for the robustness of the pellets 60

Figure 28 SEM image and corresponding EDS spectrum of particles observed on top of consolidated and aligned nanowire pellets. The particle is primarily composed of silver contaminant, a by-product obtained during the electroless etching of silicon wafers into nanowires 61

Figure 29 Scanning electron micrographs of (a) pristine Zn_3P_2 nanowires and (b) BN decorated Zn_3P_2 nanowires. No changes to the morphologies or the dimensions of the nanowires were observed after they were decorated with BN. (c) XRD spectra of both pristine and BN decorated Zn_3P_2 nanowires. In both the cases, the nanowires exhibited the α-Zn_3P_2 phase. Peaks corresponding to zinc foil substrate employed for the synthesis of nanowires are indicated with a * in the figure. Transmission electron micrographs and the corresponding SAED patterns of (d) a pristine and (e) a BN decorated Zn_3P_2 nanowire. TEM analysis also indicated that the nanowires exhibited [101] growth direction. 71

Figure 30 Scanning electron micrographs of BN decorated Zn_3P_2 nanowires (a) after they were treated in DI water and (b) HCl solution of pH 3. The nanowires retained their morphologies in both the cases. (c) and (d) SEM of pristine Zn_3P_2 nanowires after treatment with DI water and pH 3 HCl solution. Complete degradation of the pristine Zn_3P_2 nanowires was observed in both the cases. (e) XRD spectra of BN decorated Zn_3P_2 nanowires after they are treated with DI water and pH 3 HCl solution. Peaks corresponding to zinc foil substrate employed for the synthesis of nanowires are indicated with a * in the figure. (f) TEM micrograph of a BN decorated Zn_3P_2 nanowire after it was treated in pH 3 HCl solution. 73

Figure 31 FTIR spectrum of BN decorated Zn_3P_2 nanowires indicating the presence of BN. For comparison, FTIR spectrum of decomposed B-tribromoborazine source is also included. 75

Figure 32 The proposed structure of BN decorated Zn_3P_2 nanowires. Exposure of Zn_3P_2 nanowires to a vapor of decomposed B-tribromoborazine is expected to lead to BN molecule getting embedded within the surfaces/sub-surfaces of the nanowires and the formation of BN decorated Zn3P2 nanowires........76

Figure 33 A Tauc plot of both pristine Zn_3P_2 nanowires and BN decorated Zn_3P_2 nanowires. The plot indicted no change in the Eg of Zn_3P_2 nanowires on decoration with BN molecules. The Eg of both pristine and BN decorated Zn_3P_2 nanowires remained 1.55 eV. 78

Figure 34 (a) (a) Scanning electron micrographs of (a) as-obtained ZnO nanowires, (b) as-obtained ZnO nanowires after treatment with pH 3 HCl solution, (c) BN decorated ZnO nanowires, and (d) BN decorated ZnO nanowires after pH 3 HCl solution treatment. From the micrographs, it is clear, beyond doubt, that BN decoration of ZnO nanowires imparted them stability against acid-assisted degradation. (e) Tauc plot of both pristine and BN decorated ZnO nanowires. The plot indicated that the decoration process did not majorly alter the Eg of ZnO nanowires. 79

Figure 35 Scanning electron micrographs of (a) as-obtained Mg_2Si nanowires, (b) as-obtained Mg_2Si nanowires after acid treatment, (c) BN surface decorated Mg_2Si nanowires, and (d) BN surface decorated Mg_2Si nanowires after acid treatment. It is very clear from the figure (b) and (d) that BN surface decoration imparted resistance against acid-assisted degradation to Mg_2Si nanowires. (e) Raman spectra of the nanowires indicating that the nanowires are indeed composed of Mg_2Si and that they retained the same composition after BN decoration and acid treatment. 81

Figure 36 SEM images of (a) unfunctionalized Zn_3P_2 nanowires and (b) BN decorated Zn_3P_2 nanowires. No changes in morphologies or dimensions were observed in the nanowires. (c) XRD spectra of both pristine and BN decorated nanowires show the presence of the same phases. 90

Figure 37 A plot indicating the temperature variation of the thermal conductivities of the Zn_3P_2 nanowires, Zn_3P_2 nanowire-BN composites and Zn_3P_2 nanowire-BN hybrids. The hybrids exhibited lowest thermal conductivities of all the samples tested. 92

Figure 38 A plot indicating the temperature variation of the thermal conductivities of the microinterfaces between Zn_3P_2 nanowire and BN microparticles in composites, and nanointerfaces between Zn_3P_2 nanowire-BN nanodomains on their surfaces in the hybrids.. 97

Figure 39 A plot indicating the temperature variation of the thermal conductivities of the CuO micropowder, CuO micropowder-BN composites and CuO micropowder-BN hybrids. Similar to the case of Zn3P2 nanowires, the hybrids exhibited lowest thermal conductivities 98

Figure 40 Temperature profile for solid state diffusion of magnesium into silicon nanowires for fabrication of magnesium silicide nanowires. 103

Figure 41 Scanning electron microscopy of (a) silica decorated silicon nanowires and (b) phase tranformed magnesium silicide nanopartciles decorated magnesium silicide nanowires. 105

Figure 42 (a) Optical micrograph of Mg_2Si nanowire pressed pellets (b) Scanning electron micrograph of pressed nanowire pellet and (c) X-ray diffraction spectra of both welded and unwelded nanowires. The (*) represents the carbon peaks a reminant of pressing... 106

Figure 43 Scanning microscopy of (a) crushed and ball-milled silicon micron powder and (b) phase transformed manganese silicide micron powders. The X-ray-diffraction spectroscopy of converted manganese silicide and BN decorated show the higher manganese silicide phase. In addition, some peaks of silicon are also observed in both the pellets. The (*) indicates silicon peaks which indicate incomplete transformation of silicon micron particles to HMS. 108

Figure 44 Thermoelectric properties of welded and unwelded magnesium silicide nanowire networks a) seebeck vs temperature b) conductivity vs temperature c) thermal conductivity w.r.t. temperature and d) the thermoelectric figure of merit with respect to temperature 110

Figure 45 Thermoelectric characterization of $MnSi_{1.75}$ and $BN\_MnSi_{1.75}$ a) seebeck vs temperature b) conductivity vs temperature c) thermal conductivity w.r.t. temperature and d) the thermoelectric figure of merit with respect to temperature 112

Figure 46 Dependence of thermal conductivity on a) roughness of the nanowire for a given nanowire diameter and b) Diameter of the nanowire for a given roughness value.[299] 164

Figure 47 Band diagram of silicon showing the defect states created in the forbidden region on addition of various impurities.[302, 303] 167

LIST OF TABLES

Page

Table 1 Crustal elemental abundances of elements used in state of the art thermoelectrics. Shaded in violet are the state of the art materials which are rare and toxic. Shaded in green are the materials used in this work and are non-toxic as well as earth abundant[94] 26

Table 2 A literature survey of thermoelectric figure of merit for various metal silicides[5, 67] 30

Table 3 Table showing the differences in lattice parameters among zinc phosphide, copper oxide and three different structures of boron nitride[290-294] 96

Table 4 Various scattering mechanisms and their corresponding scattering rate dependence on temperature and frequency[298] 163

Table 5 Physical and electronic properties of magnesium silicide.[97, 98, 297] 166

CHAPTER I

INTRODUCTION

The current annual rate of energy consumption by mankind is 13 terawatts and is expected to increase to 43 terawatts by the end of this century, as shown in Figure 1.[1] Such a tremendous increase in energy demand not only strains the available supply of fossil fuels, but also negatively impacts the environment. If, the contribution to energy demand from the conventional fossil fuels needs to be reduced (Figure 2**),** while sustaining the current standard of living, new and efficient methods for energy production must be explored.[1] This portfolio should include waste heat harvesting technologies, as a majority of energy generated is lost as waste heat. In United States, as shown in Figure 3, during 2013, 60% of the total energy (99 Quads) generated was lost as waste heat. To reiterate, the future portfolio of renewable energy necessary to counteract the ever increasing demand for energy should be composed of a multitude of technologies, such as wind, solar, geothermal, tidal, etc., which complement each other. Each of these technologies has its own set of advantages and drawbacks. In addition to exploring new energy generation technologies, the existing energy consuming/conversion processes and technologies (such as in automobiles, power plants, etc.), must be modified to be more energy efficient and cost effective so as to reduce the amount of lost heat.

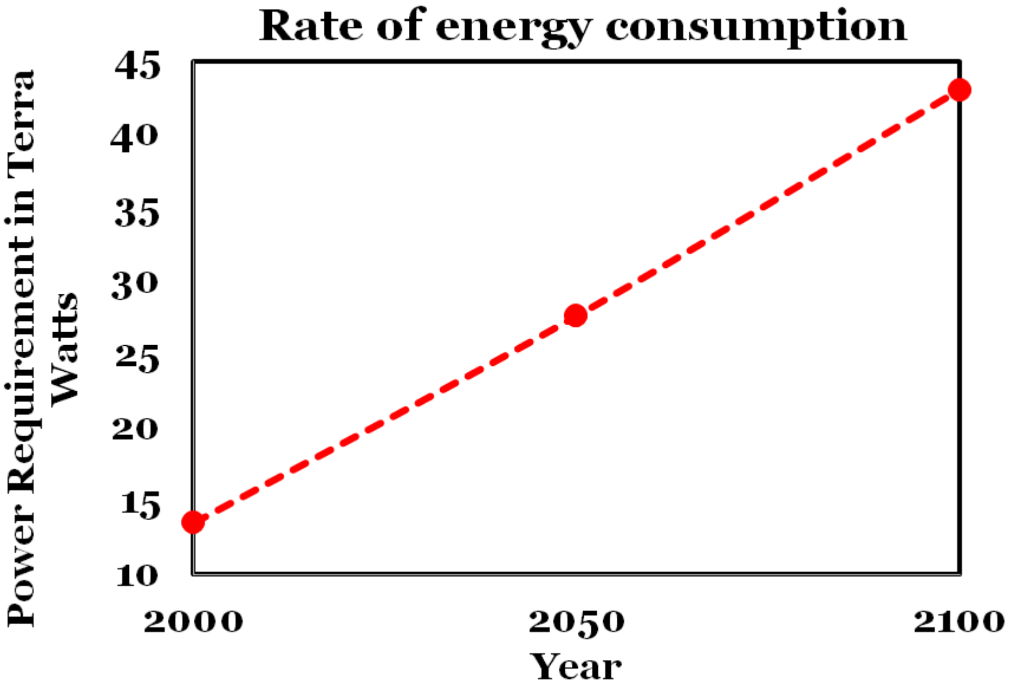

Figure 1 Increase in the rate of energy over the century as predicted by LLNL[1]

Over the last few decades, tremendous effort in photovoltaic research to produce electricity from sunlight more efficiently and cost effectively has been performed.[2] This led to a lowering in the cost of solar cells. However, the high installation costs, coupled with moderately lower efficiencies of solar cells, limit their widespread use. In addition, photovoltaics must be often water-cooled, must undergo daily maintenance and cannot be used in remote locations.[3] Solid-state thermoelectric devices useful for converting thermal energy into electricity circumvent some of these challenges.

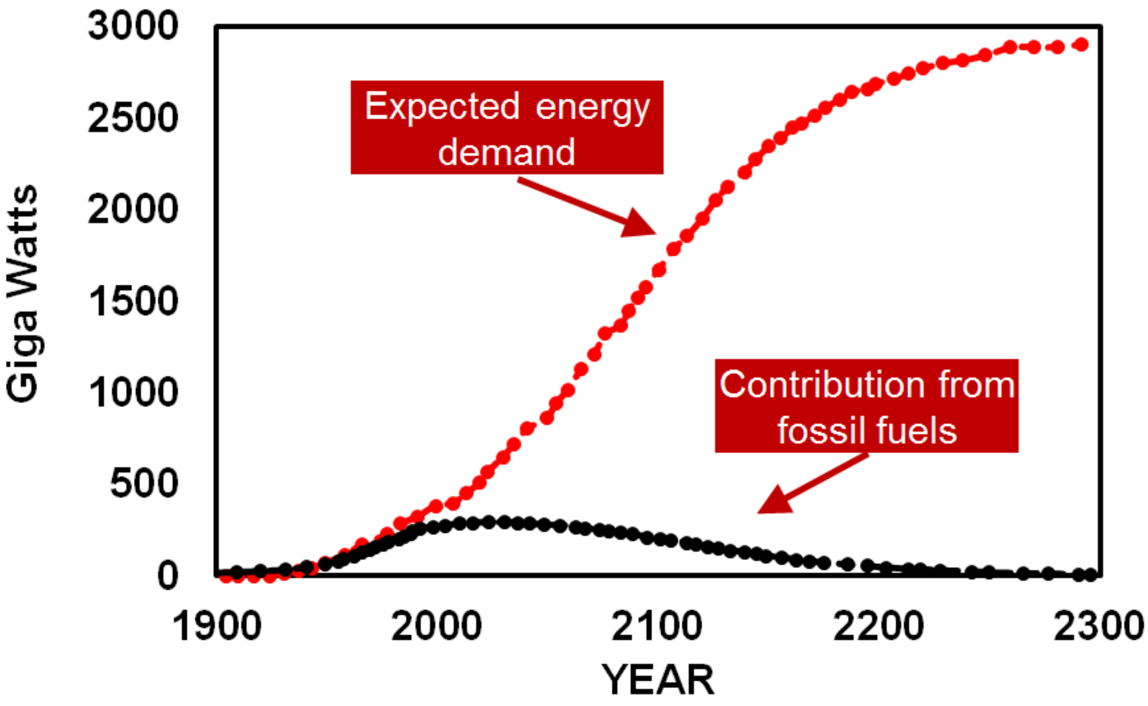

Figure 2 Expected energy demand in the future and the contribution of fossil fuels to the supply.[1]

Introduction to thermoelectrics

Thermoelectrics are solid-state energy conversion devices, which convert heat to electricity. Thermoelectric effect comprises of three different effects i.e., Seebeck effect, Peltier effect and Thomson effect. Seebeck effect was discovered by Thomas Johann Seebeck in 1823.[4] He observed that a magnetic needle was deflected due to the flow of electricity when the magnetic needle was placed in the vicinity of a closed loop formed by two dissimilar metals with one heated junction, as shown in Figure 4. Many materials were investigated for the Seebeck effect, including materials which are currently referred to as semiconductors. In fact, the very first application of semiconductors was not in electronics but thermoelectrics.[5] Seebeck coefficient is defined as the voltage generated per unit degree change in temperature. A few years later, in 1835, a complementary effect was reported, i.e. Peltier effect by Jean Charles Athanase Peltier. He observed that circulating electricity through a loop of dissimilar metals caused a temperature difference near the junctions. In 1851 Lord Kelvin established the relation between Seebeck and Peltier coefficients and introduced a third effect, the Thompson effect. A schematic of Seebeck effect and Peltier effect are shown in Figure 5. These effects are defined below.

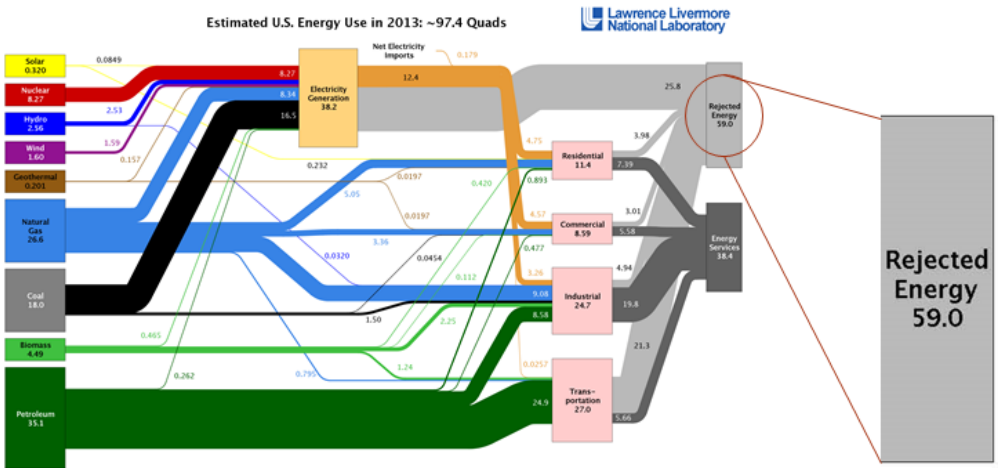

Figure 3 Spaghetti diagram showing the various sources of energy generation in United States in 2013. It is notable that from 97.4 quads of energy generated in the U.S. 59 Quads (about 60%) of energy is wasted as rejected heat energy.[1]

Peltier Effect: It is defined as "the relative change in heat content at an interface of dissimilar metals when a current flow is maintained across the interface".

Thomson Effect: It is the "reversible change of heat content within any single homogenous conductor in a temperature gradient when an electric current passes through it"

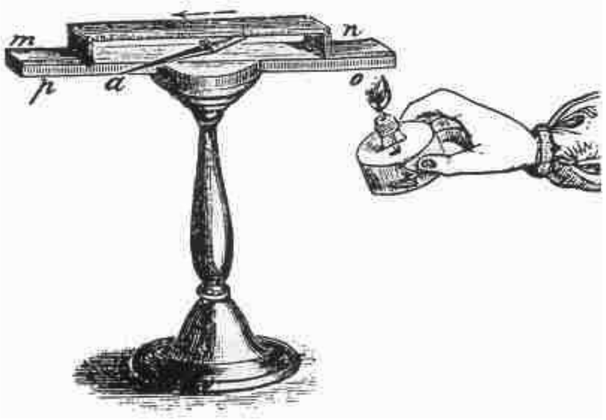

Figure 4 A schematic of the first experiments done by Seebeck to discover Seebeck effect[6]

The Seebeck coefficient (S) and Peltier coefficient (Π) are related as follows

Π = T*S, where T is the absolute temperature.

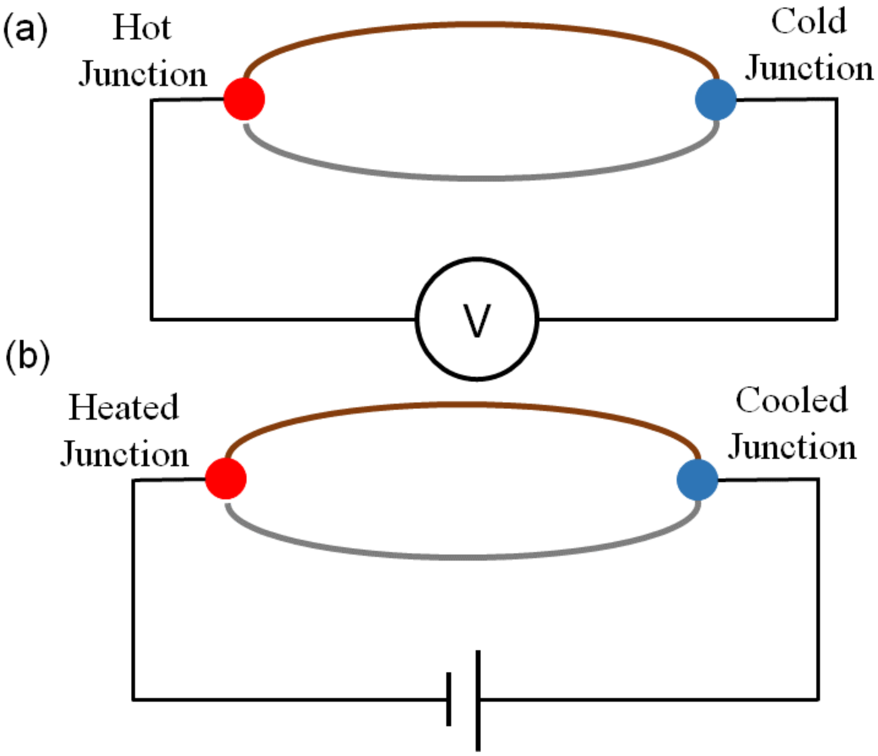

Figure 5 A schematic shown a) the Seebeck effect and b) the Peltier effect

Thermoelectrics for energy conversion

The absence of moving parts in a thermoelectric device allows for a compact design and silent operation. Among various energy conversion devices, thermoelectrics have the highest specific energy (energy generated/device weight) output, which makes them highly suitable for use in portable applications.[7-9] One of their most celebrated applications is in radioisotope-thermoelectric generators (RTG), used for powering deep space missions such as Voyager 1&2, Cassini, etc.[10] As the satellites move farther away from Mars, sunlight is not intense enough to power them, and therefore RTGs are the only viable option. Thermoelectric devices can be used for long time periods without any maintenance, and this allowed the RTGs to last for more than thirty years.[5] Currently, thermoelectrics are also making their way into compact mobile coolers and car seat heaters.[11, 12] In spite of all the mentioned advantages, their use is limited to niche applications. The large-scale deployment of these devices for terrestrial applications such as topping cycles,[13] small scale cogeneration,[14] automobile waste heat recovery,[15] etc. are still in the distant future. This is mainly due to the high costs and low efficiencies of thermoelectrics compared to other energy generation methods.

The current thermoelectric materials, which are not only prohibitively expensive but also are made from toxic elements, do not help in alleviating the main drawbacks namely, high costs and lower efficiencies. In addition to waste heat harvesting, thermoelectrics can also be used in renewable energy generation (solar thermoelectric generators useful for converting solar thermal energy into electricity); nonetheless, this application faces the same challenges presented before.[16, 17]

The efficiency of thermoelectric materials is represented by the dimensionless figure of merit, zT. It is evident from Equation 1 that the efficiency of the device is dependent on the zT of the material and the temperatures of operation, i.e. the hot and cold side temperatures. Higher zT values result in materials and devices, which can convert heat to electricity with higher efficiencies. The relation between zT of a material and heat-to-electricity efficiency for various hot side temperatures (with the cold side at room temperature, 300K) is shown in Figure 6.

$$\eta = \left(\frac{T_H - T_C}{T_H}\right)\left(\frac{\sqrt{1+zT}-1}{\sqrt{1+zT}+\frac{T_C}{T_H}}\right)$$

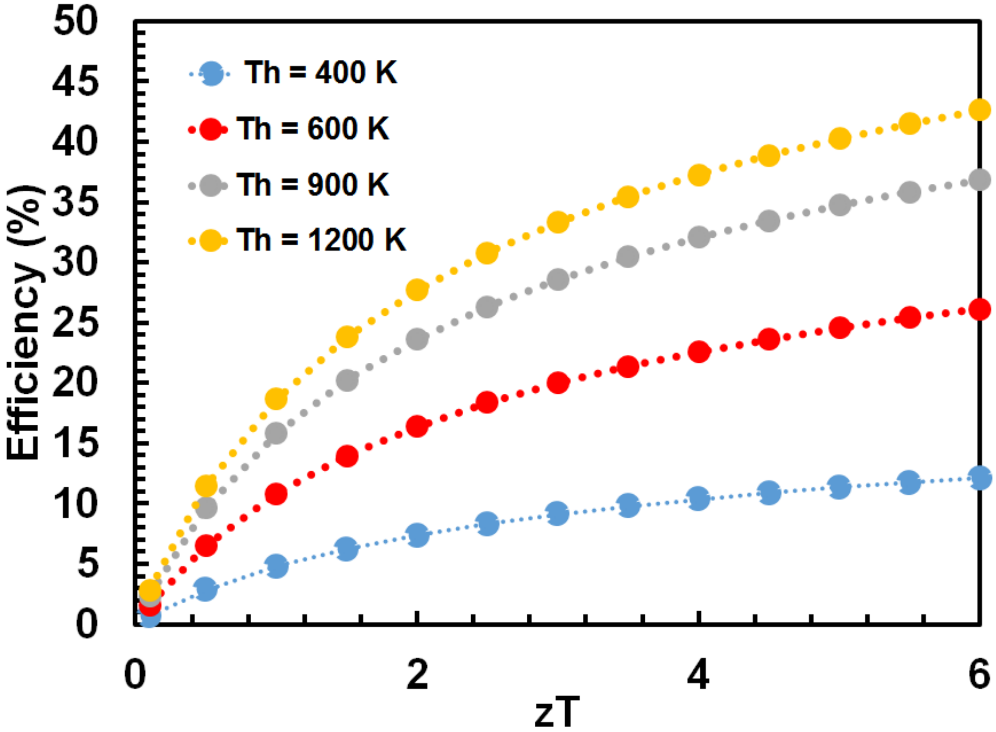

Figure 6 Calculated zT vs efficiency for various hot side temperature, the cold side temperature is 300K

A case for efficient and cost effective thermoelectric materials

A recent report published by the Department of Defense (DOD) has predicted that for any new energy generation technology to be commercially viable it has to produce one Watt of electrical power at a cost lower than 1 dollar.[18] Even at $zT = 1$, any thermoelectric material operating below 135 ^{o}C is not commercially viable. Only materials which operate at an average temperature above 275^{0}C with $zT > 1$ can achieve the \$1/W target.[19] For waste heat scavenging, the existing thermoelectric materials have lower conversion efficiencies compared to other alternative technologies such as organic Rankine cycles.[20] In addition to lower zT values, thermoelectric devices face additional challenges, such as oxidation and material degradation, electrical and thermal contact degradation owed to their thermal expansion mismatch.[21] In addition, most of the primary energy generation technologies cost less than \$3 per watt (natural gas < \$0.5/W, coal < \$1/W and nuclear < \$3/W). Currently only subsidized photovoltaics can generate electricity at a cost less than \$1 per watt.[22] Overall, achieving cost-effectiveness requires thermoelectrics, which a) operate at temperatures above 275 ^{o}C, b) have zT greater than 1 and c) are made of low-cost raw materials.[22] The prices of raw materials are usually subject to market fluctuations and are also affected by the purity requirements. Thermoelectric modules usually use materials with purity > 99.99% which adds uncertainty to their cost estimation.[19] In lieu of materials' costs, an alternate argument can be made in terms of their abundance with the assumption that widely available materials cost lower.[23] Therefore, for thermoelectrics to be commercially viable, they should be made from materials abundantly available in the earth's crust. In essence, the need of the hour is thermoelectric materials, which are highly efficient, chemically and thermally stable, and synthesized from earth abundant elements.

<u>Materials for thermoelectrics</u>

The state-of-the-art thermoelectric materials which exhibit high efficiencies (e.g., Bi_2Te_3, SiGe and PbTe) are made from rare-earth and toxic elements.[24] The thermoelectric figures of merit of these materials are represented in Figure 7. The elemental abundance of these materials is less than 100 ppm.[25] Tellurium and germanium are the two most widely used elements in thermoelectric materials, with crustal abundance of only 0.001ppm and 1 ppm, respectively.[26] This limits their use to niche applications, where the emphasis is only on power generation, but not on cost and toxicity. For a material to be cost effective in terrestrial thermoelectric applications, all of the elements in the compound (except the dopants, which by definition are used in small quantities) must have a crustal abundance of at least 30 ppm.[23]

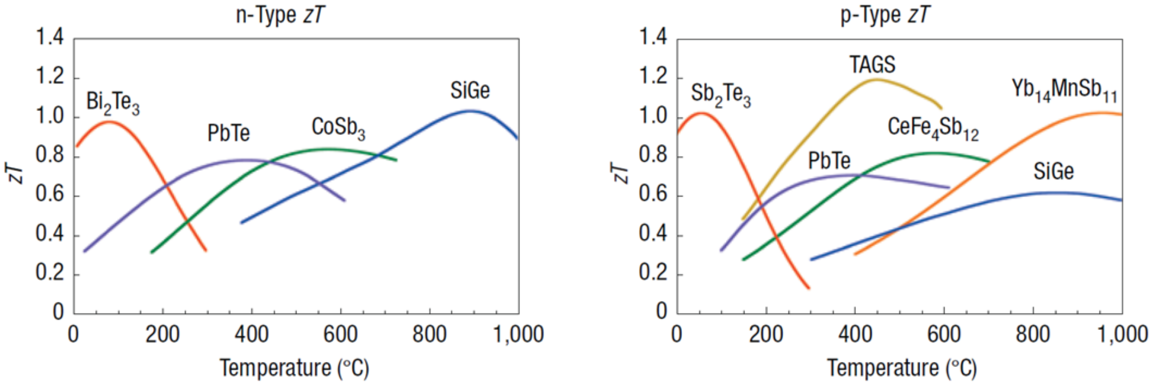

Figure 7 Thermoelectric figures of merit for (a) n-type and (b) p-type state of art materials.[7] Reprinted by permission from Macmillan Publishers Ltd: *Nat. Mater.* 2008, *7*, 105-114

History of thermoelectrics

The efficiencies of thermoelectric materials, including those composed of rare-earth elements, have not significantly improved over the past half century.[7, 27, 28] Only in the last decade, higher thermoelectric efficiencies were demonstrated. This is owed to the tremendous developments in nanotechnology, and the synthesis and characterization of nanomaterials.[29, 30] There were two key periods where thermoelectric efficiencies were demonstrably increased. Firstly, during the late 1950s when these devices were used for space exploration missions.[10] Secondly, when nanomaterials were predicted to be the future of the field to improve the thermoelectric efficiency in the 1990s. The latter occurred when in a series of papers, Hicks and Dresselhaus, reported that materials with nanomorphology have the properties necessary to both tune and enhance zT.[30, 31] Increased power factor owing to quantum confinement, decreased thermal conductivity owing to phonon confinement, and increased phonon scattering were key in achieving a higher zT.[30-32] Based on these predictions, thin films and nanowires were explored for thermoelectric applications and it was concluded that nanowires have an extra degree of freedom to influence and increase the thermoelectric figure of merit zT.[31] In fact, it was calculated that a zT of 14 was achievable if the bismuth nanowires were synthesized as thin as 5 angstroms.[30]

Following this, nanomaterials, i.e., nanoparticles, nanowires and thin films, have been explored for their use in thermoelectrics due to their large surface-to-volume ratio.[33] The crucial factor here is the large surface areas, which create more scattering centers for phonons, thereby decreasing the thermal conductivity. However, the zT of material depends on both the electrical and thermal conductivity; an increase in surface area decreases both the electrical and thermal conductivity. The key challenge for increased thermoelectric performance improvement is to reduce the thermal conductivity more than the electrical conductivity. In addition, quantum confinement in nanoparticles leads to an increased Seebeck coefficient; however, this is at the expense of decreased electrical conductivity. Nanoparticles decrease both electrical and thermal conductivities, and when the diameters of the nanoparticles are small enough to observe quantum confinement effects, they act as insulators.[34-37] Thin films, on the other hand, maintain high electrical conductivity but they do not suppress the thermal conductivity enough to achieve high zT values. An alternate form of materials, nanowires, provides a comfortable median of properties required for achieving high zT values in thermoelectric materials. Due to their anisotropic nature, nanowires possess high electrical conductivity in one direction and scatter the phonons in the other orthogonal directions, thereby reducing the overall thermal conductivity. Nanowire form of materials also allow for the easy determination of anisotropicity in the thermoelectric performances of materials.

Magnesium silicide for thermoelectrics

One of the materials that fits the criteria described above is Mg_2Si. It is expected to have high zT values due to its high Seebeck coefficient and high electrical conductivity, combined with its relatively low thermal conductivity.[38, 39] Furthermore, Mg_2Si is made from earth-abundant and non-toxic materials.[40] Mg and Si have an abundance of 29,000 and 270,000 ppm, respectively, which are very high compared to the well-known thermoelectric materials Bi (0.025 ppm), Te (0.001 ppm), Ge (1.4 ppm), and Pb (10 ppm).[23, 25, 39] Finally, both Mg and Si are non-toxic in nature.[41] The current widely accepted thermoelectric figure of merit of Mg_2Si is 0.8.[39, 42] Only one group of researchers reported a zT of 1.2 but this result has not been not independently verified.[43, 44] Satyala *et al*. predicted using theoretical calculations that a system of Mg_2Si and Mg_2Sn has a potential to achieve a zT of 3.[41] However, the current zT of these materials is less than one (approximately zT = 0.8), which leaves the scope for enhancing zT.

Achieving high zT in Mg_2Si system is hindered by the following problems: 1) the propensity for oxidation of Mg_2Si into MgO in the presence of both air and water, 2) its brittle nature, and 3) instability of Mg_2Si at higher temperatures and upon thermal cycling.[44-46] The propensity of Mg_2Si to oxidize at both ambient and elevated temperatures leads to the formation of oxide layer on top of the Mg_2Si which reduces the electron mobility and therefore thermoelectric performance.[47, 48] Its brittle nature makes fabrication of macroscale devices a problem.

Any attempt to commercialize thermoelectrics must not only concentrate on synthesizing mass quantities of nanomaterial (in this case nanowires) of Mg_2Si in a cost effective manner, but must also address the device fabrication and assembly challenges in order to solve the thermal and chemical stability problems discussed above.[46] In addition, ways of assembling nanowires into bulk anisotropic devices is necessary for ascertaining their thermoelectric performances in various crystallographic directions.

CHAPTER II

LITERATURE REVIEW

The performance of a thermoelectric material (i.e. material from which thermoelectric devices are fabricated) is given by figure of merit (zT), the dimensionless number $zT = \frac{S^2\sigma}{\kappa_e + \kappa_L}T$, where S is the Seebeck coefficient, σ is the electrical conductivity, T is the absolute temperature, and κ_e and κ_L are the electronic and lattice contributions to the thermal conductivity.[49, 50] The thermoelectric figure of merit depends on quantities which are interdependent on each other; Seebeck coefficient and electrical conductivity are inversely related i.e. an increase in the electrical conductivity leads to loss in Seebeck coefficient.[51, 52] The relation between these factors are shown in Figure 8. Additionally, electrical conductivity is directly proportional to electronic thermal conductivity (Widemann-Franz law).[7, 53]

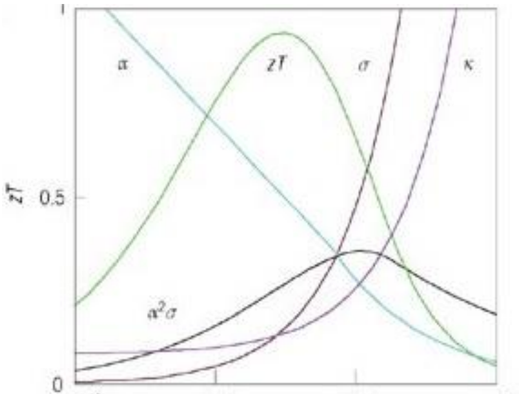

Figure 8 A schematic showing the relation between seebeck coefficient, electrical conductivity, thermal conductivity and zT with respect to the career concentration of a material[7] Reprinted by permission from Macmillan Publishers Ltd: *Nat. Mater.* 2008, *7*, 105-114

The current champion material, SnSe, is reported to have a zT of 2.6.[54] However, the current accepted and verified values of zT are near unity (i.e. zT = 1).[55] Higher zT's are required before these devices can enter the consumer market.[52] In addition the zT values of materials did not improve significantly for a long period of time i.e., from 1950 to early 2000. For five decades the zT values were below 1 as shown in Figure 9. Introduction of nanomaterials for thermoelectrics drove the rally for increase in zT, as shown in Figure 9. Although increase in zT was reported, many of these values are not verified and are viewed with skepticism.

Nanowires for thermoelectrics

A series of publications by Hicks and Dresselhaus on the enhanced thermoelectric performance via nanostructuring kicked off the race to increase the zT of thermoelectric materials via nanostructuring.[30-32] They predicted an increase in the thermoelectric performance would be due to increased power factor ($S^2\sigma$) via quantum confinement and decrease in thermal conductivity via increased phonon scattering events at the boundaries and interfaces of the nanomaterials. Nanowires were especially predicted to have better thermoelectric performance compared to thin films and nanoparticles as their geometry allows for phonon confinement in the two directions perpendicular to the axis while the axial direction acts as a high way for electrons. This allows for reduced thermal conductivity without loss of electrical conductivity.

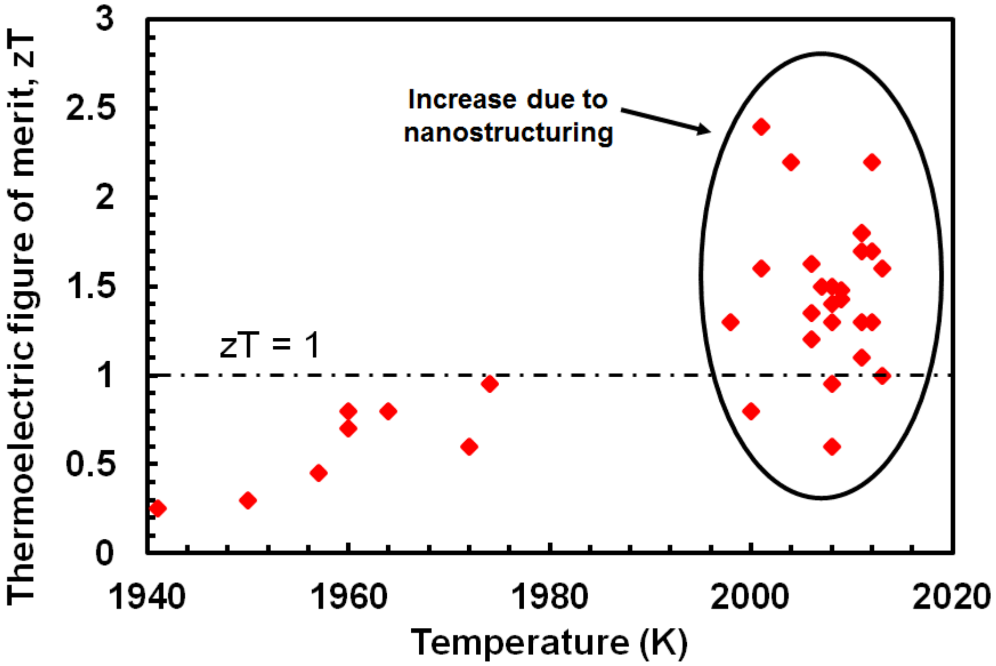

Figure 9 zT vs year, showing the slow increase in zT before 2000 and increase in zT due to nanostructuring[14, 27, 28, 51, 56-61]

zT enhancement due to quantum confinement

When the diameter of the nanowire is on the order of the electron wavelength, the electron is confined to the dimensions perpendicular to the axis. This leads to the discretization of the bands in the two directions, as shown in Figure 10**.** When the Fermi level is adjusted so as to be near the edge of the sub-bands as shown in the Seebeck coefficient is significantly boosted, which in turn increases the power factor as shown in Figure 11(a). However, these calculations by Hicks and Dresselhaus assumed only one sub-band in the nanowire. Theoretical predictions reported by Cornett and Rabin, considering multiple sub-bands, show that the power factor does not monotonically increase with decreasing diameter, but it decreases with decreases in diameter up to a certain radius, and then increases as the diameter of the nanowire decreases as shown in Figure 11(b).[62-64] In addition, some enhancements in power factors have been observed in nanowires but none of the investigations showed as significant improvements as predicted. From both the experimental and theoretical investigations it can be concluded that nanowires of ultra-low diameters (less than 5 A for Bismuth), which are practically not possible or at the very least cost prohibitive to manufacture, are required to realize a significant enhancement in zT via quantum confinement.

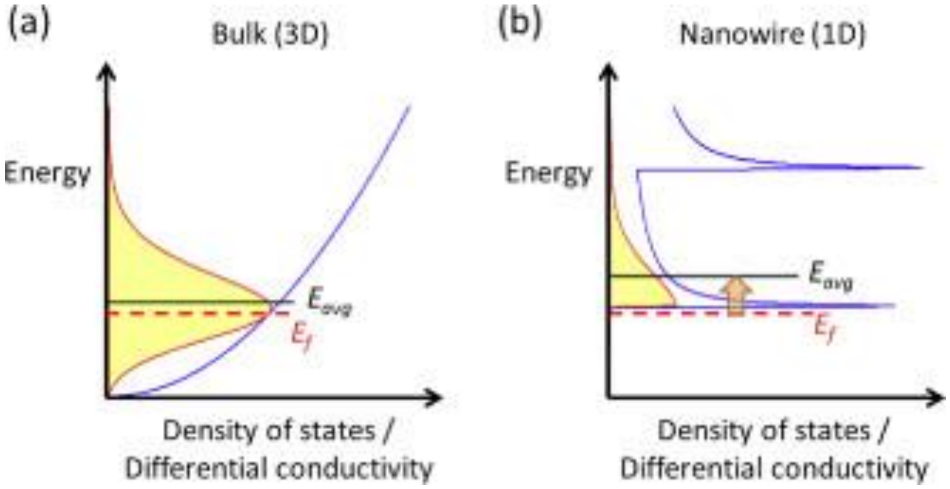

Figure 10 Density of states of (a) bulk material and (b) nanowires.[65] Reproduced with permission from WILEY-VCH Verlag GmbH & Co.

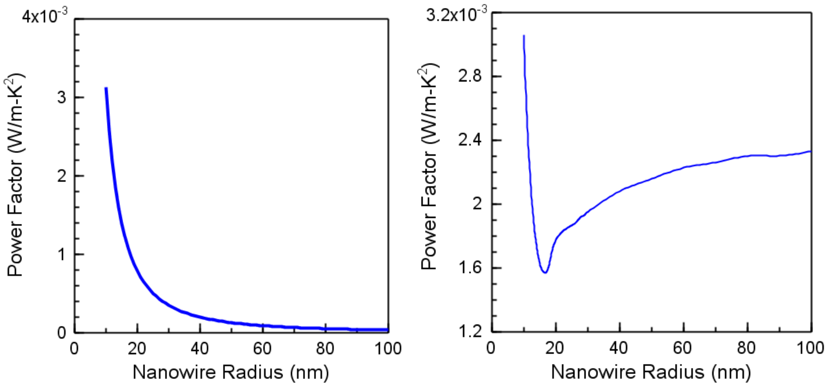

Figure 11 (a) The plot showing an increase in power factor as the diameter of the nanowire according to the Hicks – Dresselhaus in which only one sub-band is considered and (b) plot showing the change of power factor then an increase with decreasing nanowire diameter as per the calculations done by Rabin in which 300 sub-bands were considered.[63, 64]

Thermal engineering in nanowires for enhanced zT

Another venue for enhancing the zT of nanowires is via a decreasing the thermal conductivity without adversely affecting the electrical conductivity. The thermal conductivity of a material can be separated in two components, electron thermal conductivity (contribution to thermal energy transfer because of election/hole motion) and phonon thermal conductivity. The electronic component of the thermal conductivity is related to the electrical conductivity via the Wiedemann Fanz law as follows-

$\kappa_e = LT\sigma$, where L is the Lorenz number, T is the absolute temperature, and σ is the electrical conductivity. The Lorentz number is usually a constant and has a value of 2.44 x 10^{-8} WΩK^{-2}.[66] Therefore any attempts to reduce thermal conductivity have to be focused on reducing the lattice thermal conductivity as any changes in electronic part of thermal conductivity would invariably change the electrical conductivity. The lattice thermal conductivity of a material is given by

$$k_L = \frac{1}{3} C_v v l$$

Here Cv is the volumetric specific heat, υ is the phonon group velocity and l is the phonon mean free path. Most of the studies aimed at achieving higher conversion efficiencies (i.e. higher zT) are aimed at using the nanowire morphology to reduce lattice thermal conductivity. To achieve such a result, the diameter of the nanowires must be smaller than the phonon mean free path and larger than the electron mean free path. When the diameter of the nanowire is lower than the phonon mean free path, the boundaries between nanowires scatter the phonons, thereby reducing the lattice thermal conductivity.[67] Recent investigations using rough silicon nanowires have demonstrated a 100-fold decrease in thermal conductivity without a pronounced decrease in electrical conductivity. Further investigations into the effect of nanowire morphology on thermal conductivity have shown that the increase in roughness of the nanowires lead to an increased thermal resistance.[68] More information on this is included in appendix A.

Previous work on nanowires

Numerous experimental investigations have been reported thermoelectric characterization of single nanowire and nanowire array devices. Using nanowires for both the power factor enhancement and thermal conductivity reduction have been reported.

Power factor enhancement

Enhancement of zT in nanowires due to quantum confinement have not been clear and the power factor of the nanowires have been either less than or approximately equal to bulk values. The report published by Tian *et al.*, on InAs nanowires, in which the Fermi level was adjusted using the gate voltage, showed several peaks in the power factor[69].

These peaks were attributed to the Fermi level aligning with the sub-band edges (as explained in the above section). However these values are lower than that of the bulk InAs. Similarly the work done by Zuev *et al*. on Sb_2Te_3 nanowires (with diameters in range of 20 – 100 nm) have shown an increase in Seebeck coefficient (of about 30% compared to the bulk Sb_2Te_3) but lower power factor due to reduced electrical conductivity.[70] Analogously, no enhancements in power factor were observed in 11nm wide Ge-Si nanowires due to quantum confinement, this work was reported by Moon *et al.* [71] However, of the studies reporting on enhanced thermoelectric power factor, Wu *et al.* from Sweden observed enhanced power factors at 20K.[72]

Thermal investigations

Investigations on nanowires for reducing their thermal conductivity and thereby enhancing zT have had more success compared to the previous approach, which depends on power factor enhancement. Wingert *et al.* reported work involving the thermal conductivity measurements of Ge and Ge-Si core-shell nanowires with diameters less than 20 nm. Ultra-low thermal conductivity of 2 W/m-K have been shown compared to high values of thermal conductivity at RT for Ge i.e. 59 W/m-K.[73] The lowering of thermal conductivity is attributed to not only the interface effect of the core-shell structure but also to the phonon confinement, which is a result of the small nanowire diameters.

One of the most intriguing work in this area was done by Boukai *et al.*, in which 75 - 200 fold decrease in thermal conductivity in nanowire compared to bulk silicon was reported.[74] This translated to a zT of 1 at 200K for a single silicon nanowire and a zT of 0.4 at 300K. In the same way, work done by Hochbaum *et al.*, resulted in a 100 fold decrease in thermal conductivity of rough silicon nanowire compared to its bulk counterpart (149 W/m-K) with zT of 0.6 at room temperature.[68]

Eun Kyung Lee *et al.*, reported that a zT of 0.46 at 450K was realized in SiGe nanowire, with a thermal conductivity of 1.2 W/mK.[75] The same work predicted a zT of 2.2 at 800 K for the same SiGe nanowires. Liang *et al.* reported on power factor and thermal conductivity of single crystalline nanowires of PbSe. Their power factor and Fermi level controlled by applying a gate bias, however a low zT was reported.[76]The same group reported the thermoelectric characterization of degenerately doped PbSe nanowires made via solution phase technique. They reported a modest zT of only 0.12 at room temperature.[77] Lee *et al.*, reported on thermoelectric characterization of vapor grown single crystalline PbTe nanowires resulted in a zT of 0.0054 at room temperature compared to the zT of bulk PbTe (synthesized in their lab) 0.002 at room temperature.[78]

The above mentioned works and a few others on thermoelectric characterization of lead chalcogenides have shown lower zT values compared to their bulk counterparts. As these materials (i.e. IV-VI semiconductors) already possess lower thermal conductivities, the nanowire morphologies tend to have both low thermal and electrical conductivity. The loss in electrical conductivity is usually greater than loss in thermal conductivity, which leads to poor zT values. However, bulk nanostructuring along with doping of these materials (PbTe with Na_2Te) has lead to a zT of 1.7 and higher[79] (upto 2.2 when other techniques were used.[80])

Mavrorkefalos *et al.*, reported on electrodeposited Bi_2Te_3 nanowires of 52nm in diameter. They discovered electron mobility of the nanowires was about 19% higher than that of bulk. A zT of 0.1 has been achieved at 400K.[81] Similarly Zhang *et al.* reported on Bi_2Te_3 nanowires in which the Te nanowires were converted to Bi_2Te_3 by reacting them with Bi precursors, this resulted in a zT of 0.96 at 380K.[82] Work done on segmented nanowires of Bi_2Te_3-Sb and Bi_2Te_3-Te nanowires show a great promise with a seebeck increase and thermal conductivity decrease compared to the bulk.[83]

A theoretical investigation by Mingo shows that the thermal conductivity of CdTe nanowires can be reduced to 0.2 W/m-K for a 10nm wire which results in a zT greater than 1.[84] Other investigations on ZnO nanowires by Bui *et al.*[85] reported a dramatic decrease in the thermal conductivity of the nanowires. The thermal conductivity decreased from 100 W/m-K for the bulk to 5W/m-K for a 70nm nanowire at 300K. Zhou *et al.* has reported a very weak zT of 0.01 at 400K for InSb nanowire.[86] This low performance is attributed to the oxidation of InSb nanowires.

Theoretical investigations by Mingo have shown that for InSb nanowire with a diameter of 30 nm, a zT of 3 is achievable. However these high zT's in InSb nanowires have not yet been observed experimentally.[61]

Investigations on nanowire arrays

Although only two experimental investigations have shown enhanced thermoelectric figure of merit using single nanowire devices, interest in nanowire thermoelectrics has been extensive. This is in part because there is no fundamental principle limiting the zT value and since many theoretical investigations have concluded that nanowire, based thermoelectrics are the way to achieve high zT values.

However, it is obvious that single nanowire devices are not practical to be used in terrestrial applications. Therefore, scientists and engineers have focused their effort on using arrays of nanowires for achieving thermoelectric devices with an enhanced zT. One of the initial work was done by Abramson *et al.*, in which arrays of silicon nanowires grown by VLS method were used as the thermoelectric device.[87] The gaps between the nanowires were filled with parylene, a polymer with very poor thermal conductivity. This was done to provide structural stability and thermal isolation between the nanowires. Though thermoelectric characterization of the device did not yield any enhancement in the zT, this work paved a way for using nanowires for bulk applications. Similar works have been reported by various groups on the thermoelectric characterization of silicon nanowire arrays filled with a very low thermal conductor.[88-91] No significant enhancements of zT were reported. A schematic of such a device is shown in Figure 12.

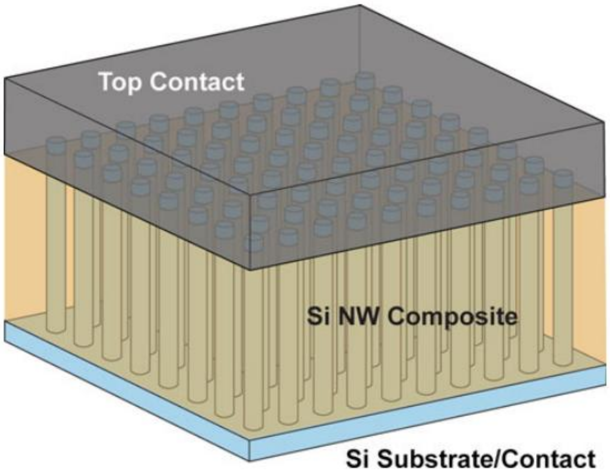

Figure 12 A schematic showing a nanowire array based thermoelectric device.[88] Reproduced with permission from TMS, 2012

Similar works on Bismuth and Bismuth telluride nanowire arrays were also performed.[92, 93] Though these devices reported a competitive performance, the performance gains were not even on the order of gains observed in individual nanowires. In addition, the number of steps required to fabricate such a device makes them cost prohibitive to be used in terrestrial applications where the devices must compete with more cost effective technologies such as solar cells.

Material selection criteria

The state-of-the-art thermoelectric materials which show high efficiency (such as Bi_2Te_3, SiGe, PbTe etc.) are made from rare-earth and toxic elements.[24] The elemental abundance of these materials are less than 30 ppm.[25] Tellurium and germanium, two most used elements in thermoelectrics, have a crustal abundance of 0.001ppm and 1ppm respectively.[26] In fact these materials cost orders of magnitude more than gold. This limits their use to niche applications where neither cost nor toxicity is a factor. For a material to be cost effective in terrestrial thermoelectric applications, all of the elements in the compound (except the dopants) must have a crustal abundance of at least 30ppm.[23] The cost and crustal abundance of various materials used for thermoelectric application are shown in Table 1**.** A simple analysis comparing zT vs the cost of the material (excluding the cost of production and packaging) shows that state of the art materials cannot compete against the low efficient materials as shown in Figure 13. It shows that the current champion material SnSe which has been claimed to have a zT of 2.6 has a zT/cost value lower than Zn_3P_2 manufactured in our lab, which as a zT of only 0.23.

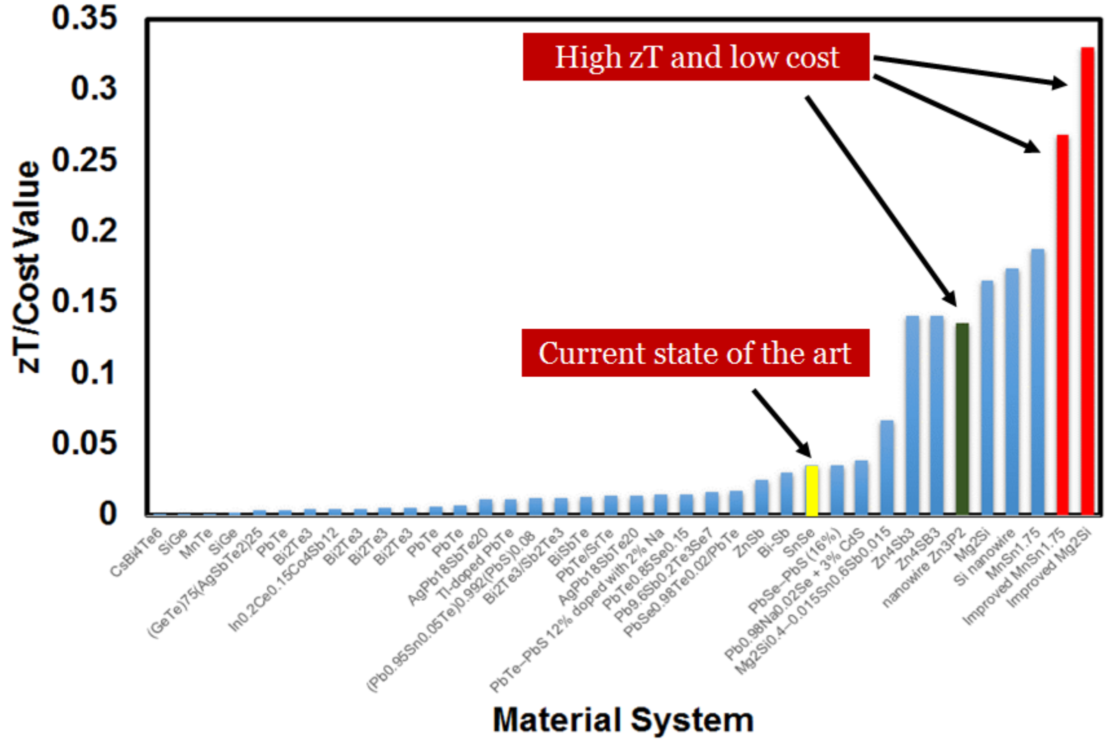

Figure 13 zT per dollar value for prominent thermoelectric materials. The yellow bar shows the zT/cost value of the current state of the material. The green bar and the red bars shows the achieved and expected zT/cost value of thermoelectric materials composed of earth abundant. The cost of the compounds were calculated from elemental costs provided in USGS 2013 survey.[29, 33, 54, 80, 94]

Zinc phosphide

Zinc Phosphide is a p-type, metal deficient semiconductor with a bandgap of 1.5eV.[95] It is a well known solar cell material, with reported efficiencies of about 6% via a magnesium-Zn_3P_2 Schottky diode solar cell.[96] Its constituent elements have a high crustal abundance (Zinc is 79 ppm and Phosphors is 1000ppm[94]) and is costs approximately $3/kg. Zn_3P_2 has a FCC tetragonal crystal structure, P42/nmc, with lattice parameters a = b = 8.0785 Å, c = 11.3966 Å as shown in Figure 14. It has unfilled lattice sites, which when filled could lead to reduction in thermal conductivity and increased thermoelectric efficiencies. However, this material has the following drawbacks - lack of good electrical conductivity and relatively low stability in oxidizing environments (i.e. in presence of oxygen, moisture or any acidic medium). The typical reaction of Zn_3P_2 with water and moisture are given below.

$$Zn_3P_2 + 6H_2O \rightarrow 3Zn(OH)_2 + 2PH_3$$

$$Zn_3P_2 + 4\ O_2 \rightarrow Zn_3(PO_4)_2$$

Zinc phosphide reacts with water to form zinc phosphide and phosphene, and with oxygen to form zinc phosphate.

Table 1 Crustal elemental abundances of elements used in state of the art thermoelectrics. Shaded in violet are the state of the art materials which are rare and toxic. Shaded in green are the materials used in this work and are non-toxic as well as earth abundant[94]

Metal	$/kg	Abundance PPM
Antimony	14.3	0.2
Bismuth	25.234	0.025
Cadmium	2.79	0.15
Germanium	1185	1.4
Lead	2.6	10
Selenium	145.97	0.05
Tellurium	349.35	0.001
Magnesium	5.17	29000
Manganese	3.982	1100
Zinc	2.189	79
Silicon	3.454	270000
Phosphorus	0.144	1000

Manganese and magnesium silicides

The other class of material studied in this thesis are silicides. This class of materials are highly investigated for their application in thermoelectrics, partly because silicon is the second most abundant element in the earth’s crust. Metal silicides are potential materials for thermoelectric applications due to their excellent mechanical and chemical properties. Except for alkali and alkaline silicides only higher silicides i.e. silicides with higher silicon in the stoichiometric ratio, show semiconducting properties. Higher silicides, i.e. silicon rich silicides of transition metals (Ru, Mn, Fe, Ru and Cr) have higher seebeck coefficients due to the d- orbital hybridization. The thermoelectric characteristics of these materials are presented in Table 2. Among them Mg_2Si is notable for its thermoelectric properties. Magnesium silicide has a band gap of 0.78eV with high electron mobility and low thermal conductivity.[97] It has an antifluorite crystal structure magnesium at the tetrahedral sites and silicon at the face centered position with lattice parameter ($a = b = c = 0.6351$nm). The phonon mean free path is upto 10nm and the electron mean free path is 2 nm.[97, 98]

Nicolau *et al.* predicted a zT of 3 is possible for certain solid solutions of silicide. Magnesium silicide is a mid to high range thermoelectric material.[99] A zt of 1.1 is reported for Mg_2Si - 0.4Sn - 0.6 solid solution by Fedorov.[44]

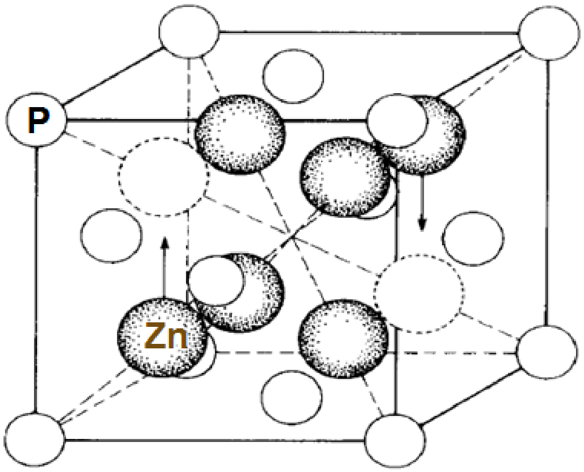

Figure 14 The tetragonal crystal structure of zinc phosphide.[100] Reprinted from, Elrod et al., Journal of Crystal Growth 1984, 67, 195-201., with permission from Elsevier

However, the current zT of these materials is less than one (approx. zT = 0.8), which necessitates enhancing zT. In Figure 13, the zT/cost of the prominent thermoelectric materials are plotted. Mg_2Si even at the current zT of 0.8 has the highest zT per cost efficiency. If the zT of this material is improved to 1.5 it is possible to use this material for commercial application.[23]

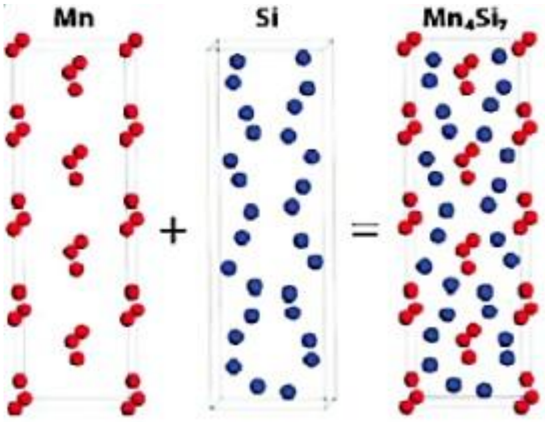

Figure 15 Nowotny chimney-ladder structure of higher manganese silicide.[101] Reprinted by permission from Macmillan Publishers Ltd: *Nature Communications* 2015, *6*, 6723.

Higher manganese silicide (HMS) has a Novtny-chimney ladder structure as shown in Figure 15. The composition of HMS ranges from $MnSi_{1.71}$ to $MnSi_{1.77}$. The other compositions of Mn and Si (which are not silicon rich) are more metallic in nature, which are not useful for thermoelectric performance. It has a band gap of 0.67eV and is a self-doped p-type material, with a relatively high carrier concentration and low carrier mobility. It is also considered to have high anisotropy in its kinetic and thermoelectric properties. Due to its strong anisotropy of charge and thermal properties combined with its complex crystal structure, it is expected to be a good thermoelectric material. Undoped HMS samples have relatively low zT due to the high carrier concentration. Its unusually low vapor pressure at 1000K and high stability, in addition to its relatively cheap and abundant elemental materials, make this material a noteworthy thermoelectric. Introduction of neutral dopants such as Ge makes this material a better thermoelectric due to the increased complexity in crystal structure.

Table 2 A literature survey of thermoelectric figure of merit for various metal silicides[5, 67]

Material	Band Gap	Type	Effective mass ratio	zT
$Mg_2(SiSn)$	0.7	N	1	0.8
$Mg_2(SiGe)$	0.74	N	1.2	1.07
$CrSi_2$	0.35/0.35	p/n	5/20.2	
$MnSi_{1.75}$	0.67	P	1	0.7
$ReSi_2$	0.12	P	1	
Ru_2Si_3	1.08	n/p	2.9/2.9	
$FeSi_2$	0.9	n/p	¼	0.2/0.4

CHAPTER III

PROBLEM STATEMENT AND HYPOTHESIS

Experimental studies performed over the last decade have explored the efficiency of single nanowire thermoelectric devices. In the case of silicon, a 100 time enhancement in the zT values was reported in nanowires, relative to those observed in bulk counterparts, i.e. an increase in zT from 0.006 to 0.6, has been reported.[102, 103] Other works exploring the efficiency of single nanowire devices have shown a moderate to significant boost in thermoelectric performances of up to 30 %.[104, 105] However, two decades after the aforementioned work by Hicks & Dresselhaus,[30-32] despite all the positive and exciting work published in the interim, reports on performance of thermoelectric devices based on bulk nanowire devices are scarce. As a result, no thermoelectric devices based on nanowires are commercially available. The only reports currently available are based on silicon nanowire arrays and polymer-nanowire composites.[88, 89, 106] The dearth of work on macrodevices based on nanowires is due to following reasons, among many, and are addressed in this thesis.

- Lack of methods for producing pure and uncontaminated nanowires on gram and kilogram scale in a reproducible manner
- Lack of methods to assemble these nanowires in a manner that offers precise control over electrical and thermal transport of the interfaces between nanowires in the assemblies and necessary to optimize the thermoelectric performance. The assembly strategies should preferably assemble nanowires in either randomly-oriented or aligned fashion on demand.

- Lack of methods to chemically and thermally stabilize the nanomaterials without loss of their novel and excellent electric and electronic properties. These issues are represented in Figure 16.

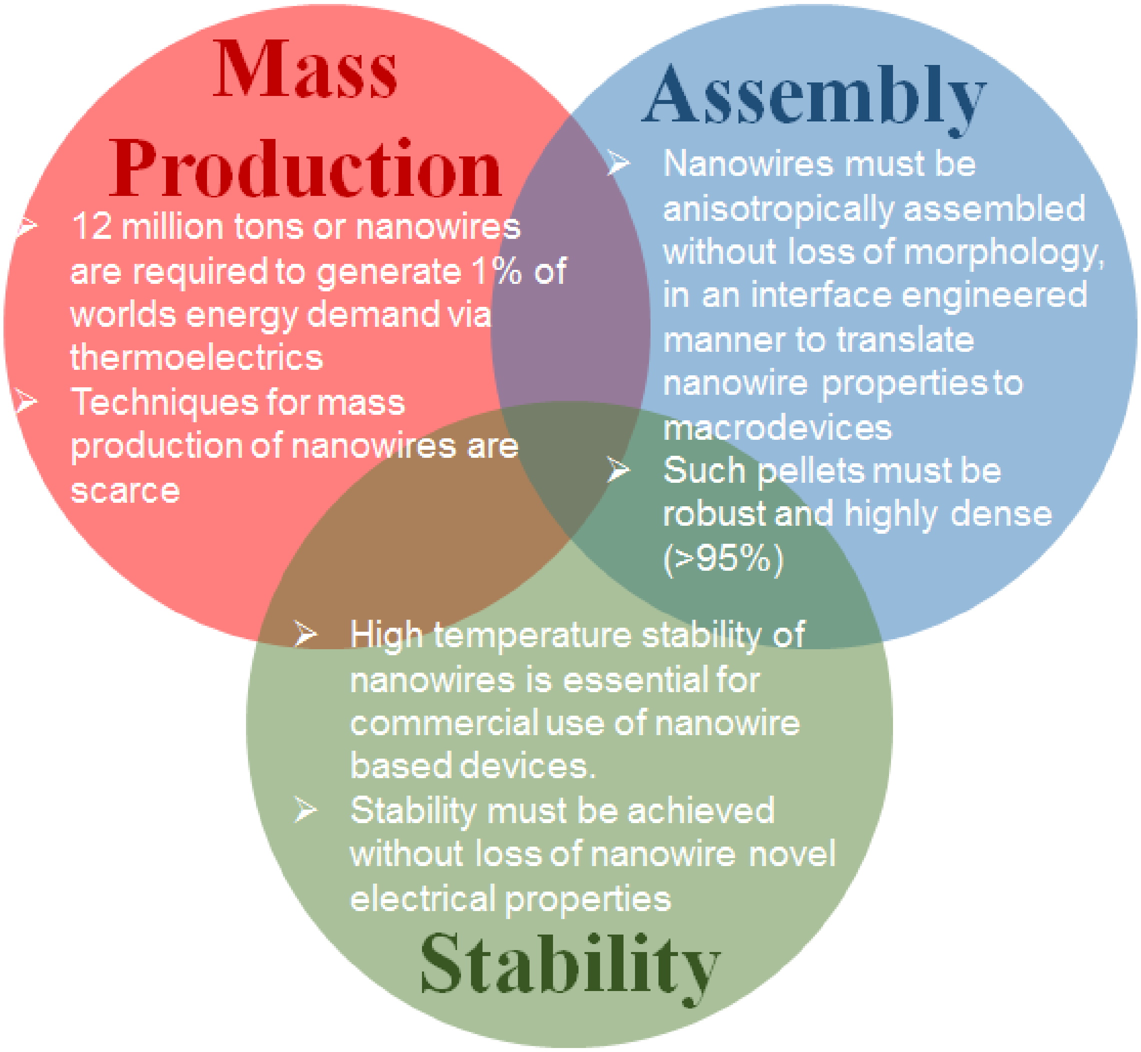

- 12 million tons or nanowires are required to generate 1% of worlds energy demand via thermoelectrics
- Techniques for mass production of nanowires are scarce

- Nanowires must be anisotropically assembled without loss of morphology, in an interface engineered manner to translate nanowire properties to macrodevices
- Such pellets must be robust and highly dense (>95%)

- High temperature stability of nanowires is essential for commercial use of nanowire based devices.
- Stability must be achieved without loss of nanowire novel electrical properties

Figure 16 Schematic showing the fields in which advances are needed to achieve materials with commercialization of thermoelectrics for domestic applications

The following sections outline the hypothesis behind the work in this dissertation, along with the goals.

Hypothesis

The following are the hypothesis of the work presented in this dissertation:

1. Although organic molecule decoration of nanowires offers it stability against air- and moisture-assisted degradation, it may not offer high temperature stability. Therefore, it is entirely possible that decorating nanowires with high-temperature-stable ceramic molecules (e.g., BN) may make render them stable at high temperatures. This work hypothesizes that that complete and conformal coating of the nanowires will make the nanowires stable, however such a coating will render the nanowire-nanowire interfaces electrically insulating, making it unusable in thermoelectric devices. To overcome this problem, this work hypothesizes that non-conformal decoration of the nanowires with BN makes them both stable and usable in thermoelectric devices. Here, the hydrophobic nature of BN ensure that the nanowires are non-wettable to aqueous media and hence resist degradation in their presence. In addition to increasing the stability of the nanowires, the non-confomal BN coating is also expected to improve the thermoelectric properties of the nanowires. The BN molecules are expected to scatter phonons, thereby reducing the thermal conductivity of the nanowires, without adversely affecting electrical transport.
2. Another hypothesis of this work is that a strategy for aligned assembly of nanowires into anisotropic bulk devices is necessary to test whether enhanced

thermoelectric performances in individual nanowires are translatable to bulk devices, and to document the anisotropicity in the thermoelectric performances of bulk nanowires devices. The latter is highly important because a strategy for measuring thermoelectric performance of individual nanowires in a direction perpendicular to their lengths is not currently possible. Suspended nanowire devices only measure thermoelectric performance of individual nanowires along their lengths.[74] In the literature, techniques for assembling nanowires in an aligned fashion into bulk devices do not exist. Literature review of nanowire assembly techniques demonstrates that monolayers of nanowires are obtained in an aligned fashion using shear forces.[107, 108] In this work Equal Channel Angular Extrusion (ECAE)[109, 110], a severe plastic deformation technique, is hypothesized to provide the shear forces for alignment and also for the consolidation of the nanowires. This coupled with the nanowire welded strategy demonstrated by our group previously[46] is expected to lead to anisotropic bulk thermoelectric devices based on nanowires.

3. Finally, it is the hypothesis of this work that it is possible to enhance the thermoelectric figure of merit of macro devices based on nanowires, composed of earth abundant elements, using the above mentioned techniques and the work performed previously in our lab i.e., welding the nanowires (via solid state diffusion for phase transformation).[46] The premise is that it is possible to enhance the thermoelectric figure of merit (zT) of Mg_2Si nanowire assemblies to about 1.5 – 2 from the current state of the art zT, which is approximately around 1. Literature

review of thermoelectric data on Mg_2Si shows a maximum achievable seebeck coefficient is 180-270 µV/K and maximum available electrical conductivity is 20,000-75,000 S/m, and minimum thermal conductivity of 2W/mK respectively.[39, 42, 44, 45, 111-124] These values were individually achieved, however if these values if obtained in the same device would dramatically improve the thermoelectric performance of Mg_2Si nanowire based devices to zT values of 1.5 or higher.

Goals

The objective of this work is to design various strategies that aid in fabricating efficient and stable nanowire-based thermoelectric devices. Contextually, each chapter in this dissertation described individual aspects of stabilizing/assembling nanowires. The description below is a previews individual goals and accomplishments (of each chapter) of this work.

1. Chapter IV: In this chapter the synthesis of pure and uncontaminated Zn_3P_2, Silicon and Mg_2Si nanowires is revisited.
2. Chapter V: In this chapter the consolidation of rigid silicon nanowires into aligned pellets is achieved using ECAE and described. Accomplishing the aim of achieving high density consolidation of mechanically rigid nanowires into aligned nanowire pellets (and thermoelectric devices) is described in detail in this chapter.
3. Chapter VI: This chapter describes a novel nanowires stabilization strategy involving their non-conformally decoration with BN. The increased stabilization of nanowires achieved as a result of this strategy is described in detail.

4. Chapter VII: In this chapter, the effect of BN addition to nanowire surfaces on their thermal transport properties is explored in detail.
5. Chapter VIII: In this chapter the thermoelectric properties of BN decorated $MnSi_{1.75}$ micron powders and welded Mg_2Si nanowires are explored.

CHAPTER IV

MASS PRODUCTION OF ZINC PHOSPHIDE SILICON AND MAGNESIUM SILICIDE NANOWIRES

Considering the recent thermoelectric efficiencies of reported on single nanowire devices, 12 million tons of nanowires are required to produce even 1 % of worlds energy demand. The enormity of this requirement is understood when compared to the production of iron in US is 20 million tons per year. To achieve such a high production of nanowires, methods to produce pure nanowires at a lower cost must be explored. In this section the production of Zn_3P_2 nanowires is explored via chemical vapor deposition of elemental components and production of magnesium silicide nanowires is achieved via phase transformation of silicon nanowires.[125]

Mass production of Zn_3P_2 and ZnO nanowires

The large-scale synthesis of Zn_3P_2 and ZnO nanowire was reported in earlier publications. The nanowires were fabricated by using direct reaction scheme by reacting red phosphorus/oxygen with Zinc foils in in a hot walled CVD chamber as shown schematically in Figure 17. The zinc foil rolled so as to fit into the reactor acts as both the substrate and the source of zinc foil. For fabricating Zn_3P_2 nanowires, the zinc foil was heated to 400C and the phosphorus to 485 C at pressure of 100 milli torr with a 5 sccm flow of hydrogen. The nanowires thus formed on the zinc foil are brushed off. For synthesizing the ZnO nanowires were fabricated by heating the zinc foil to 500 C in the flow of oxygen under atmospheric pressure.[126] Gram quantities of nanowires per day were produced using this technique. The zinc phosphide nanowires synthesized were characterized using XRD, SEM and TEM. The scanning electron and transmission electron images are shown in Figure 18. The nanowires were grown in [101] direction. The nanowires were characterized to have a diameter of 20 – 70 nm and with lengths between 5 – 40 μm.

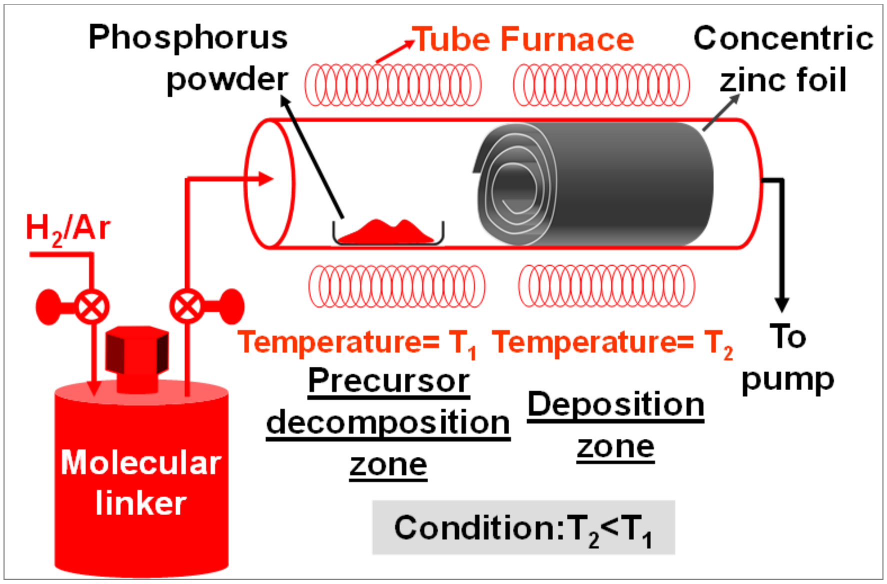

Figure 17 Schematic of 3 zone furnace for chemical vapor deposition chamber of elemental phosphorous onto rolled zinc foil for production of Zn_3P_2 nanowires

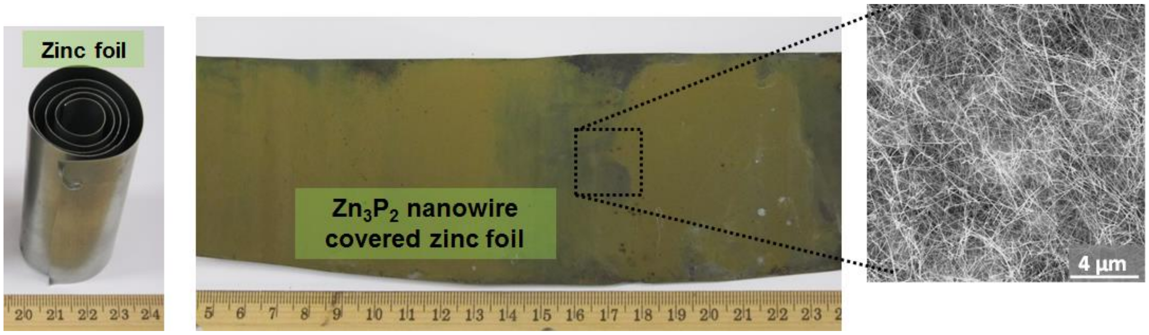

Figure 18 The scanning electron micrograph of the zinc phosphide nanowires synthesized by reacting the (a) zinc foil with elemental red phosphorous to result in (b) a completely converted foil with (c) nanowires of 20 – 50 nm in diameter.[127] Reproduced from Physical Chemistry Chemical Physics 2013, 15, 6260-6267 with permission of The Royal Society of Chemistry.

Owing to the difficulties in fabricating Mg_2Si nanowires in conventional fashion a novel phase transformation method was invented. Arrays of silicon nanowires fabricated by electroless etching were placed on Mg foil. Diffusion of Mg into the silicon nanowires resulted in the formation of Mg_2Si nanowires.[125, 128] The silicon nanowires required for the fabrication of Mg_2Si nanowires were fabricated by anisotropically etching silicon wafers. These wafers are first cleaned in piranha solution and acetone to get rid of any organic contaminants. This is followed by cleaning these wafers in HF solution to get rid of the SiO_2 passivation layer present on the wafers. Then the wafers are etched in a solution of 5M HF and 5M $AgNO_3$ solution. This step lasts for an hour and wafer are cleaned in acid to get rid of the silver so that pristine and un-contaminated silicon nanowires are obtained.

The mechanism of the nanowire production is as follows. The silver ions from silver nitrate are reduced to form silver nanoparticles on top of the silicon wafer as follow.

$$Ag^{+}+e^{-}\rightarrow Ag_{(s)}$$

These silver nanoparticles catalyze the reaction in which the silicon atom under the silver nanoparticles oxidize on reaction with water to form silicon-di-oxide as shown below.

$$Si_{(solid)} + 2H_2O - 4e^- \rightarrow SiO_{2(solid)} + 4H^+$$

The silicon-di-oxide thus formed is etched away by hydrofluoric acid leaving behind a pit in which the silver nanoparticle fall into.[129, 130] This mechanism is schematically represented in Figure 19.

$$SiO_{2(solid)} + 6HF \rightarrow H_2SiF_6Si + H_2O$$

Continuous selective etching of silicon leads to the formation of [100] and [110] silicon nanowires as shown in Figure 20. P-type silicon nanowires were synthesized by electroless etching of both p-type (boron doped) wafers. .

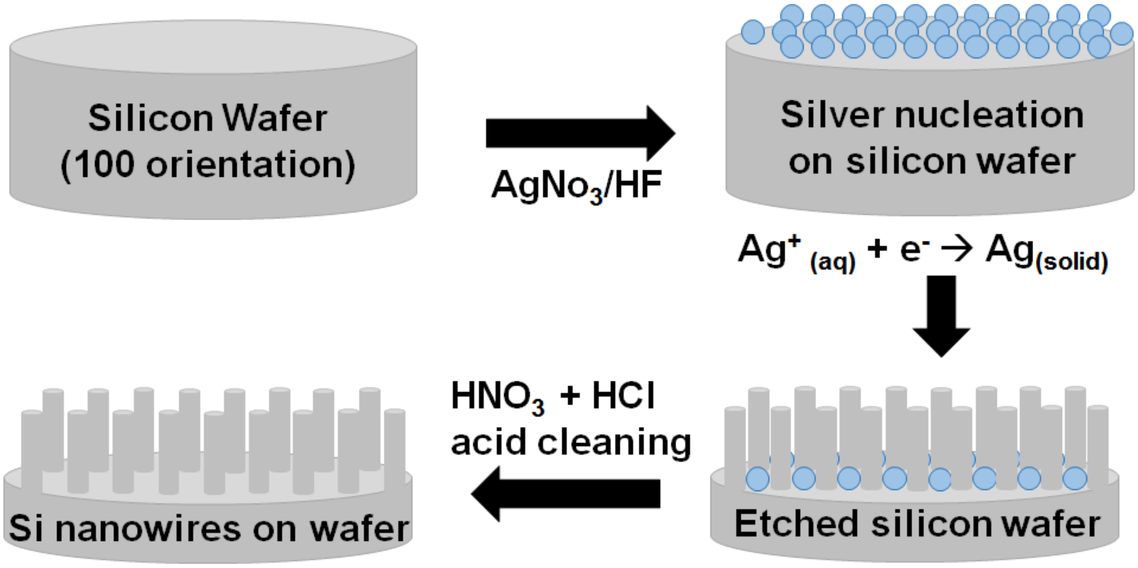

Figure 19 Schematic of silicon nanowire synthesis from a single crystalline (100) silicon wafer by etching in a solution of hydrofluoric acid and silver nitrate

Mass production of contaminant free silicon nanowires

Electroless etching of single crystalline silicon wafers resulted in the fabrication of arrays of silicon nanowires. Gram quantities of these nanowires were produced, Figure 21 . Electronic characterization of silicon nanowires shows that the nanowires had a diameter between 20 – 100 nm with a length range of 10 – 15µm as shown in Figure 20 (a & b). Transmission electron microscopy of the nanowires show their growth direction to be either [100] or [110], Figure 20 (c & d).

Silver removal from nanowire surfaces

The nanowires obtained from electroless etching of silicon wafers, using hydrofluoric acid and silver nitrate, are not expected to be contaminated by silver as the whole procedure takes place at a moderate temperature of 50C. No work reporting such contamination is published to date. However, we discovered that silver is embedded in the nanowire surface in trace quantities, undetectable by the EDAX detector of a TEM. This silver contamination is revealed only after the nanowires are exposed to shear forces. While undergoing ECAE the nanowires are exposed to shear forces and rub against each other. This exposes the silver in the nanowires as shown in Figure 28. Removal of this silver is an important step so as not to alter the electronic properties of silicon nanowires and thereby of Mg_2Si nanowires. This also leads to the recovery of silver, which makes the whole process more cost effective.

The phase transformation of silicon nanowires is achieved by diffusing magnesium through silicon nanowires. This method was demonstrated in a previous publication where silicon nanowires made via electroless etching are phase transformed in Mg_2Si

nanowires.[125] However, the silicon nanowires produced were contaminated with silver an essential process of electroless etching (see procedures section).

The use of silver in this procedure gives rise to two issues 1) contamination of silicon nanowires which ultimately leads to contamination and property poisoning of Mg_2Si nanowire, 2) silver is a precious metal costing more than $1000/Kg and the use of new silver for every etching increases the cost of reaction. Therefore a method for removal of silver in a fashion such that the silver is recoverable leads to cost effective procedure and uncontaminated silicon nanowires. More on this is included in goals and procedures section.

Fabrication of devices based on nanowires requires mass production of nanowires. The first step requires the production of impurity free silicon nanowires in a cost effective nanowire. Silicon nanowires will be synthesized using electrochemical etching of single-crystalline silicon wafers.[125, 128] The etching process uses hydrofluoric acid and silver nitrate solution. In the conventional synthesis, the silver used is usually removed by reacting the silver with a mixture of hydrochloric and sulfuric acid. This procedure has two drawbacks 1) the use of expensive precious metal i.e. silver which makes the whole procedure expensive and cost prohibitive, and 2) the contamination of silicon nanowires with silver. Contamination of the nanowires detrimentally influences the electrical and electronic properties of the silicon and Mg_2Si nanowires synthesized from them (more information provided in appendix B). Due to the trace amounts of silver in the silicon nanowires cannot typically detected using even a TEM. The evidence of silver presence can be seen when the nanowires are sheared using ECAE.

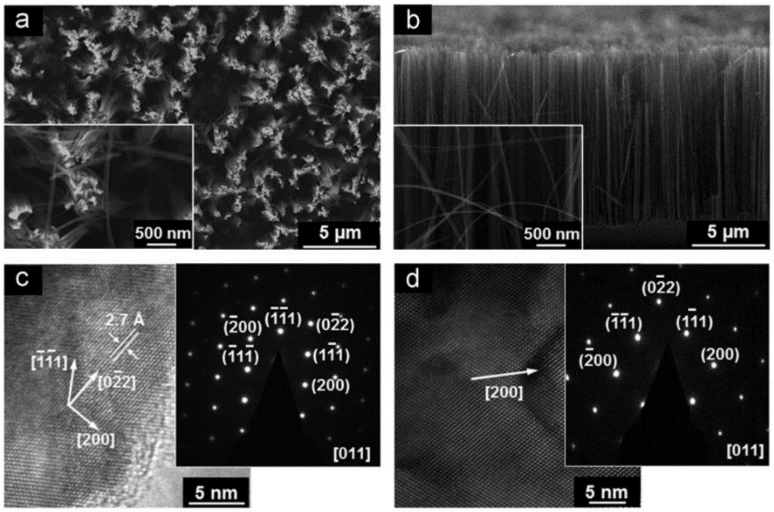

Figure 20 Scanning electron micrograph showing the a) top view and b) crossectional view of silicon nanowires fibricated via electroless etching. High resolution TEM images showing single crystalline nanowires with c) [110] and d) [100] growth directions.[125] **Reprinted from Materials Letters 2013, 100, 106-110., with permission from Elsevier**

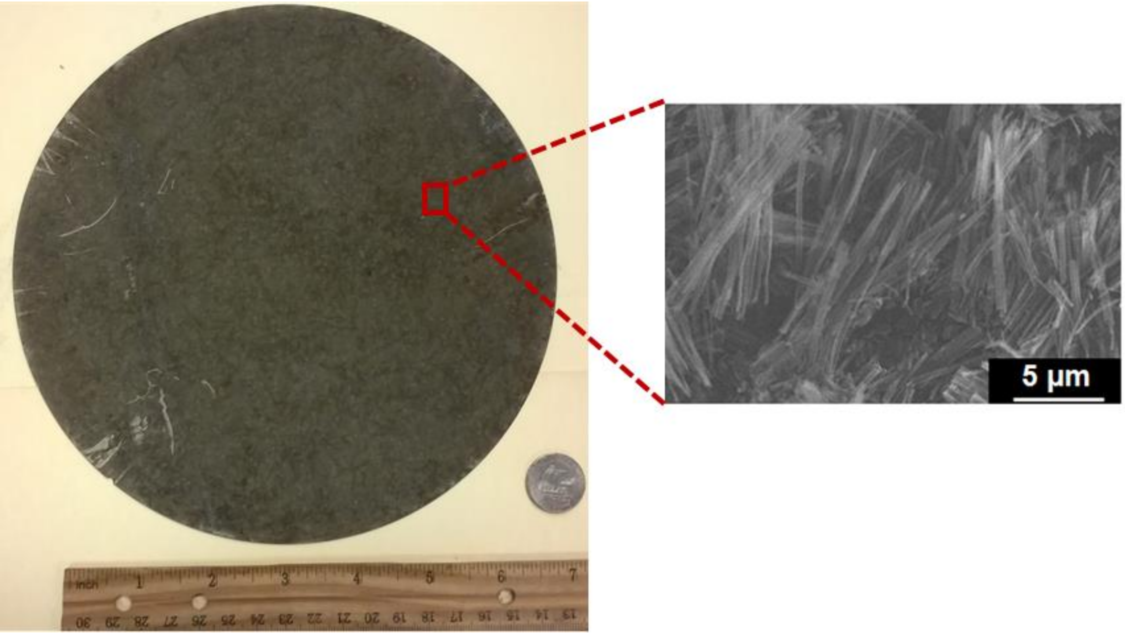

Figure 21 Silicon nanowires obtained from electroless etching of single crystalline (100) silicon wafers

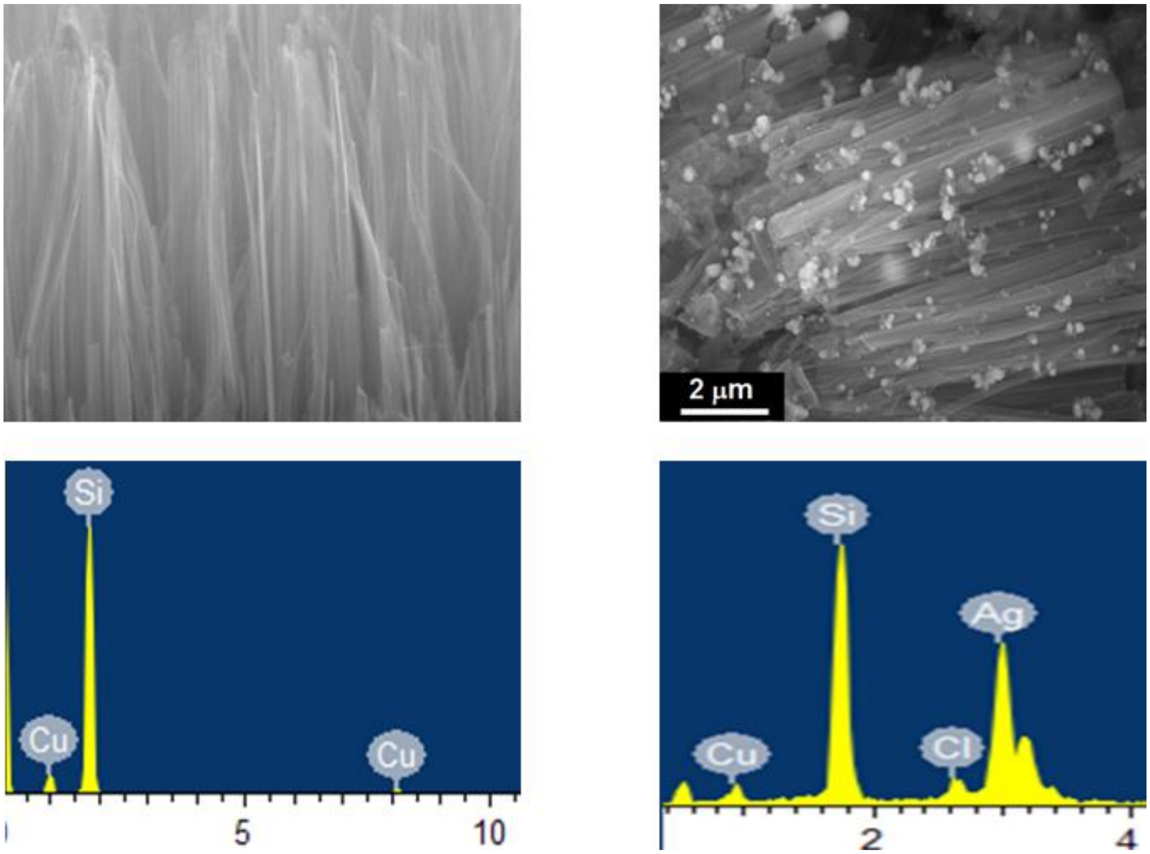

Figure 22 SEM image and corresponding EDS spectrum of particles observed on top of consolidated and aligned nanowire pellets. The particle is primarily composed of silver contaminant, a by-product obtained during the electroless etching of silicon wafers into nanowires

CHAPTER V

SIMULTANEOUS ALIGNMENT AND CONSOLIDATION OF RIGID NANOWIRES VIA SHEAR FORCE USING EQUAL CHANNEL ANGULAR EXTRUSION*

Achieving robust and high density pellets (relative density greater than 90%) is essential to obtaining reliable thermoelectric characterization of the nanowires.[131] In addition to retain the novel properties of nanowires, after the assembly the pellet fabricated from the nanowires must retain their morphology. Aligning of nanowires achieved both the above requirements. In addition, such an assembly provides a highway for electrons transport while scattering the phonons, which increases the electrical conductivity and reduces the thermal conductivity.[132] Aligning the nanowires in a thermoelectric device allows us to not only exploit the anisotropic properties of nanowires but also pack them into high-density pellets (greater than 98%).[133, 134] Abreu *et al.* reported that the maximum density achievable by a random packing of nanorods is only 57%.[135] In order to achieve a highly dense arrangement of the faceted nanowires, the nanowires have to be aligned. As thermoelectrics need high electrical conductivity and low thermal conductivity, aligning the nanowires will scatter the phonons in the directions perpendicular to the axis of the nanowire (thereby decreasing the thermal conductivity) while providing a single-crystalline electron pathway (thereby having a high electrical conductivity).[65]

---

*Reproduced with permission from “Shear Induced Simultaneous Consolidation and Alignment of Silicon Nanowires into Ingots using Equal Channel Angular Extrusion” V. Vasiraju et al., 2015, *Materials Research Express***,** *2*, 015013 © 2015 by IOP Publishing. All rights reserved

Introduction

Nanowires have been envisioned and demonstrated to be the fundamental building blocks for the fabrication of next-generation electronic and photonic devices.[136-143] Materials in nanowire format offer the unique ability to tailor their electrical,[141] mechanical,[144] electronic[140] and optical[145] properties, unlike their counterparts in bulk form.[146] Tailoring the dimensions of materials in nanowire form (i.e., varying the lengths and diameters of nanowires) not only allows for precisely tuning their electronic and optical properties, [147, 148] but also brings to the fore of hitherto-unknown novel properties they exhibit.[34, 149, 150] Utilization of any novel properties observed in nanowire form of materials requires strategies for assembling them in a bottom-up fashion into devices.[151] Such bottom-up assembly strategies are expected to overcome the technological and economical limitations posed by traditional lithography and other top-down approaches for device fabrication.[152-157] In fact, a large number of studies explored the use of nanowire form of materials in electronics[141, 158], photonics,[159] optics,[160] and also in other mechanical devices.[34] Superior performances have been reported in nanowire-based energy conversion devices such as thermoelectric[102], solar cells,[161] photo-,[162]bio- [163] and chemical-detectors,[164] for example, a 100-fold increase in thermoelectric performance has been reported in thin silicon nanowires.[102] Similarly, efficiencies in nanowire-based solar cells are consistently reported to be on the rise because of increased optical path, photon trapping through multiple scattering and decreased reflections.[165] Single-photon nanowire based detectors have been reported, which stand as a testimony for the efficiency of materials in nanowire format.[166] Finally, nanowires have also been employed successfully as plasmonic wave guides,[167] efficient biosensors,[164] bio-chemical sensors, lasers[168, 169] and DSSC's [170, 171].

A common thread in all the above-mentioned studies is the fact that they mostly characterize the performances of single nanowires.[102, 129, 172, 173] Reports indicating that the unique characteristics exhibited by individual nanowires are extendable to bulk devices composed of multiple nanowires are scarce.[144] This is readily supported by the fact that no bulk/macro devices fabricated from nanowire building blocks are currently commercially available. Realizing such devices needs huge leaps in the progress on the strategies useful for the mass production of nanowires, and strategies that allow for their assembly into various configuration on demand.[174] In a previous report, our group has addressed one of these issues, we have described a catalyst and template-free method for the mass production of compound semiconductor nanowires from elemental solid sources.[127] More specifically, mass production of zinc phosphide (Zn_3P_2) and zinc antimonide (Zn_4Sb_3) nanowires from zinc foils and phosphorus/antimony powders was reported. In subsequent reports, we have described assembly of nanowires into high density pellets.[144] As described in these reports, the enhanced flexibility offered by thin nanowires allowed for the assembly of nanowires in a randomly oriented fashion into highly dense pellets, while also allowing for the retention of their morphologies.[144] High packing fraction of nanowires is important to avoid inconsistent device performance and ensure long-term device stability.[133] However, gaining any insight into and utilizing the anisotropic properties of single-crystalline nanowires requires their assembly in an oriented fashion into highly dense pellets.[107]

Nanowire alignment has been center of many studies[175] and has been achieved by application of magnetic field,[176-178] electric field,[108, 179] fluid flow[180, 181] and shear force.[151] Though consistent alignment within ± 20^o variation has been achieved using these methods, nanowire compaction was not accomplished. The aligned nanowires were always spaced apart and not compacted in these studies. Even though some applications may need the large inter spacing between nanowires, they require expensive lithography techniques to address individual nanowires in the aligned assembly before devices could be fabricated from them. At the core, this goes against the primary advantages of bottom-up assembly of nanowires into devices, namely cost reduction and high throughput. Mechanical printing overcomes some of the problems plaguing field flow approaches, but is still limited by problems in density and alignment ratios.[182, 183] These limitations necessitate the need for developing strategies that create highly dense assemblies (>90% material density) of aligned nanowires. In other words, strategies for the simultaneous consolidation and assembly of nanowires are essential. Contextually, the main goal of this manuscript is the same, achieving the simultaneous consolidation and assembly of nanowires into bulk ingots composed of highly dense and aligned nanowires. More specifically, use of equal channel angular extrusion (ECAE) for the simultaneous consolidation and alignment of large quantities of silicon nanowire powders is described in detail in this manuscript.

Application of simple shear was chosen for the simultaneous consolidation and alignment and consolidation of nanowires over tensile and compressive forces due to the following reasons. Processes based on tensile forces, such as wire drawing, would align the nanowires. However, they do not allow for the consolidation of the nanowires into highly dense compactions.[184] Processes based on compressive forces, such as hot uniaxial pressing, on the other hand do consolidate nanowire powders into stable and robust compacts. However, they do not impart any alignment to the nanowires. In sharp contrast, ECAE could be used to both impart high amounts of texture (i.e. better chance for nanowire alignment) and also to consolidate the nanowires.[185, 186] Briefly, ECAE is a shear deformation technique for texture development and microstructure refinement.[110] In a typical ECAE process, a well lubricated metal bar (billet) filled with microcrystalline/nanocrystalline powders is pushed through a rigid metallic die (extrusion) that has two identical channels whose axis intersect at an angle (90^0 in this case).[187] Simple shear occurs at crossing plane intersection as shown in the schematic in Figure 23 and this shear is responsible for microstructure refinement and texture development.[188] As the cross-section of the billet before and after processing remains same, the extrusion can be done any number of times, imparting huge strains on the billet. Each extrusion of the billet through the metallic die is called a 'pass'. It is also possible to processes the microcrystalline/nanocrystalline powders by either rotating the billet relative to the die or opting to keep the orientation of the die relative to the billet the same between different passes. Route A processing uses the latter strategy and involves maintaining the orientation of the billet relative to the die the same between multiple passes. As already mentioned earlier, shear forces imparted to the nanowires through the copper billets surrounding them is expected to simultaneously consolidate and align the nanowires, with the alignment getting better as more and more shear force is applied.[107] Though an extensive amount of literature is available for consolidation and texture development of nanoparticles using

ECAE[189-194], literature discussing use of ECAE to consolidate or align nanowire powders does not exist.

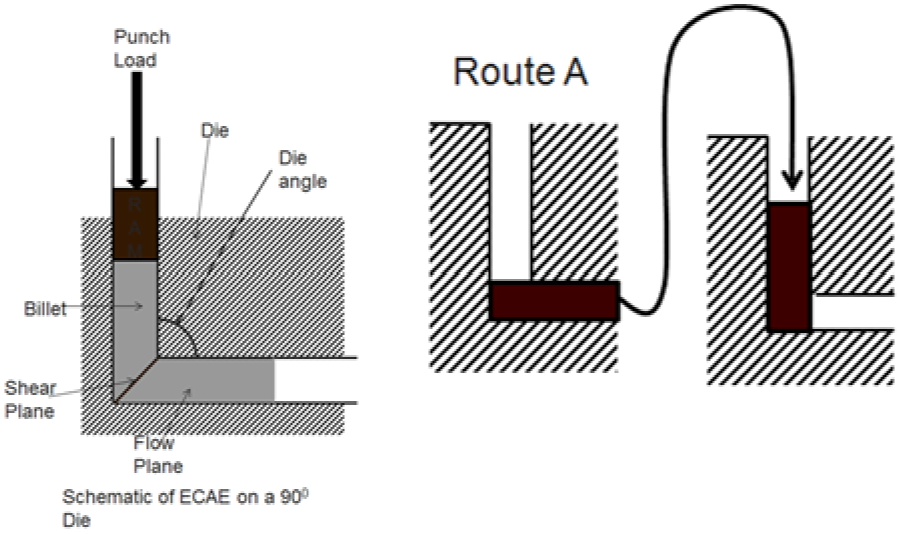

Figure 23 A schematic showing the basic working of equal channel angular extrusion

Only a few reports on ECAE of metal matrix carbon nanotubes exist.[195-197] The aim of these studies to increase the mechanical strength and hardness of copper-carbon nanotube composites.[198] No indication was provided regarding the alignment of the carbon nanotubes in the composites.

Materials and methods

Gram quantities of silicon nanowires necessary for the ECAE experimentation were obtained using electroless etching of single crystalline silicon wafers as reported previously.[199-201] These wafers were rinsed with acetone and cleaned using piranha solution (a mixture of 1 part Hydrogen peroxide (H_2O_2) and 3 parts sulfuric acid (H_2SO_4) solution) for 15 minutes. Following the cleaning, the wafers were treated in 5M Hydrofluoric acid (HF) for 3 minutes to remove the native silicon oxide layers on the wafers. Following this, the wafers were electroless etched with a mixture of 1 part 5 M Hydrofluoric acid (HF) and 1 part 0.04 M silver nitrate ($AgNO_3$) solution 30 minutes at 50^0C for forming silicon nanowires on their surfaces. Subsequently, the electroless etched wafers containing the nanowires were treated with 1:1 ratio by volume of nitric acid (HNO_3, 70% w/w) and hydrochloric acid (30% w/w), for one hour to remove any excess metallic silver. The nanowires were then scraped off the wafers using a blade and collected as powders. The silicon nanowires obtained using this procedure typically had diameters in the 20-100 nm range and lengths of 10 µm.

For the ECAE experimentation, a 1 inch x 1 inch x 6 inch copper 101 stock (obtained from McMaster Carr, Inc.) was used as the billet. Copper was specifically chosen as the billet material not only because of its excellent room temperature ductility[202] and good machinability but also because of its abundance and wide availability. It is worthwhile to add here that other metals could also be used as billet, in addition to copper.[187] Two holes 1/8th inch diameter and 3 inches deep were drilled into the copper billet as depicted in Figure 24(b). 0.2 grams of silicon nanowires were filled into each of these holes, followed by covering them using copper wire of the same diameter as the hole. Any excess copper wire was then cut flush to the top surface of the billet. The top of the wire was then welded to the billet using metal inert gas (MIG) welding, using argon as the inert gas. This welding ensured that the structure remained stable during the extrusion. This nanowire filled copper billet was extruded at a rate of 0.01 inches/second at room temperature, which required a maximum pressure of 690 MPa. The extrusion was performed using four passes in route A. A pictorial representation of the state of the billet and the nanowires within it as the extrusion proceeds is presented in Figure 24(c). The rectangular cross-section of the element containing the nanowires is distorted into a parallelogram due to the shear forces as the billet is extruded. However, the billet containing the nanowires retains its original square cross section.[203] This is because the inlet and outlet channels of the die are of the same cross-section (rectangular). After the processing the billet was cut open using a slow rotating diamond saw and the copper surrounding the consolidated nanowires was etched in concentrated HNO_3 to expose the oriented and consolidated silicon nanowire pellets. Both the as-obtained nanowires and the consolidated silicon nanowires were characterized using electron microscopy (SEM), Energy dispersive spectroscopy (EDS) and X-ray diffraction (XRD). Densities of the consolidated nanowire pellets were determined using Archimedes principle.

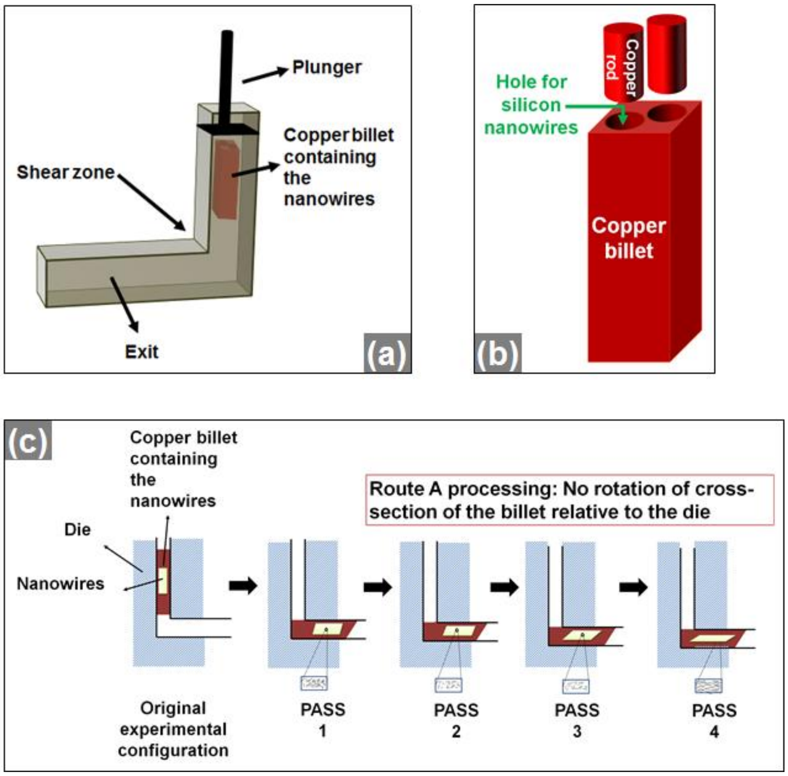

Figure 24 Schematic representing (a) ECAE experimental setup, (b) billet used for the ECAE experimentation, and (c) steps involved in Route A processing of nanowires.

Results and discussion

Optical micrographs of a copper billet during various stages of ECAE are depicted in Figure 25. In addition, micrographs of the silicon nanowire powder, copper billet and copper wires used as initial raw materials for processing the nanowires, along with those of a consolidated silicon nanowire pellet are also depicted in Figure 25. As is clearly evident from Figure 25, the processing of silicon nanowires powders using ECAE resulted in the formation of robust and free-standing nanowire pellets. Measurements of the consolidated nanowire pellets indicated that on an average they exhibit densities of 2.12 g/cm^3. This is approximately 90% of the theoretical density of silicon (density of silicon is 2.32 g/cm^3). This indicates that ECAE consolidated the nanowires powders into pellets of fairly high packing densities. This result also serves as indirect evidence of the alignment of the nanowires within the pellets, as randomly oriented nanowires cannot be pressed into such highly dense pellets. Scanning electron micrographs of a silicon nanowire pellet are presented in Figure 26 (b) and (c). For comparison, an SEM micrograph of as-obtained silicon nanowires is presented in Figure 26(a).

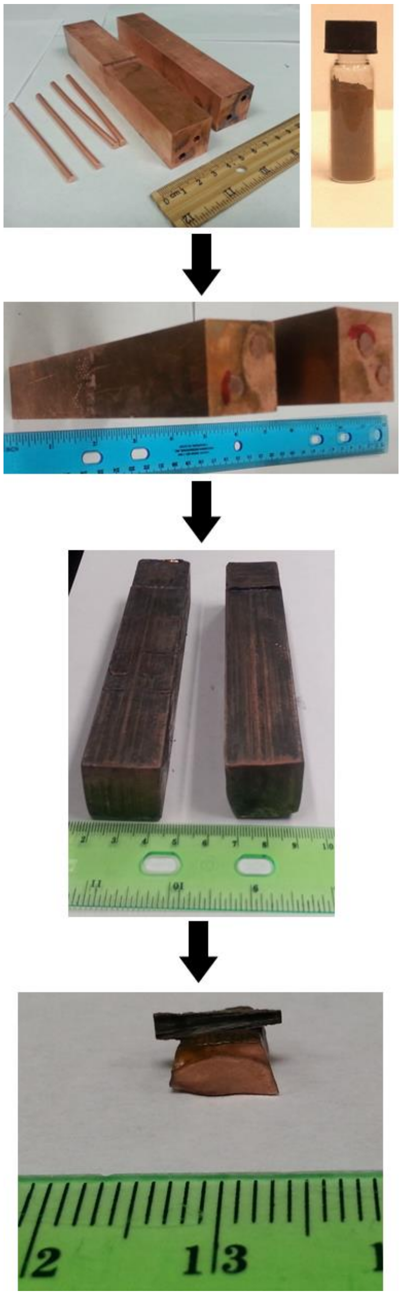

Figure 25 Optical micrographs representing all the steps involved in the simultaneous consolidation and alignment of nanowires using ECAE. (a) Raw materials used for consolidating and aligning nanowires, including copper billet, silicon nanowire powders and copper rods, (b) billet containing the copper nanowires before ECAE, (c) copper billets after ECAE processing, and (d) silicon pellet obtained by the ECAE.

The analysis of the pellets confirmed the dense packing and consolidation of the nanowires Figure 26(b & c)). In addition, some regions of the pellets indicated alignment of the nanowires in the shear direction Figure 26(b & c)). The nanowire alignment observed is not believed to be an artifact, as the nitric acid etching procedure employed for removing copper surrounding the consolidated and aligned nanowire pellet is not expected to react or otherwise disturb the configuration of the silicon nanowires in the pellets. The angular mismatch between the shear direction and the direction of alignment of the nanowires is observed to lower than 5^{o}. Such orientation of the nanowires was across the sample at multiple locations. The SEM analysis indicated no major loss of the nanowire morphology (breaking of the nanowires into nanoparticles was observed to be minimal, if any). The bright particles seen on the surfaces in the Figure 26(b & c) are believed to silver contaminant generated during the electroless etching of silicon nanowires to produce nanowires. EDS analysis of the pellets confirmed this conclusion (Figure 28). In such highly dense nanowire pellets, it is entirely possible that the consolidation process obscures the grain boundaries between the nanowires. In such a scenario, it is essential to delineate the grain boundaries to precisely determine the orientation of the nanowires relative to each other. Typical scanning electron microscopes do not have the resolution necessary to delineate the grain boundaries between the nanowires. To obtain this information, destructive analysis of the nanowires was performed. For this purpose, partial etching of the grain boundary between the nanowires in the pellets, followed by scanning electron microscopy was performed. As the grain boundaries between the nanowires in the pellets are primarily composed of silicon oxide, well-known silicon oxide etching procedure involving the use of HF acid aqueous solution was employed. Partial etching of the grain boundaries using mild HF solution, as expected, revealed the boundaries between the nanowires in pellets and clearly confirmed the alignment of the nanowires (Figure 26 (d)). However, prolonged etching of the grain boundaries using concentrated HF solution led to the complete disintegration of the pellets into powders. The disintegration of the pellets clearly indicated that no sintering /welding of the nanowires occurring during the ECAE. It is believed that the mechanical stability of the nanowire pellets is owed to the interlocking of their rough surfaces during ECAE, as explained below.

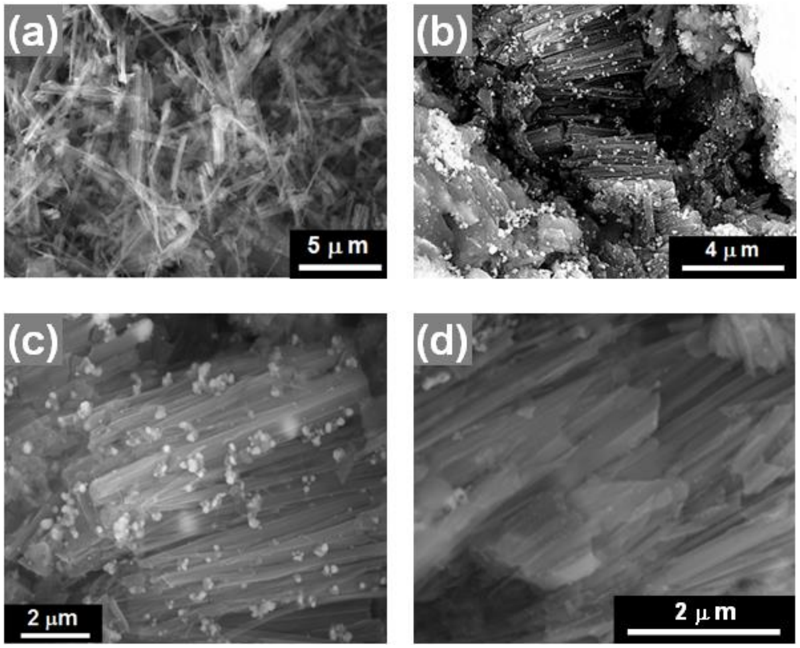

Figure 26 Scanning electron micrographs of (a) as-obtained nanowires, (b) and (c) as-obtained aligned and consolidated nanowires obtained by ECAE, and (d) aligned and consolidated silicon nanowires after grain boundary etching. Images shown in (b) and (c) are obtained from consolidated and silicon nanowire pellets.

Typically, consolidation of anisotropic crystals (e.g., nanowires) into highly dense pellets, while also ensuring that their morphologies are retained within the pellets, is only possible under two different scenarios. In the first scenario, mechanical flexibility of the nanowires is a requirement. In a previous study, we have demonstrated that enhanced flexibility afforded by ultrathin Zn_3P_2 nanowires allows for their consolidation into highly dense pellets. In this case, the intertwining of the nanowires makes the resulting pellets robust. In cases where the nanowires are brittle, simple hot pressing of randomly oriented nanowires does not result in highly dense pellets. High density is only possible if the nanowires break along their lengths into nanoparticles. This defeats the primary purpose of synthesizing materials in nanowire form for studying their anisotropic properties. The silicon nanowires employed in the current study are brittle in nature. This is because the nanowires made by electroless etching, although thin, are not expected to be defect-free.[204] In such cases, consolidating them without destroying their wire morphology requires aligning them. In fact, faceted nanowires when consolidated in an aligned fashion could be theoretically packed into 100% dense pellets. ECAE allowed us to accomplish this task. The mechanical robustness of the nanowire pellets in this case is believed to be due to the interlocking of the rough surfaces of the silicon nanowires obtained by electroless etching (Figure 27).[102] This is clearly supported by the etching experiments. When the rough grain boundaries of the nanowires are etched using HF/water mixtures, the silicon oxide at the grain boundaries is removed and this further leads to the loss of the interlocking mechanism. Consequently, the pellets disintegrate into powders. As all the processing was done at room temperature, no sintering or grain growth is expected during ECAE, unlike that occurs during the consolidation of materials using traditional powder consolidation techniques. As mentioned above, the disintegration of the nanowires on prolonged etching in concentrated HF etching clearly confirmed that the sintering of nanowires did not occur during consolidation. It is entirely possible that in some cases the same surface roughness of the nanowires also prevents the alignment of the nanowires. The average surface roughnesses, if large, will prevent the sliding of the nanowires relative to each other on application of shear stress and prevent the alignment of the nanowires during the initial stages of consolidation. This essentially makes the nanowires consolidate in a random fashion without any alignment (Figure 26(b)). Further experimentation is necessary to precisely determine the processing conditions (number of passes, ECAE route etc.) and the characteristics of the nanowires (surface roughness, length etc.) necessary for consolidating and aligning nanowires all across the pellets. Nevertheless, these results indicate that it is possible to simultaneously consolidate and align nanowires using ECAE. ECAE strategy for simultaneously consolidating and aligning nanowires, coupled with the strategy we recently developed for welding nanowires,[205] is expected to lead to aligned and welded nanowire ingots highly useful in the fabrication of energy conversion devices, such as thermoelectrics.

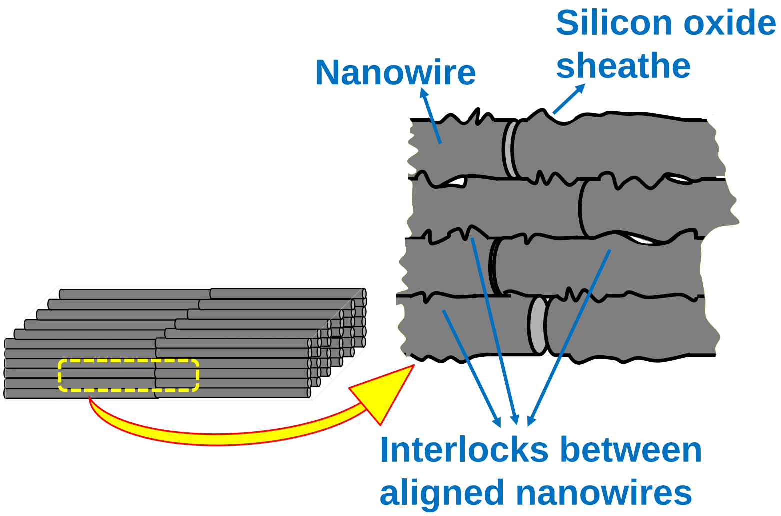

Figure 27 A schematic representing the mechanism proposed to explain the mechanical robustness of the consolidated and aligned nanowire pellets. The interlocking of the rough surfaces of the electroless etched nanowires is believed to be responsible for the robustness of the pellets

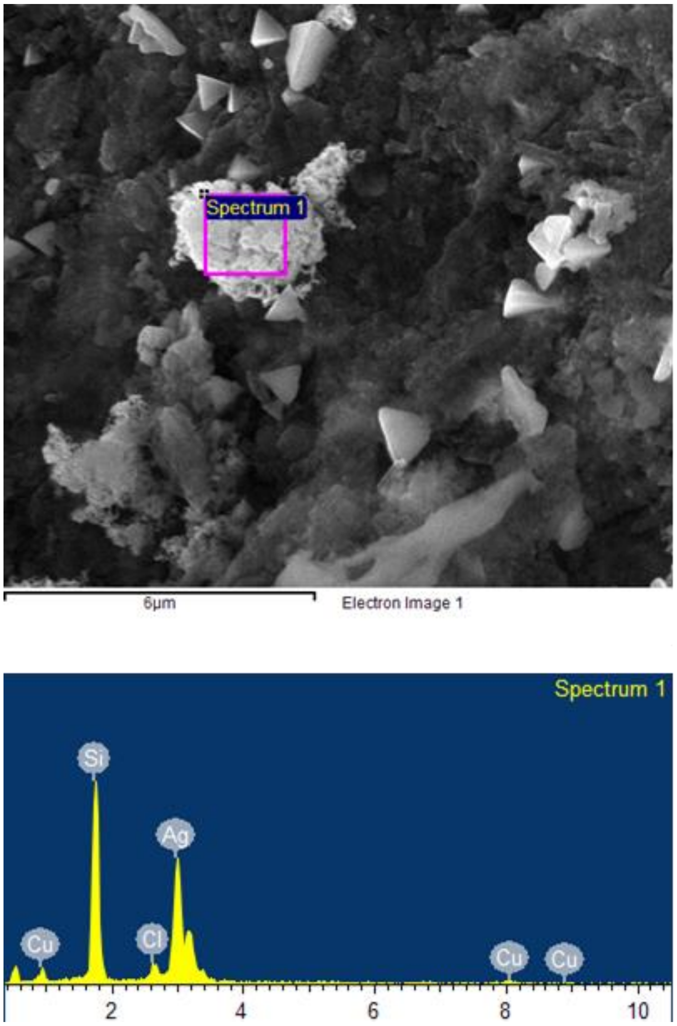

Figure 28 SEM image and corresponding EDS spectrum of particles observed on top of consolidated and aligned nanowire pellets. The particle is primarily composed of silver contaminant, a by-product obtained during the electroless etching of silicon wafers into nanowires

Conclusions

In conclusion, the possibility of simultaneously aligning and consolidating mechanically rigid nanowire powders for obtaining highly dense ingots (or pellets) of aligned nanowires was studied. ECAE of silicon nanowires obtained by electroless etching was employed for this purpose. The results indicated that ECAE could be employed for consolidating nanowires into highly dense and robust nanowire pellets, without destroying their morphologies. As this is a room temperature process, no major changes to the dimension of the nanowires were observed. This is unlike traditional hot pressing techniques where consolidation of powders leads to grain growth via sintering and the alteration of the dimensions of the particles composing the powders. In addition to consolidation, nanowire alignment was also observed in a few regions of the pellets. Based on the results, it was postulated that the interlocking of the rough surfaces of the nanowires is responsible for their mechanical robustness. Optimization of the processing conditions further is expected to lead to the complete alignment of the nanowires within the pellets. Such large-scale assemblies of aligned and consolidated nanowires directly in the solid state and without the use of any solvents or fluids are highly useful for utilization the anisotropic properties of nanowires and the fabrication of energy conversion devices, such as thermoelectrics.

CHAPTER VI

STABILITY ENHANCEMENT OF ZINC PHOSPHIDE, ZINC OXIDE AND MAGNESIUM SILICIDE NANOWIRES VIA NONCONFORMAL BORON NITRIDE DECORATION*

Introduction

Instability of inorganic compound semiconductors, especially nanomaterials, is a subject that has received very little attention, especially when compared to the volume of research that has been/being performed on nanomaterials synthesis, nanomaterial characterization and energy conversion device fabrication from these materials.[206-213] The need for addressing instabilities of compound semiconductor nanomaterials and devising strategies for overcoming such instabilities is illustrated below using three material systems as examples, zinc phosphide (Zn_3P_2), zinc oxide (ZnO) and magnesium silicide (Mg_2Si) nanowires.

Zn_3P_2, an inorganic compound semiconductor, is predicted to be highly useful in the bulk fabrication of photovoltaics (PVs).[214,215] It is not only composed of earth abundant elements, Zn and P,[25] but also has an ideal bandgap (E_g) of 1.5 eV [216] useful for obtaining highest possible efficiencies in single-junction PVs. It also has other characteristics ideal for the fabrication of PVs, including high electron diffusion lengths of ~10 μm reported in *p*-type Zn_3P_2, and a high absorption coefficient $>10^4$ cm^{-1}. [217-219] However, the instability of Zn_3P_2 prevents its widespread use in PV fabrication.[220].

---

*Reproduced by permission from "Non-conformal Decoration of Semiconductor Nanowire Surfaces with Boron Nitride (BN) Molecules for Stability Enhancement: Degradation-resistant Zn_3P_2, ZnO and Mg_2Si Nanowires" Vasiraju, V. R. K, et al., 2014 Physical Chemistry Chemical Physics, 16, 16150 © 2014 by PCCP Owner Societies

It is unstable not only in ambient air at room temperature, but also in vacuum at slightly elevated temperatures of 150-200 ^{o}C. When exposed to air, Zn_3P_2 reacts with both oxygen and moisture to form $Zn(OH)_2$ or $Zn_3(PO_4)_2$.[126] Processing Zn_3P_2 under vacuum for the fabrication of PVs (e.g., metal cathode deposition) also renders it unstable. It leads to loss of phosphorus from the Zn_3P_2 surfaces.[221] This inevitably leads to the formation of Zn-Zn_3P_2 interfaces dominating the electrical properties of the interfaces, irrespective of the type of metal deposited on their surfaces.[222] The loss of phosphorus is believed to occur due to the rearrangement of the surfaces, followed by the subsequent formation and sublimation of phosphorus in the form of P_4 molecules. In addition to oxygen and moisture from air, Zn_3P_2 also reacts with mild aqueous acid solutions. It reacts with mild HCl solution and forms $ZnCl_2$, along with the evolution of PH_3 gas. As rain water is acidic in nature (pH of rain water is typically in the 5.5-6 range), this corrosion of Zn_3P_2 renders any photovoltaic modules fabricated from it unsuitable for rooftop installation and long-term use. Similar instabilities are also observed and reported in other compound semiconductors, including metal arsenides,[223] antimonides [224] and oxides.[225]

ZnO, similar to Zn_3P_2, is also a well-known semiconductor with an E_g of 3.4 eV.[226] It has been reported that ZnO nanowires are useful in the fabrication of light emitting diodes (LEDs)[227], waveguides [228] and lasers,[229] dye-sensitized solar cells (DSSCs) [230] and biosensors.[231] Similar to Zn_3P_2, ZnO nanomaterial degrades (dissolves) in both acidic solutions of pH in the 4.5-5.0 range, basic solutions of ammonia and NaOH, and even in horse blood serum,[232] rendering it unsuitable for the fabrication of stable energy conversion devices.

Finally, Mg_2Si is a compound semiconductor highly useful in the fabrication of thermoelectrics modules. Similar to Zn_3P_2 and ZnO, Mg_2Si reacts with both water and mild acid solutions rendering it unsuitable for use in terrestrial thermoelectric device fabrication. To illustrate the instability of Mg_2Si, its reaction with water and aqueous HCl solution are presented below.[233, 234]

$$Mg_2Si+4H_2O \rightarrow 2Mg(OH)_2+SiH_4$$

$$Mg_2Si+4HCl\rightarrow 2MgCl_2+SiH_4$$

In the past, passivation of surfaces with organic molecules has been pioneered to enhance the stabilities of inorganic semiconductor surfaces.[235, 236] Both straight chain and conjugated molecules with various head groups have been employed for passivating semiconductor surfaces as reported in the literature.[237] These molecules act as barriers and prevent the diffusion of either oxygen or moisture to the semiconductor surfaces, thereby imparting them enhanced resistance against air- and moisture-assisted degradation.[206, 238] Although this strategy offers stability to semiconductors at low temperatures, it does not do so at high temperatures.[239] In addition, these organic molecules alter the interfacial properties of nanomaterials, especially when a multitude of these nanomaterials are assembled into devices. It is worthwhile to mention here that presence of molecules at the interfaces between assembled nanomaterials is not always a handicap. In fact, the presence of molecules has been employed to tune thermal and electrical transport through materials. Nevertheless the low stabilities of these organic molecules at high temperatures, necessitates the development of an alternate strategy for imparting stabilities to nanomaterials.

Therefore, the primary question that needs to be answered is whether a strategy could be developed to enhance the stabilities of compound semiconductors at both room temperature and moderately elevated temperatures. Of particular importance in the development of such strategies is ensuring that the stabilization process does not degrade/majorly alter either their electrical or electronic properties. The aim of this paper is to accomplish the same, namely the development of a strategy for making compound semiconductor nanowires stable both at room temperature and at moderately high temperatures. More specifically, surface decoration of Zn_3P_2, ZnO and Mg_2Si nanowires with small and highly stable inorganic boron nitride (BN) molecules is presented as a strategy for imparting them stabilities against water- and acid-assisted degradation. By the end, it will be demonstrated that BN molecule decoration of nanowire surfaces imparts them enhanced stabilities not only against moisture-assisted degradation, but also to acid-assisted degradation. It will also be demonstrated that such surface decoration does not adversely impact their electrical and electronic properties (e.g., the electrical conductivities and the E_g of nanowires). Such inorganic molecule decoration of semiconductor nanowire surfaces for making them corrosion resistant has never been reported in the literature. Only a lone report in the literature discussed the doping of semiconductors with salt molecules for enhancing their electrical conductivity.[240] That report did not mention whether salt doping of semiconductors made them resistant to degradation.

Experimental methods

Zn_3P_2 and ZnO nanowires necessary for this study have been synthesized using direct reaction schemes. This procedure was described in detail previously.[126] Direct reaction of zinc foils with either phosphorus or oxygen, respectively, was employed for the synthesis of Zn_3P_2 and ZnO nanowires. These nanowire synthesis experiments were performed in a hot-walled chemical vapor deposition (HWCVD) chamber, and in the presence of hydrogen. The zinc foils served as both the source of zinc and the substrate in these experiments. Following the synthesis, nanowires were brushed off the foils and collected as powders. The same HWCVD setup was slightly modified for obtaining BN molecule decorated Zn_3P_2 and ZnO nanowire powders. Experiments for obtaining BN molecule decorated nanowires involved an additional step of exposing the nanowires to a vapor of pre-decomposed B-tribromoborazine molecules immediately after the formation of nanowires, and before their removal from the vacuum chamber.[126] The supply of B-tribromoborazine molecules into the CVD chamber was accomplished by heating a stainless-steel bubbler containing the source powder to a temperature of 300 ^oC. The B-tribromoborazine vapor is then passed through a decomposition zone maintained at a temperature of 600 ^oC,[241] before it reacted with the nanowires. In order to prevent the complete conformal coating of the nanowires with either a monolayer or multilayers of BN, only minute amounts of B-tribromoborazine, ~30-40 mg, were employed per experimental run. The amount of B-triboromborazine employed in each experimental run was always lower than that theoretically required to form one monolayer of BN conformal coating on top of all the nanowire synthesized in that run. The nanowires obtained were characterized for morphology, phase, crystal structure and chemical composition using scanning electron microscopy (SEM), X-ray diffraction (XRD), transmission electron microscopy (TEM), and Fourier Transform Infrared Spectroscopy (FTIR). To understand the stabilities of BN molecule decorated nanowires, they were dropped in either deionized (DI) water or concentrated HCl solution (pH=3) for an hour, followed by decanting the mixtures to collect the nanowires and analyzing the so-obtained nanowires using electron microscopy and diffractometry. For comparison, as-obtained (or pristine) nanowires were also dropped into DI water and concentrated HCl solution, and the resulting residues were studied using microscopy and diffractometry. 4-point probe measurements of nanowires cast into thin mats by drop casting nanowire dispersions were employed for the measurement of their electrical conductivities. UV-Vis spectroscopy was employed to determine the E_g of the both the BN decorated and as-obtained nanowires.[226, 242, 243]

While the characterization of Mg_2Si nanowires was also performed using the methods mentioned above, their synthesis was performed using an alternate procedure. Mg_2Si nanowires both pristine and BN decorated were obtained by solid-state phase transformation of pre-synthesized silicon nanowires produced by electroless etching. This experimental procedure employed for obtaining Mg_2Si nanowires was described in detail in previously.[46, 125] For obtaining pristine Mg_2Si nanowires, phase transformation of as-obtained silicon nanowires was performed. BN decorated silicon nanowires (obtaining by exposing silicon nanowires to a vapor of decomposed B-tribromoborazine) were employed for obtaining BN decorated Mg_2Si nanowires.

Results and discussion

The stability of the non-conformally decorated Zn_3P_2 nanowires, ZnO and Mg_2Si nanowires, these nanowires were dipped in deionized water and 3pH acid solutions. Scanning electron micrographs of pristine and BN molecule surface decorated Zn_3P_2

nanowires are presented in Figure 29, respectively. As observed in the micrographs, the surface decoration of the nanowires, by itself, did not majorly alter either their morphologies or their dimensions. The diameters of both the pristine and BN decorated nanowires were observed to be approximately the same, in the range of 40-60 nm. A comparison of the XRD patterns of pristine and BN decorated nanowires (Figure 29c) indicated that they are both composed of only α-Zn_3P_2 phase. No traces of any crystalline BN phase was observed in the BN molecule decorated Zn_3P_2 nanowires. From the microscopy and the diffractometry analyses, it can be concluded that the BN decoration process did not result in the formation of thick, conformal BN coatings on top of the nanowires, as such thick BN coating of the nanowires would have significantly increased the diameter of the nanowires and indicated its presence in the XRD pattern. High-resolution TEM (HRTEM) and selected area electron diffraction (SAED) analysis of the pristine (Figure 29d) and BN decorated nanowires (Figure 29e) confirmed the conclusions drawn from the SEM and XRD analyses and indicated that they are primarily composed of α-Zn_3P_2 phase (Figure 29 (d & e), and that exposure of the nanowires to decomposed B-tribromoborazine did not lead to their conformal coating with BN (Figure 29 e). Furthermore, no formation of any nanoscale BN domains (or crystals) on top of the Zn_3P_2 nanowire surfaces was observed in the HRTEM analysis of BN decorated nanowires. Comparison of the HRTEM images of pristine and BN decorated nanowires (Figure 29 d and e, respectively) clearly indicated that their surfaces are different. Formation of amorphous $Zn_3(PO_4)_2$ sheathes, expected on top of pristine Zn_3P_2 nanowires and observed in a previous study by our group, was clearly reiterated in Figure 29d. In sharp contrast, the surfaces of BN decorated Zn_3P_2 nanowires did not indicate the presence of any $Zn_3(PO_4)_2$ sheathes (Figure 29e). This result gave a preliminary indication that BN decoration of Zn_3P_2 nanowires prevented the reaction of their surfaces with air and the formation of amorphous $Zn_3(PO_4)_2$ sheathes. Energy dispersive spectroscopy (EDS) of the samples was also performed to detect the presence of BN on top of the nanowires (not shown). The analysis indicated the presence of no BN, clearly demonstrating that the conformal coating of the nanowires with thick layers of either amorphous or crystalline BN did not occur.

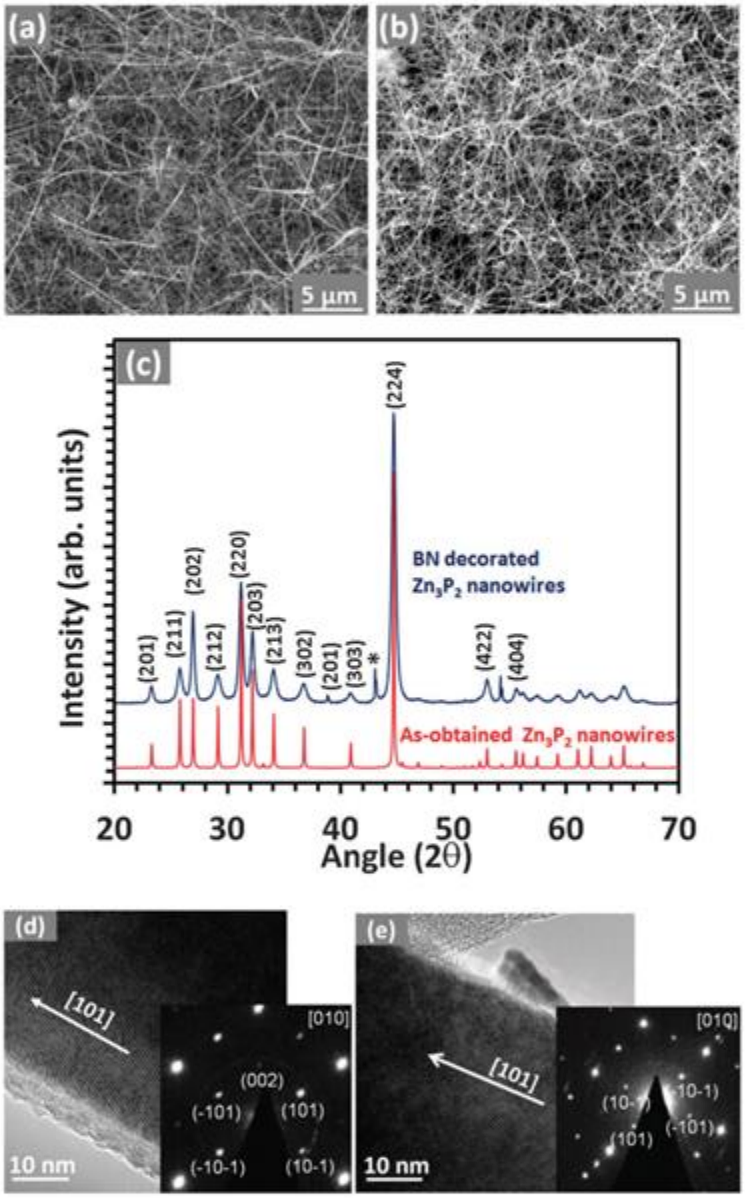

Figure 29 Scanning electron micrographs of (a) pristine Zn_3P_2 nanowires and (b) BN decorated Zn_3P_2 nanowires. No changes to the morphologies or the dimensions of the nanowires were observed after they were decorated with BN. (c) XRD spectra of both pristine and BN decorated Zn_3P_2 nanowires. In both the cases, the nanowires exhibited the α-Zn_3P_2 phase. Peaks corresponding to zinc foil substrate employed for the synthesis of nanowires are indicated with a * in the figure. Transmission electron micrographs and the corresponding SAED patterns of (d) a pristine and (e) a BN decorated Zn_3P_2 nanowire. TEM analysis also indicated that the nanowires exhibited [101] growth direction.

To further probe the effect of BN surface decoration on the stability of Zn_3P_2 nanowires they were exposed to water and concentrated HCl solution. Scanning electron micrographs of BN molecule decorated Zn_3P_2 nanowires after they were treated with deionized (DI) water and concentrated HCl solution of pH 3 for one hour are respectively presented in Figure 30 (a & b). In sharp contrast, pristine Zn_3P_2 nanowires indicated a complete degradation of the nanowire morphology after treatment with either DI water or HCl solution of pH 3 for an hour (Figure 30 c & d). The XRD spectra of the nanowires after DI water and acid treatments are presented in Figure 30e. These analyses clearly indicated that the morphology and the phase the BN decorated Zn_3P_2 nanowires remained unaltered after either DI water of acid solution treatment. HRTEM analysis of a BN decorated nanowire after it is treated with HCl solution of pH 3 for one hour is depicted in Figure 30f. The analysis indicated that the nanowire remained single-crystalline and retained its α-Zn_3P_2 phase.

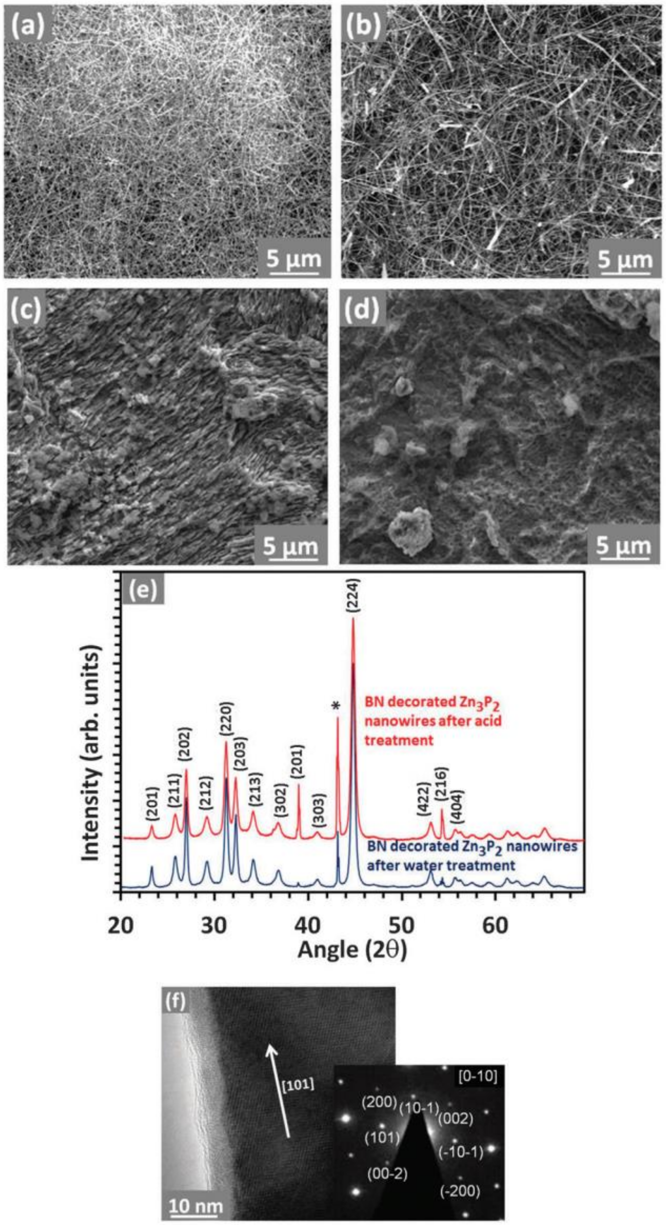

Figure 30 Scanning electron micrographs of BN decorated Zn_3P_2 nanowires (a) after they were treated in DI water and (b) HCl solution of pH 3. The nanowires retained their morphologies in both the cases. (c) and (d) SEM of pristine Zn_3P_2 nanowires after treatment with DI water and pH 3 HCl solution. Complete degradation of the pristine Zn_3P_2 nanowires was observed in both the cases. (e) XRD spectra of BN decorated Zn_3P_2 nanowires after they are treated with DI water and pH 3 HCl solution. Peaks corresponding to zinc foil substrate employed for the synthesis of nanowires are indicated with a * in the figure. (f) TEM micrograph of a BN decorated Zn_3P_2 nanowire after it was treated in pH 3 HCl solution.

To determine the presence of any minute quantities of BN on top of the Zn_3P_2 nanowires (that is below the detection limits of the TEM EDS detector), FTIR spectroscopic analysis of the BN decorated Zn_3P_2 nanowires was performed (Figure 31). For comparison, FTIR spectroscopy of pure B-tribromoborazine powders heated to a temperature of 600 ^{o}C was also performed and presented in Figure 31. The analysis clearly indicated the presence of BN in decorated Zn_3P_2 nanowires. Peaks at 744 and 919 cm^{-1} indicative of B-N-B bonds and B-N bonds are clearly observed in the spectra. In addition, peaks of cubic BN phase in the 1050-1065 cm^{-1} and the 1310-1340 cm^{-1} regions, and at 1078 cm^{-1} are clearly observed in the spectrum. Also, peak at 1019 cm^{-1} and 1400 cm^{-1} corresponding to explosive BN phase are also observed in the spectrum. Finally, peaks at 962 cm^{-1} corresponding to the wurtzitic phase of BN are also observed in the spectra.

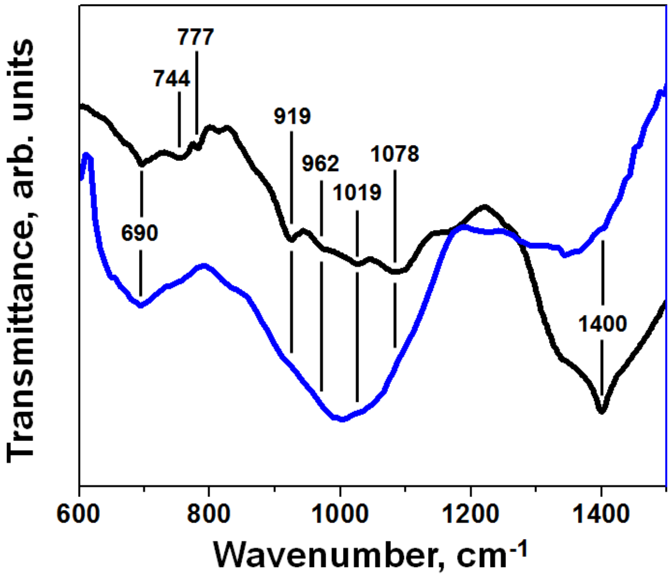

Figure 31 FTIR spectrum of BN decorated Zn_3P_2 nanowires indicating the presence of BN. For comparison, FTIR spectrum of decomposed B-tribromoborazine source is also included.

Overall, the analysis indicated that exposure of Zn_3P_2 nanowires to decomposed B-tribromoborazine results in the formation of non-conformal, ultra-thin BN coating on the surfaces. It is postulated that these non-conformal, ultra-thin BN coating is composed of multiple BN nanocluster islands or BN individual molecules. These nanoclusters or molecules are physically embedded on the surfaces/sub-surfaces of the nanowires (Figure 32), and not chemically bonded to the surfaces. When BN decorated nanowires are exposed to DI water or aqueous acid solutions, these BN clusters or molecules prevent the wetting of the nanowires by water or acid solution in their vicinity, and thereby prevent their degradation. Fairly large amount of literature supports the fact that BN coatings and films prevent wetting by many molten metal melts, non-metallic melts and aqueous solutions. Unlike conformal coating of nanowires with polymers and ceramics that result in the complete loss of interfacial electrical conductivity and the formation of electrically-insulating interfaces, this strategy is not expected to lead to the complete loss of interfacial electrical conductivity.

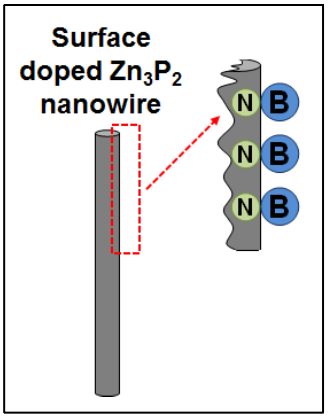

Figure 32 The proposed structure of BN decorated Zn_3P_2 nanowires. Exposure of Zn_3P_2 nanowires to a vapor of decomposed B-tribromoborazine is expected to lead to BN molecule getting embedded within the surfaces/sub-surfaces of the nanowires and the formation of BN decorated Zn3P2 nanowires

To ensure that the decoration of Zn_3P_2 with BN molecules did not alter the electronic and electrical properties of the nanowires UV-Vis spectroscopy and 4-point probe measurements have been performed. Tauc plots, generated from the variation absorbance ($\acute{\alpha}$) with frequency (v), of BN decorated Zn_3P_2 nanowires along with that obtained from pristine Zn_3P_2 nanowires, are presented in Figure 33. The Tauc plot clearly indicated that both BN decorated and pristine Zn_3P_2 nanowires have the same light absorption characteristics and that the E_g of both the as-obtained Zn_3P_2 nanowires and BN decorated Zn_3P_2 nanowires is 1.55 eV. This E_g values is close to that expected of Zn_3P_2.

The electrical conductivity of pristine Zn_3P_2 nanowire mats was observed to be 2.4 milli$\Omega^{-1}m^{-1}$. This value was very close to that observed in highly dense Zn_3P_2 nanowire pellets obtained by our group in a previous study.[144] The electrical conductivity of BN decorated Zn_3P_2 nanowire mats was observed to be lower, approximately 0.155 milli$\Omega^{-1}m^{-1}$. This result confirms the previous conclusion that Zn_3P_2 nanowires are not conformally coated with BN layers. Had the nanowires been coated conformally with electrically-insulating BN layers, they would not have exhibited any measurable electrical conductivity, a fact support by multiple previous studies.[244] BN is an insulating material with a band gap of 6 eV and is used in the fabrication of ultrathin insulators and as gate dielectric material. Studies on electrical properties of monolayers and multi layers of boron nitride sheets have reported a large electric potential, on the order of 10^6 V/cm, is required for the BN layers to show measurable current. The required break down voltage is 5 orders of magnitude higher than the voltages employed in our measurements (a maximum electric potential of 5V/cm was employed in our measurements), clearly underlying that the conformal coating of the nanowires with BN did not occur in our experiments.

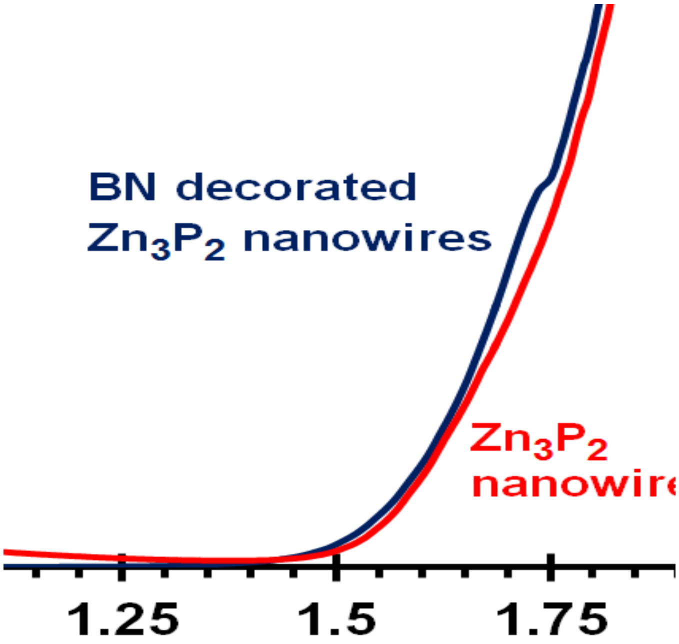

Figure 33 A Tauc plot of both pristine Zn_3P_2 nanowires and BN decorated Zn_3P_2 nanowires. The plot indicted no change in the Eg of Zn_3P_2 nanowires on decoration with BN molecules. The Eg of both pristine and BN decorated Zn_3P_2 nanowires remained 1.55 eV.

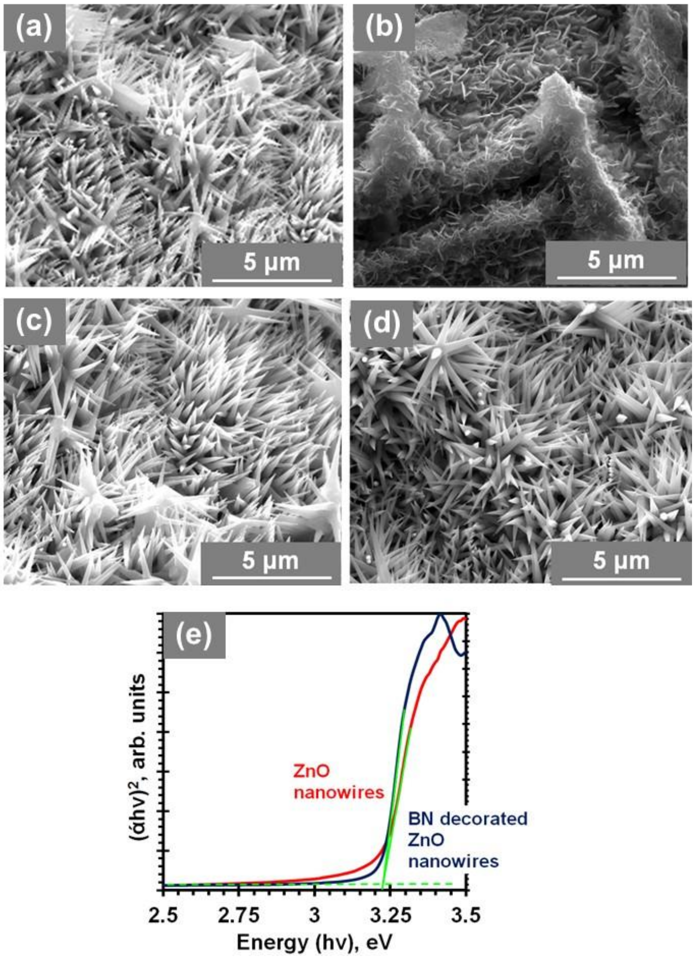

Figure 34 (a) (a) Scanning electron micrographs of (a) as-obtained ZnO nanowires, (b) as-obtained ZnO nanowires after treatment with pH 3 HCl solution, (c) BN decorated ZnO nanowires, and (d) BN decorated ZnO nanowires after pH 3 HCl solution treatment. From the micrographs, it is clear, beyond doubt, that BN decoration of ZnO nanowires imparted them stability against acid-assisted degradation. (e) Tauc plot of both pristine and BN decorated ZnO nanowires. The plot indicated that the decoration process did not majorly alter the Eg of ZnO nanowires.

To further confirm the universal applicability of this procedure for stabilizing nanowires of compound semiconductors, study of the stabilities of BN decorated ZnO and BN decorated Mg_2Si nanowires was also performed. The results of these experiments were along expected lines and indicated that BN decoration of ZnO nanowires imparted them stability against acid degradation, without altering their E_g (). Scanning electron micrographs of pristine ZnO nanowires and BN decorated ZnO nanowires before and after treatment in HCl solution of pH 3 are presented in Figure 34(a) to (d). As is clearly evident from the figures, BN decoration aided in preserving the morphologies of ZnO nanowires, even when they are exposed to strong acids. It is essential to mention here that ZnO nanowires are known to dissolve in acidic solutions. Tauc plots obtained from UV-Vis spectroscopic measurements of both pristine ZnO nanowires and BN decorated ZnO nanowires also indicated no variation in the E_g of ZnO nanowires, even after BN decoration (Figure 34e).

Finally, non-conformal decoration of Mg_2Si nanowires with BN also reiterated that this procedure imparts stabilities to the nanowires against acid-assisted degradation (Figure 35). As is clearly depicted in Figure 35, BN non-conformal decoration of Mg_2Si nanowires imparted them enhanced stabilities against acid-assisted degradation. Both the composition and the morphology of the Mg_2Si nanowire remained unaltered after their treatment with pH 4.5 HCl acid solution (Figure 35). In sharp contrast, bare Mg_2Si nanowires were completely etched by the pH 4.5 HCl acid solution employed in these studies. As the synthesis of these nanowires involved the solid-state diffusion of magnesium into BN decorated silicon nanowires, these final set of experiments also confirm that the decoration procedure did not conformally coat the nanowires. If the nanowires had been coated with either a complete monolayer or multilayers of BN, then magnesium would not have diffused into the nanowires and this would have prevented the formation of Mg_2Si nanowires.

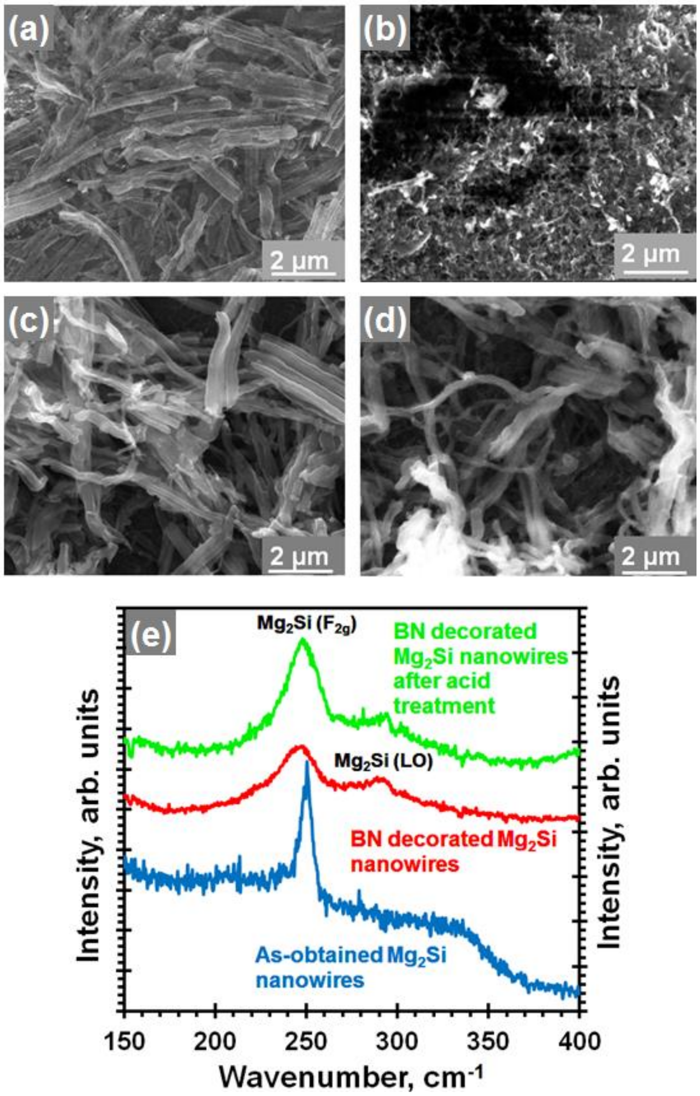

Figure 35 Scanning electron micrographs of (a) as-obtained Mg_2Si nanowires, (b) as-obtained Mg_2Si nanowires after acid treatment, (c) BN surface decorated Mg_2Si nanowires, and (d) BN surface decorated Mg_2Si nanowires after acid treatment. It is very clear from the figure (b) and (d) that BN surface decoration imparted resistance against acid-assisted degradation to Mg_2Si nanowires. (e) Raman spectra of the nanowires indicating that the nanowires are indeed composed of Mg_2Si and that they retained the same composition after BN decoration and acid treatment.

Conclusions

To summarize, a novel strategy for stabilizing the surfaces of compound semiconductors is presented. This strategy primarily involved the use of the non-conformal decoration of the surfaces of compound semiconductor nanowires with small inorganic molecules of BN, experimentally accomplished by exposing Zn_3P_2 and ZnO nanowires to a vapor of decomposed B-tribromoborazine *in-situ* in a chemical vapor deposition (CVD) chamber immediately after their synthesis. By controlling the amount of B-tribromoborazine employed for this purpose, conformal BN coating of the nanowires is prevented. For the synthesis Mg_2Si nanowires non-conformally decorated with BN molecules, a slightly alternate procedure was employed. Here, BN surface decorated silicon nanowires were phase transformed into BN surface decorated Mg_2Si nanowires. It is hypothesized that the decoration process is expected to embed BN molecules within the surfaces/sub-surfaces of the nanowires. These molecules are expected to prevent the wetting of the surfaces by either water or aqueous acidic solutions and hence prevent their degradation. The decoration process did not majorly alter the electronic properties of the nanowires. UV-Vis measurements of the nanowires before and after BN decoration clearly indicated no change in the E_g of Zn_3P_2 and ZnO nanowires. 4-point probe electrical conductivity measurements of the nanowires indicated that the stabilization procedure allowed for retaining the electrical conductivity between nanowires when assembled, and confirmed earlier conclusion that this procedure employed did not result in nanowires conformally coated with BN layers. This novel method of stabilizing nanowires, along with our recent reports on the strategies for the large-scale synthesis and assembly of nanowires, is expected to be of huge importance in the energy conversion device fabrication field as the instability of compound semiconductors nanowires is a major deterrent in their widespread use in the fabrication of the above-mentioned devices.

CHAPTER VII

THERMAL ENGINEERING IN NANOWIRE AND MICRON PARTICLE ASSEMBLIES VIA NONCONFORMAL BN DECORATION

Introduction

Enhancing thermal dissipation through materials (via increased thermal conductivities) has been a key hurdle in realizing performance-intensive electronic devices, such as microprocessors [245-248] and graphic cards.[249-251] On the other hand, insufficient reduction in the thermal conductivities of materials without any associated loss in electrical transport through them has been a major deterrent in achieving highly efficient thermoelectric devices.[252-254] Therefore a multitude of both theoretical and experimental research efforts have focused on both increasing the thermal conductivities of materials for better thermal dissipation,[255-257] and reducing the thermal conductivities of materials for increased thermoelectric efficiencies.[258, 259] These efforts include modifying defects in materials, strain engineering,[260-262] nanostructuring of materials, and fabricating composites from two or more materials.[263-266] Amongst these, engineering thermal engineering of materials by mixing/hybridizing them with materials that are good thermal conductors for fabricating composites that have enhanced thermal conductivities has received tremendous attention. In addition, nanostructuring of materials for reducing their thermal conductivities has received a lot of attention in the field of thermoelectrics research.[33, 80, 267, 268] With regards to thermoelectrics, the ability to selectively reduce lattice thermal conductivities (κ_l) through phonon confinement and phonon scattering (and hence overall thermal conductivities) of materials through nanostructuring has been found to be an indispensable tool in the fabrication of highly efficient thermoelectrics.[269, 270] In a series of publications, our group has also exploited this concept for designing thermoelectrics from bulk assemblies of Zn_3P_2 and ZnO nanowires.[131, 271, 272] In sharp contrast, the same nanostructuring approach was employed for increasing thermal conductivities of materials in the composites literature.

First and foremost, that exhibit enhanced thermal conductivities (compared to those observed in the standalone polymer matrices).[273] Use of BN in nanostructured form has not only allowed for uniformly mixing BN and polymers or other matrices in these cases,[274] but also in enhancing the thermal conductivities of the resulting composites.[273, 275-277] Therefore, nanostructuring was not observed to majorly lower the thermal conductivity of BN and stands in contrast to the observed lowering in the thermal conductivities of semiconductors on nanostructuring. In fact, nanomorphologies of boron nitride (BN), i.e., nanosheets, nanotubes and nanoparticles, have been increasingly researched upon for their excellent thermal conductivities.[278, 279] Nanomaterials of BN are not only inert, but also electrically insulating counterparts to carbon nanotubes (CNT's) and graphene.[280, 281] BN nanotubes have theoretically been predicted to have higher thermal conductivities than those of CNTs (3000 $Wm^{-1}K^{-1}$),[282, 283] which are orders of magnitude higher than those of bulk BN (thermal conductivity of bulk h-BN is 400 $Wm^{-1}K^{-1}$ at room temperature).[284] It is worth noting that the lattice thermal conductivity of single layer of hexagonal BN was predicted to be more than 600 $Wm^{-1}K^{-1}$ at room temperature.[285] Overall, reports in the literature indicate that BN is thermally conductive not only in the bulk form, but also in nanostructured form. However the highest thermal conductivity experimentally measured for multilayered (11-12 atomic layers) *h*-BN was reported to be 360 $Wm^{-1}K^{-1}$.

Secondly, a review of the literature also shows that inorganic-organic hybrids, unlike composites, exhibit novel properties that do not proportionally increase or decrease with compositional variations. For example, thermoelectric power factors of PEDOT:PSS-tellurium nanowire hybrids were found to be completely different and higher than those of the individual components.[286] In this case, the electrical conductivities of the hybrids were found be far higher than those of the two individual components.[287] However, no reports in the literature discuss that thermal conductivities of hybrids are lower than those of the components, especially in cases where BN nanostructures are one of the components.

In this context, it is important to determine whether conditions exist where mixing BN with a thermal insulator leads to the formation of hybrids (not composites) that exhibit thermal conductivities lower than those of both the components. In other words, it is important to know if addition of nanoclusters of BN to materials leads to enhanced phonon scattering at the boundaries and overall lowering of the thermal conductivities of the resulting hybrids. If so, it is important to deduce a pathway for obtaining such hybrids. Finally, it is necessary to determine the magnitude of the thermal conductivity lowering that could be achieved in the obtained hybrids. The aim of this paper is to accomplish the above-mentioned tasks, i.e., demonstrate a strategy involving non-conformal decoration of nanowire surfaces with BN for obtaining hybrids that have thermal conductivity lower than those of both the nanowires and bulk BN. Specifically, non-conformal surface decoration of Zn_3P_2 nanowires, followed by their consolidation into pellets, was employed as a strategy for obtaining the nanowire-BN hybrids in this paper. Non-conformal decoration of nanowires was previously employed by our group for imparting nanowires resistance against water- and acid-assisted degradation, without majorly altering their electrical and electronic properties in the process. In this report, the thermal conductivity behavior of the hybrids is determined and discussed.[288] In addition, extension and generalization of this strategy for obtaining CuO nanoparticle-BN hybrids composed of BN surface decorated CuO nanoparticles with low thermal conductivities was also accomplished and discussed. This report is the first of its kind in discussing the use of BN for reducing the thermal conductivities of semiconductors and is believed to be highly useful for fabricating highly efficient thermoelectric devices that are also corrosion resistant.

Experimental methods

Mass production of Zn_3P_2 nanowires was accomplished using self-catalysis in a hot-walled chemical vapor deposition (HWCVD) chamber. This procedure was extensively described in previous publications and involved the direct reaction of zinc and phosphorus. This one-dimensional growth of Zn_3P_2 crystals is aided by the presence of zinc droplets at the tips of the crystals. For the vapor phase transport of phosphorus onto zinc foils maintained at 400^{o}C, the source of red phosphors was maintained at a temperature of 480 ^{o}C. A steady flow of hydrogen aids in the vapor transport of phosphorus onto zinc foils. Following the synthesis, the nanowires were simply brushed off the zinc foils and collected.[127] Synthesis of BN decorated nanowires involved one extra experimental step following the synthesis of nanowires and preceding the brushing off nanowires from foils. This step involved exposing the nanowires to decomposed B-tribromoborazine supplied via the vapor phase onto the nanowires.[288] Care was taken to ensure that the amount of B-tribromoborazine source employed was low enough to prevent complete conformal coatings of the nanowires with BN. The morphology, phase, and chemical composition of the nanowires were respectively determined using scanning electron microscopy (SEM), X-ray diffractometry (XRD) and Raman spectroscopy.

Consolidation of the nanowires into ½ inch diameter, 1 mm thick pellets was accomplished using hot uniaxial pressing. The experimentation for this involved pressing the nanowire powders at a pressure of 300 MPa and a temperature of 500 ^{o}C hours for 2 hours under a current of nitrogen. Custom-built stainless steel dies lined with graphite were employed for this purpose. A carver hydraulic press was employed for consolidating nanowires into pellets. Following the pressing, the die was naturally cooled and the nanowire-pellet was hand polished using 1200 grit sand paper, followed by cleaning them using isopropyl alcohol.

Thermal conductivity of the pellets was calculated using the following relationship: $\kappa = \alpha \rho c_p$. Here, α is the thermal diffusivity (2% error), ρ is the density and c_p is the heat capacity (3.5%) of the sample. The density (ρ) was measured using the Archimedes principle. α was measured using the laser flash method and c_p was obtained via identical flash experiments. copper served as the reference in ideal flash experiments. A TA instruments DLF 1200 laser flash apparatus was employed for α and c_p measurement. The respective errors in the determination of α and c_p are 2% and 3.5%.

For comparison, composites were also fabricated by hot uniaxial pressing powders obtained by mixing measured quantities of commercially-available BN micropowder and

Zn_3P_2 nanowires. The thermal conductivities of the composites were then compared against hybrids obtained by consolidating BN surface decorated nanowires.

Results and discussion

Micrograph of Zn_3P_2 nanowires obtained by self-catalysis is depicted in Figure 36(a). Micrograph of the same Zn_3P_2 nanowires after the non-conformal decoration of their surfaces with BN is presented in Figure 36(b). In both the cases, the nanowires had an average diameter of 30 nm and an average length of 25 μm. In other words, decoration of nanowire surfaces non-conformally with BN, as expected, did not majorly alter their diameters. XRD analysis of the nanowires both before and after BN surface decoration (Figure 36(c)) clearly confirmed that they are primarily composed of α-Zn_3P_2 phase. Owing to the presence of BN in extremely small amounts on the surfaces of the nanowire, its presence could not be detected using XRD analysis. Although TEM analysis was not performed, based on multiple previous studies published by our group it could be reasonably assumed that the axial direction of the nanowires is along the [110] direction.[131, 271, 288]

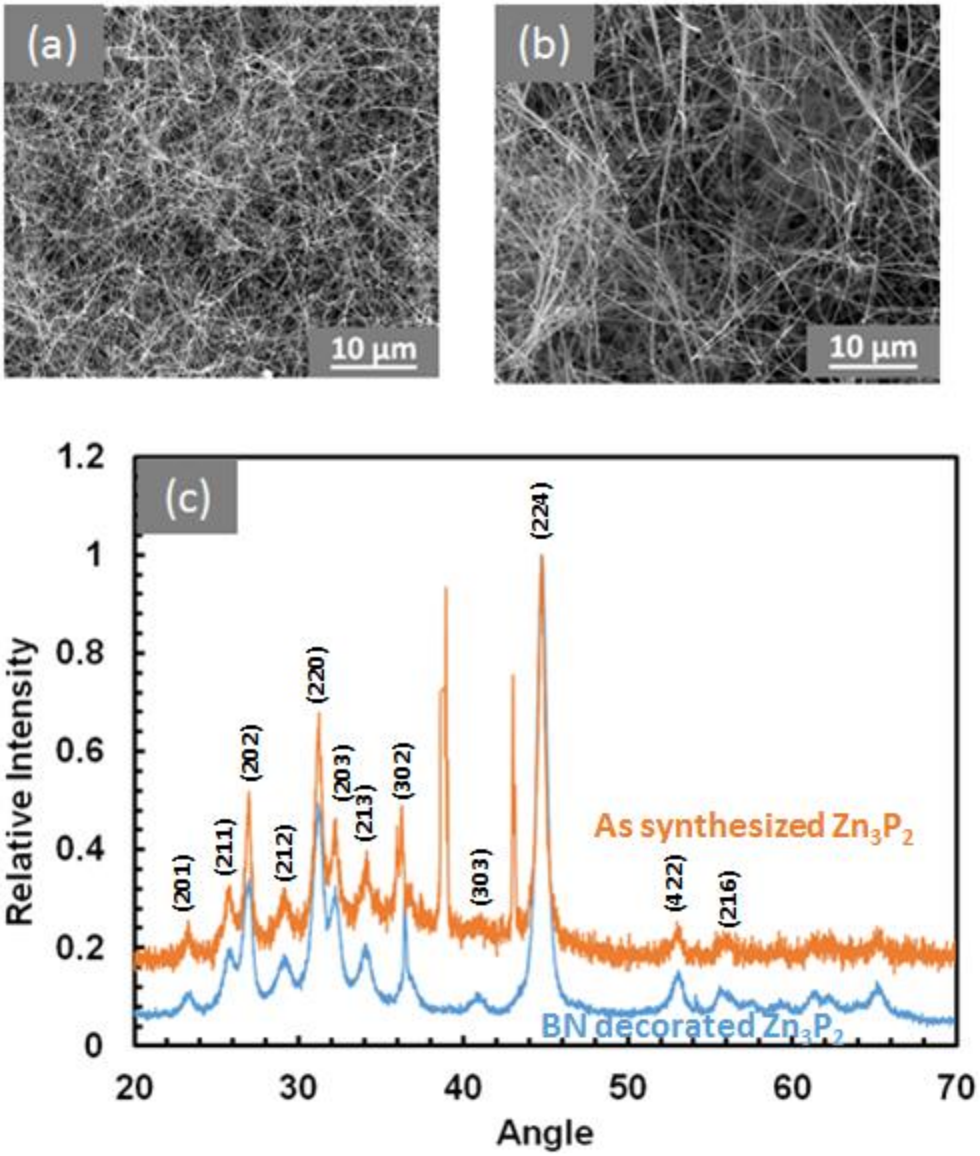

Figure 36 SEM images of (a) unfunctionalized Zn_3P_2 nanowires and (b) BN decorated Zn_3P_2 nanowires. No changes in morphologies or dimensions were observed in the nanowires. (c) XRD spectra of both pristine and BN decorated nanowires show the presence of the same phases.

A plot showing the temperature variation of the thermal conductivities of the Zn_3P_2 nanowire assemblies, Zn_3P_2 nanowire-BN composites and Zn_3P_2 nanowire-BN hybrids is presented in Figure 37. The plot indicates that the thermal conductivity of nanowires is low, ranging from 1.062 $Wm^{-1}K^{-1}$ at 300 K to 0.962 $Wm^{-1}K^{-1}$ at 620 K. Zn_3P_2 nanowire-BN composites prepared by consolidating mixtures of Zn_3P_2 nanowires and BN micropowder (1 wt.% BN) exhibited thermal conductivities lower than those observed in Zn_3P_2 nanowire pellet. The thermal conductivity of the composites ranged from 0.906 $Wm^{-1}K^{-1}$ at 300 K to 0.880 $Wm^{-1}K^{-1}$ at 620 K. This translated to a reduction of 8-15% in the thermal conductivities of Zn_3P_2 nanowires when mixed with BN micropowder. Upon increasing the weight percent of BN in the composites to 10%, no major changes in the their thermal conductivities was observed. However, a higher reduction in the thermal conductivities of Zn_3P_2 nanowires was observed when their surfaces are decorated with BN. On decoration of the nanowires with BN for the formation of Zn_3P_2 nanowire-BN hybrids the thermal conductivity of the nanowires was found to be reduced by 36 - 47%. The thermal conductivity of the hybrids ranged from 0.624 $Wm^{-1}K^{-1}$ at 300 K to 0.576 $Wm^{-1}K^{-1}$ at 620 K. Overall, all the sample studied exhibited a slight decrease in their thermal conductivities with increased temperature. Furthermore, the reduction in thermal conductivity observed on BN decoration of Zn_3P_2 nanowires is higher than that realized by merely mixing them with BN micropowders or functionalizing their surfaces with 1,4-Benzenedithiol.[131]

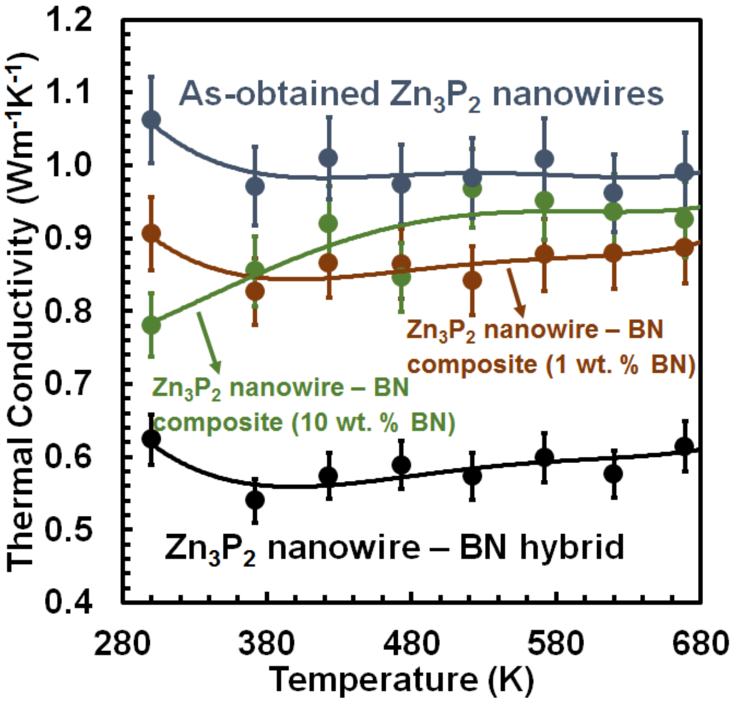

Figure 37 A plot indicating the temperature variation of the thermal conductivities of the Zn_3P_2 nanowires, Zn_3P_2 nanowire-BN composites and Zn_3P_2 nanowire-BN hybrids. The hybrids exhibited lowest thermal conductivities of all the samples tested.

To understand the thermal conductivity reduction of Zn_3P_2 nanowires on either the addition of BN micropowder or the decoration of their surfaces non-conformally with BN, it is essential to regard the Zn_3P_2 nanowires the matrix and the BN micropowder/nanodomains the filler. In composites made by mixing Zn_3P_2 nanowires and BN microparticles/nanodomains, the thermal conductivity behavior could typically be explained using traditional theories, such as Lewis-Nielsen model.[289] Here, the thermal conductivity of the composites is dependent on the ratio of the thermal conductivities of the filler to that of the matrix, λ. If $\lambda > 1$, then the thermal conductivity of the composite will be higher than that of the matrix; and if $\lambda < 1$, then the thermal conductivity of the composite will be lower than that of the matrix. In the current case, it is well-known that the filler (BN) is a superior thermal conductor, relative to the Zn_3P_2 nanowires. Considering a room temperature thermal conductivity of 450 $Wm^{-1}K^{-1}$ for BN and 1.23 $Wm^{-1}K^{-1}$ for Zn_3P_2 nanowires, the value of λ is 365.85. Therefore, the thermal conductivity of the Zn_3P_2 nanowires-BN composites are expected to be higher than those observed in stand-alone Zn_3P_2 nanowires. This stands in contrast to the measured thermal conductivity values.

Enhanced interfacial phonon scattering, and the ensuing lowering of the thermal conductivities, explains the observed behavior in the Zn_3P_2 nanowire-BN hybrid pellet compared and the Zn_3P_2 nanowire-BN composite pellet relative to that observed in Zn_3P_2 nanowire pellets. If $\kappa_{nanowires}$ is the thermal conductivity of Zn_3P_2 nanowire pellet, then it encompasses the thermal resistance contribution of the material (i.e., Zn_3P_2), the contribution to thermal resistance owed to the phonon confinement in the nanowires and finally the contribution to thermal resistance owed to phonon scattering at the nanowire–nanowire interfaces. The thermal conductivity of the Zn_3P_2 nanowire–BN micropowder composites, $\kappa_{BN\text{-}Composite}$, consists in addition thermal resistance contribution of the consolidated BN micropowder (κ_{BN}) and the thermal resistance contribution from the Zn_3P_2 nanowire-BN microparticle interfaces ($\kappa_{BN\text{-}microinterface}$), as described below in Equation 1 . Similarly, the thermal conductivity of the Zn_3P_2 nanowire–BN hybrid, $\kappa_{BN\text{-}Hybrid}$, has thermal resistance contributions from the nanowire component ($\kappa_{nanowires}$), nanocrystalline BN (κ_{BN}) and Zn_3P_2 nanowire–nanocrystalline BN interfaces ($\kappa_{BN\text{-}nanointerface}$), as described below in equation 2.

$$\frac{1}{\kappa_{BN-composite}} = \frac{1}{\kappa_{nanowires}} + \frac{1}{\kappa_{BN}} + \frac{1}{\kappa_{BN-microinterface}} \quad .....(1)$$

$$\frac{1}{\kappa_{BN-Hybrid}} = \frac{1}{\kappa_{nanowires}} + \frac{1}{\kappa_{BN}} + \frac{1}{\kappa_{BN-nanointerface}} \quad ..... (2)$$

From the data in Figure 37, it could be concluded that amount of BN does not majorly impact the overall thermal conductivities of the composites and the hybrids. This is because of the fact that increasing BN fraction in nanowires from 1 wt. % to 10 wt. % did not majorly alter the thermal conductivities of the nanowires. As the thermal conductivity of BN is very high relative to those of the nanowires and the BN interfaces, the composite and hybrid thermal conductivities are primarily dictated by the nanowire component and the BN-nanowire interfaces. In other words, it could be assumed that $\frac{1}{\kappa_{BN}} \approx 0$ in equations 1 and 2. Therefore, equations 1 and 2 could be rewritten respectively rewritten as equations 3 and 4, represented below.

$$\frac{1}{\kappa_{BN-composite}} = \frac{1}{\kappa_{nanowires}} + \frac{1}{\kappa_{BN-microinterface}} \quad .....(3)$$

$$\frac{1}{\kappa_{BN-Hybrid}} = \frac{1}{\kappa_{nanowires}} + \frac{1}{\kappa_{BN-nanointerface}} \quad .....(4)$$

Using equation 3 and 4, and the data from Figure 37, the thermal conductivities of the microinterfaces and nanointerfaces between BN and the nanowires, $\kappa_{BN\text{-}microinterface}$ and $\kappa_{BN\text{-}nanointerface}$, could be determined. The plot in Figure 38 shows the variation of $\kappa_{BN\text{-}microinterface}$ and $\kappa_{BN\text{-}nanointerface}$, with temperature. It can be clearly seen that microinterfaces between BN and the nanowires serve as better pathways for thermal transport compared to nanointerfaces between BN and nanowires. Assuming that the weight fraction of BN in both the hybrids and the composites is the same, microparticles have at least three orders of magnitude lower surface area per unit volume relative to the nanodomains. The lower surface area of the microparticles lowers the magnitude of phonon scattering. Therefore, the microinterfaces are expected to exhibit higher thermal conductivities, than the nanointerfaces. Secondly, the process of formation of Zn_3P_2 nanowire-BN hybrids results in the spatially uniform decoration of Zn_3P_2 nanowires with BN. CVD processes are expected to lead to such spatially uniform BN coatings on nanowire surfaces. In sharp contrast, mere mixing of BN microparticles and Zn_3P_2 nanowires used for the formation of composites lead to spatially non-uniform composites. Overall, the amount of Zn_3P_2-BN interfaces available for phonon scattering is higher in the hybrids than in the composites. This also makes the microinterfaces better thermal conductors than the nanointerfaces. Making interfaces better thermal conductors necessitates that the interfaces between the nanowires and the BN be defect-free. Heteroepitaxial deposition of a thermal conductor on a thermal insulator could be theoretically employed for ensuring that the interfaces are defect-free and that the resulting hybrids exhibit enhanced thermal conductivity. In the current case, although CVD was employed for the formation of the hybrids, the large lattice mismatch between BN and Zn_3P_2 make the nanointerfaces imperfect and hence poor thermal conductors. The lattice parameters and their mismatches are shown in Table 3

Table 3 Table showing the differences in lattice parameters among zinc phosphide, copper oxide and three different structures of boron nitride[290-294]

Material	a (A)	b (A)	c (A)	aplha	beta	Gamma
Zn_3P_2	8.097	8.097	11.45	90	90	90
Cu_2O	4.627	4.627	4.627	90	90	90
h-Bn	2.504	2.504	6.6612	90	90	120
Wurtzite BN	2.55	2.55	4.23	90	90	120
zinc blende structure BN	3.6157	3.6157	3.6157	90	90	90

In short, mere mixing of BN and compound semiconductor nanowires (directly in the solid state) may not be a feasible route for enhancing the thermal conductivities of the resulting composites, even when the consolidation of such mixtures is performed at elevated temperatures. Therefore, any annealing of defects at the nanowire-BN interface is not sufficient to enhance thermal transport through them. Interface-engineered assembly is essential both for enhancing and reducing thermal transport through nanomaterial assemblies and their composites. For example, welding of nanowires during their assembly can be used to enhance thermal transport between them.[205] In such cases, phonon confinement resulting from reducing the size of the welds could also be employed to curtail thermal transport between them.[205]

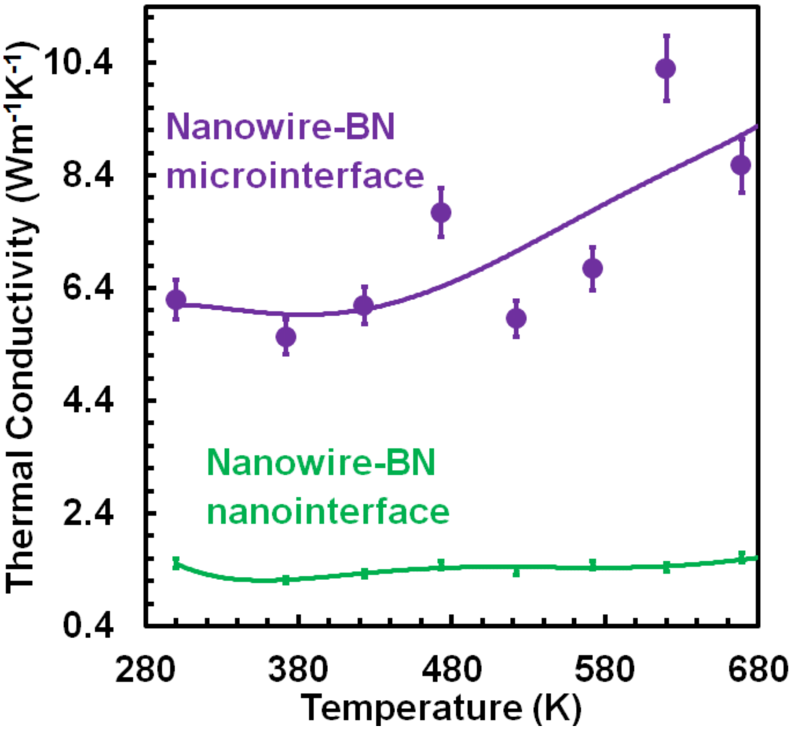

Figure 38 A plot indicating the temperature variation of the thermal conductivities of the microinterfaces between Zn_3P_2 nanowire and BN microparticles in composites, and nanointerfaces between Zn_3P_2 nanowire-BN nanodomains on their surfaces in the hybrids.

To ensure that the observed thermal conductivity behavior is universal and applicable to other nanomaterials systems in addition to Zn_3P_2 nanowires, thermal conductivity behavior of CuO micropowders, CuO micropowder-BN composites and CuO micropowder-BN hybrids were also measured and presented in Figure 39. As expected, the thermal conductivities of the samples exhibited the following trend: $\kappa_{CuO\ micropowders} > \kappa_{CuO\ micropowder\text{-}BN\ composites} > \kappa_{CuO\ micropowder\text{-}BN\ hybrids}$.

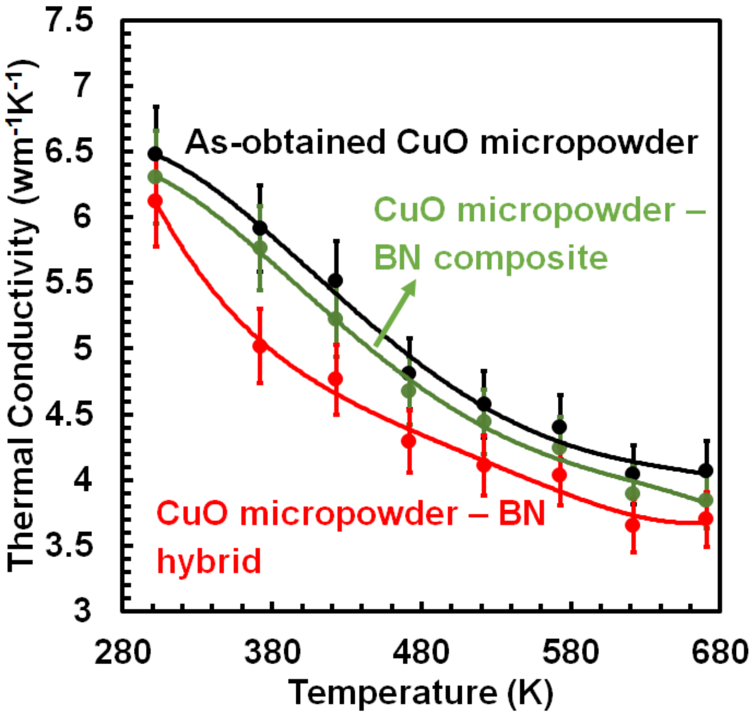

Figure 39 A plot indicating the temperature variation of the thermal conductivities of the CuO micropowder, CuO micropowder-BN composites and CuO micropowder-BN hybrids. Similar to the case of Zn3P2 nanowires, the hybrids exhibited lowest thermal conductivities

Conclusions

In summary, thermal conductivity behavior of composites and hybrids of BN and semiconducting nanowires/nanoparticles have been studied. It was observed that mere addition of superior thermal conducting filler to a semiconducting matrix does not improve the overall thermal conductivity of the resulting composites or hybrids, especially if the mixing is performed in the solid state. Contrary to the expectation, addition of filler in nanostructured form to a semiconducting matrix actually results in composites and hybrids that have thermal conductivities lower than those of the individual components. In other words, rule of mixture does not help in enhancing the thermal conductivities of bulk nanostructured systems. Owing to the significant role of interfacial phonon scattering on the thermal conductivities of bulk nanostructured systems, enhancing their conductivities essentially requires controlling the chemistries and phases of the interfaces between the nanostructures in the bulk assemblies. In an ideal scenario, bridges that have the same chemical compositions and phases as the nanostructures they are joining, coupled with them being in homoepitaxy with the nanostructures, will be ideal for tuning the thermal conductivities of bulk nanostructured materials.[205]

CHAPTER VIII

THERMOELECTRIC PROPERTIES OF STABILIZED MANGANESE SILICIDE AND WELDED MAGNESIUM SILICIDE

Introduction

Thermoelectrics despite all their advantages are limited to use in niche applications and not in terrestrial applications. This is due to their low conversion efficiencies and high costs. Magnesium and higher manganese silicides, as discussed in the literature review, have great potential to be used for thermoelectrics for terrestrial applications. This is owed to fact that the constituent elements are earth abundant, cost effective and non-toxic. However, the low zT's of these materials limits their use. In addition, as discussed in the literature review section of this dissertation, nanowires are expected to have higher thermoelectric figure of merit, which in turn leads to higher efficiencies for converting heat to electricity. Experimental demonstrations using individual nanowires of silicon have shown two-order increase in thermoelectric figure of merit.[68] However, as discussed extensively in the literature review, assemblies of nanowires did not show this enhanced performance.[295] In this context, strategy for assembling magnesium silicide nanowires is explored here in order to reduce the thermal conductivity and simultaneously increase the electrical conductivity while not affecting the seebeck coefficient. In addition the assembly strategy should also be able to protect the device against mechanical degradation while temperature cycling. Strategies for obtaining such semiconductor nanowire assemblies do not currently exist. The assembly strategy used in this work, for consolidating nanocrystalline semiconductors, leads to the formation of electrically insulating oxides at the interfaces between the nanowire after consolidation (e.g., interfaces composed of electrically-insulating MgO are formed when nanocrystalline Mg_2Si is assembled) and also as shown will lead to tailoring of electrical and thermal properties to obtain higher efficiencies in the material system.

The current strategy for achieving such interfaces, involves conformal decoration of the synthesized silicon nanowires with SiO_2 nanoparticles.[205, 296] The silicon nanowires particles thus obtained are phase transformed into Mg_2Si via solid-state diffusion of magnesium through the nanowires.[125] These converted nanowire powders are then hot pressed and sintered to obtain nanowire assemblies joined by the same material as the nanowires. These pellets are characterized for their thermoelectric properties i.e. seebeck coefficient, electrical conductivity and thermal conductivity. Such an assembly without oxide interfaces are expected to lead to enhanced thermoelectric performance.

Experimental methods

Fabrication of welded Mg_2Si nanowire pellets

Interface engineered assembly of Mg_2Si nanowires i.e. Mg_2Si nanowires attached with Mg_2Si bridges were fabricated for their thermoelectric characterization. Pellets of Mg_2Si unwelded nanowires and welded nanowires in which the Mg_2Si nanowires are connected with Mg_2Si nanowire welds were fabricated. In order to fabricate these pellets (in this work both pellets and assemblies are used interchangeably) silicon nanowires were synthesized via electrochemical etching. Silcion wafers of (100) orientation were etched in a solution of 0.04 M $AgNo_3$ and 5M HF solution. Anistropic etching of silicon leads to the formation of silicon nanowires.[125] Gram quantities of Si nanowires were produced in this method. More discussion on the silicon nanowire synthesis is available in the mass production section. The silicon nanowire samples thus obtained were phase transformed into Mg_2Si via solid-state diffusion. This was achieved by scraping the nanowires of the silicon wafer and placing these nanowire powders in between two polished magnesium foils. The foils were heated to 400 °C for 2 hours in a vacuum chamber, the conditions are shown in Figure 40, with a base pressure of 5 mTorr and an operating pressure of 50 mTorr with 100 sccm hydrogen flow which provides a relatively oxygen free environment. This heating allows the magnesium to diffuse through the silicon nanowires and leads to the phase transformation of silicon nanowires into Mg_2Si nanowires. The phase transformation was conducted in a flow of hydrogen in order to prevent, or in the very least minimize, the the formation of MgO. The obtained Mg_2Si nanowires were then hot pressed at 500 MPa and 400 °C for 2 hours in a stainless steel die covered with graphite sheet in order to prevent any unwanted side reactions from the stainless steel die. This leads to highly dense Mg_2Si nanowire pellets that are 12 mm in diameter and at least 1 mm thick. The pellets were then annealed inside a vacuum chamber, in a flow of hydrogen, at 450 °C for 2 hour without any pressure inside the graphite sheet covered stainless steel die. This leads to better sintering of the nanowires. The welded nanowire assemblies of Mg_2Si nanowires were fabricated using the same procedure. However in this fabrication silica decorated silicon nanowires Figure 41 (a) were used as the starting material. The silica nanoparticles used here are functionalized with an amine group with an average diameter of 200nm. The pellets obtained were polished with 800 grit polishing paper and alcohol to obtain a clean surface for the density and thermoelectric characterization.

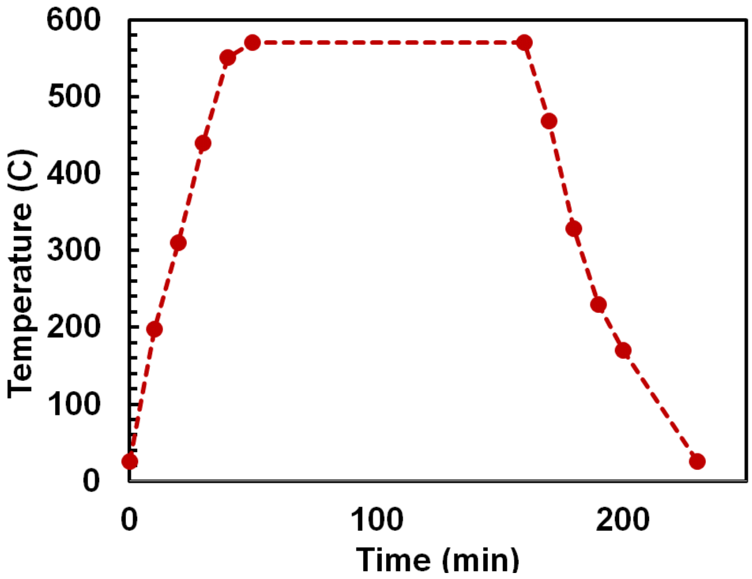

Figure 40 Temperature profile for solid state diffusion of magnesium into silicon nanowires for fabrication of magnesium silicide nanowires.

Fabrication of BN decorated $MnSi_{1.75}$ micron pellets

Stabilized and interface engineered assembly of $MnSi_{1.75}$ micron particles was accomplished via phase transformation i.e. by solid state diffusion of manganese powder into silicon micron particles. Pellets of $MnSi_{1.75}$ micron powders and $MnSi_{1.75}$ BN decorated micron powders were fabricated. In order to fabricate these pellets silicon micron powders were obtained by crushing a single crystalline wafer of silicon using a mortar and pestle. The obtained powders were ball milled in a “Cole-Parmer one-tier jar high-capacity laboratory jar mill” for 24 hours. The ball-miller powder was then mixed with 44 micron manganese powder in a mortar and grounded manually with a pestle to allow for homogenous mixing. The obtained homogenous mixture of manganese and silicon micron powders were then filled in a stainless steel die covered with a graphite sheet. The powder in the die was hot pressed at a pressure of 500 MPa and 500 $^{\circ}$C in a continuous flow of nitrogen for 2 hours. The pellets were then annealed inside a vacuum chamber, in a flow of 100 sccm hydrogen, at 700 ˚C for 2 hour without any pressure inside the graphite sheet covered stainless steel die. This leads to better sintering of the formation of $MnSi_{1.75}$ powders from a mixture of silicon and manganese powders. The BN decorated manganese silicide micron pellets were fabricated in a similar fashion. The silicon micron particles used for the phase transformation were non-conformally decorated with BN. This procedure was discussed in detail in the previous chapters V. Pellets of diameter 12 mm and at least 1 mm thick were obtained.

The pellets thus obtained were characterized via XRD and SEM to confirm the phase formed as shown in Figure 42. The thermoelectric figure of merit of these pellets was measured by measuring the individual components. The seebeck coefficients w.r.t temperature were obtained via the analogue subtraction. The electrical conductivity were measures using the same setup via the 4-probe Van-der-Pauw technique. This allows for the measurement of both the seebeck coefficient and electrical conductivity at various temperatures simultaneously. The thermal conductivity (κ) of the pellets is calculated using the following $\kappa = \alpha \rho C_{p.,}$ where ρ is the density of the pellet which is measured using Archimedes principle, C_p is the heat capacity measured using differential scanning calorimetry and α is the thermal diffusivity, measured using laser flash apparatus via a TA instruments DLF-1200.

Results and discussion

Electron micrograph of silicon nanowires obtained from electroless etching of single-crystalline silicon wafers and the silicon nanowires decorated with silica particles are shown in Figure 41 (a). These nanowires were phase transformed into Mg$_2$Si nanowires both welded. These phase transformed silica decorated nanowires are presented in Figure 41(b). Comparing the phase transformed nanowires without and with the silica nanoparticle decoration; it is evident that the welding of nanowires leads to the formation of bridges between the nanowires and leads to the formation of Mg$_2$Si nanowire assembly.

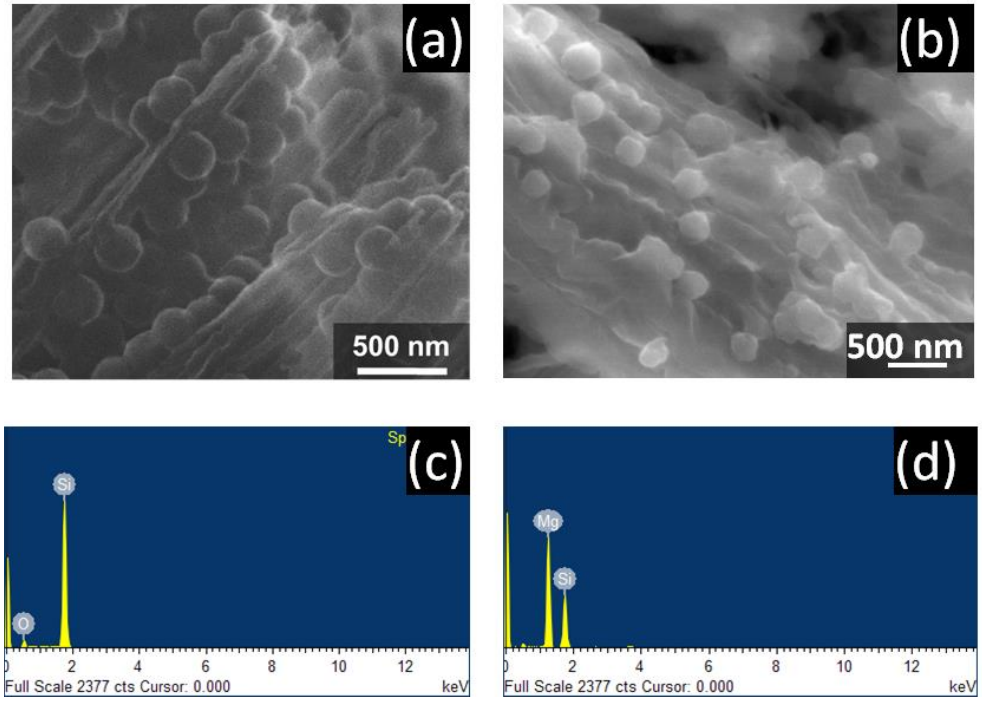

Figure 41 Scanning electron microscopy of (a) silica decorated silicon nanowires and (b) phase tranformed magnesium silicide nanopartciles decorated magnesium silicide nanowires.

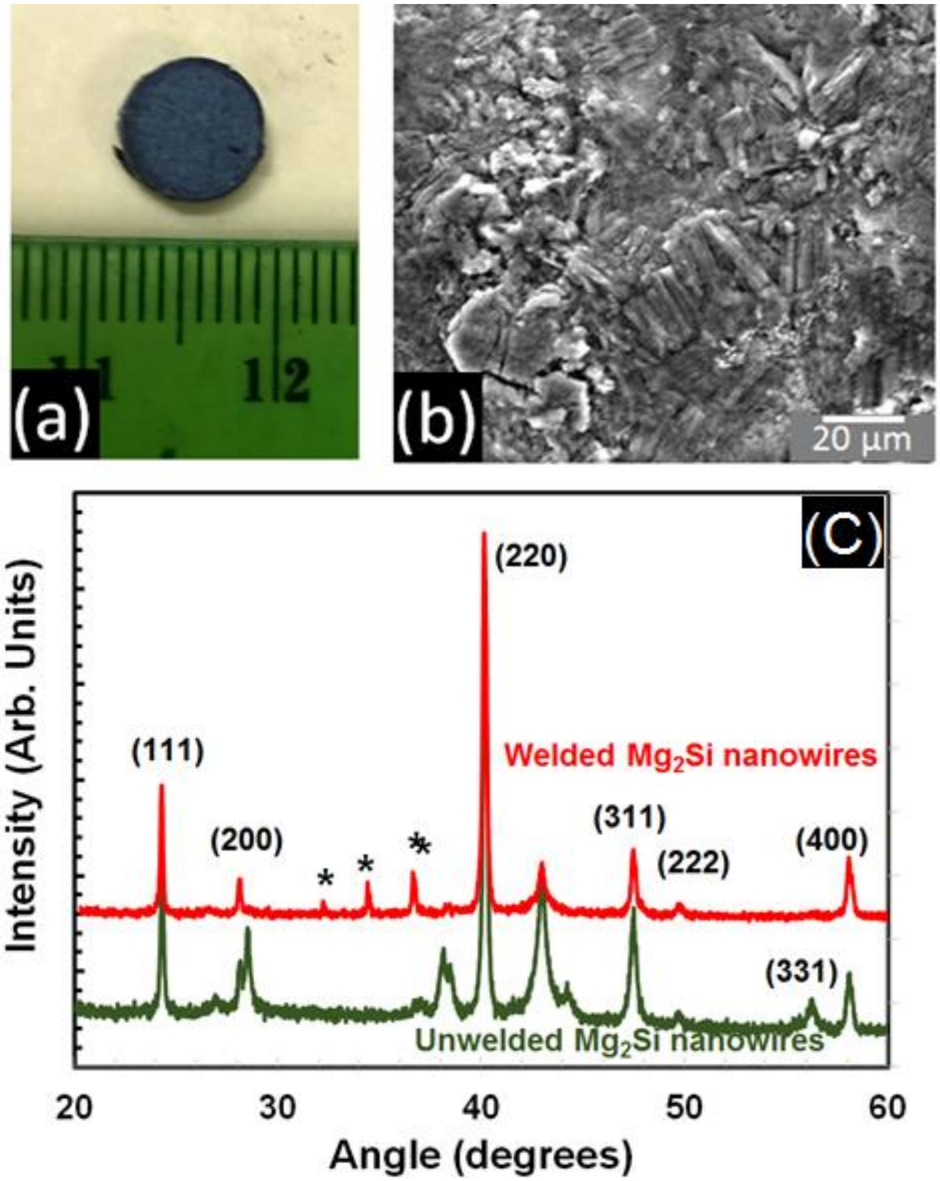

Figure 42 (a) Optical micrograph of Mg_2Si nanowire pressed pellets (b) Scanning electron micrograph of pressed nanowire pellet and (c) X-ray diffraction spectra of both welded and unwelded nanowires. The (*) represents the carbon peaks a reminant of pressing.

Post pressing of these nanowires via hot pressing and annealing results in macro pellets. SEM imaging of these pellets show the presence of nanowire morphology. XRD analysis on the pressed pellets, both welded and unwelded nanowires result in phase pure

Mg_2Si as evident from Figure 42. The density of the pellets was measured using the Archimedes principle. High relative density (greater than 98%) was observed in these pellets.

Pellets of $MnSi_{1.75}$ and BN $MnSi_{1.75}$ were also run through the same gamut of characterization techniques. The scanning electron microscopy images of silicon micron powder, Figure 43, shows that the sizes of the particles range from 5 μm to 50 μm. The X-ray diffraction spectroscopy of these pellets reveals the presence of $MnSi_{1.75}$ phase. However silicon peaks were also detected in these pellets.

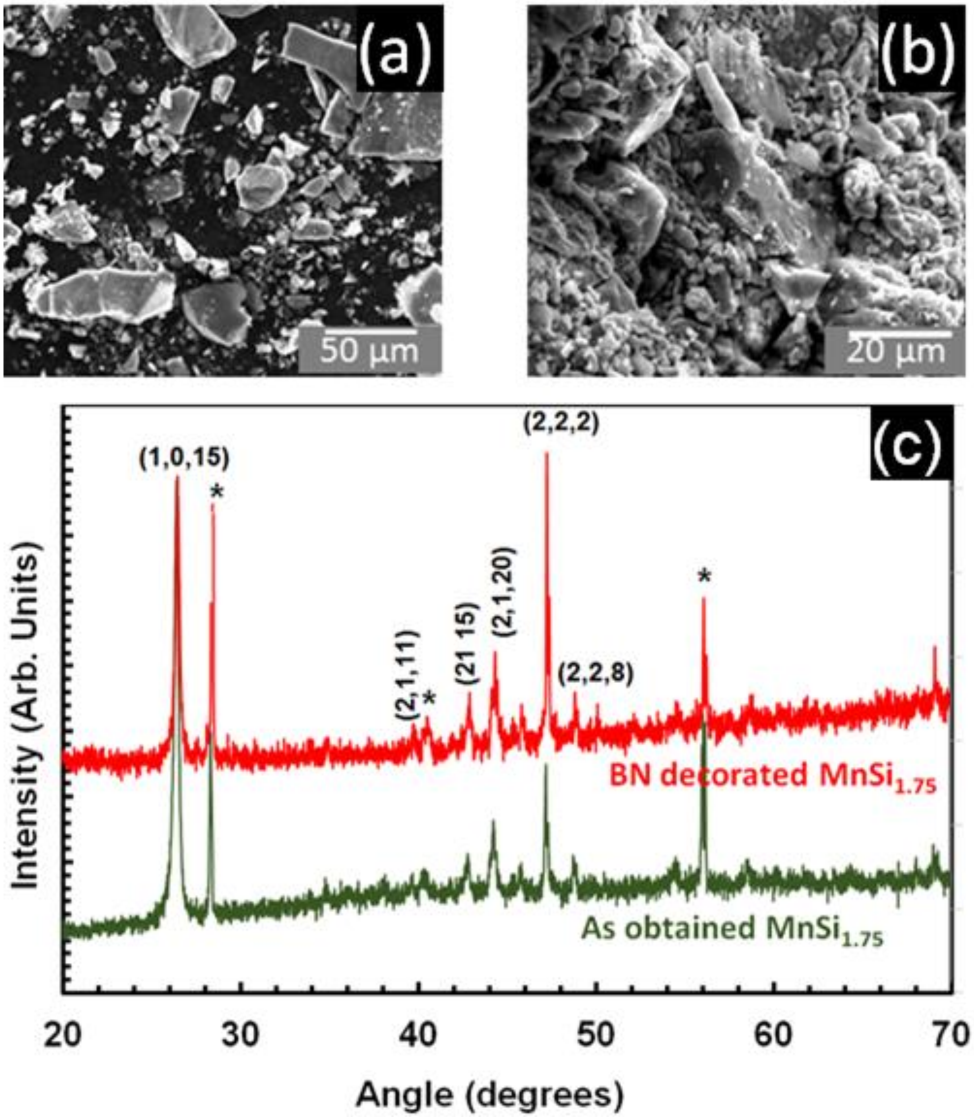

Figure 43 Scanning microscopy of (a) crushed and ball-milled silicon micron powder and (b) phase transformed manganese silicide micron powders. The X-ray-diffraction spectroscopy of converted manganese silicide and BN decorated show the higher manganese silicide phase. In addition, some peaks of silicon are also observed in both the pellets. The (*) indicates silicon peaks which indicate incomplete transformation of silicon micron particles to HMS.

Thermoelectric characterization

Welded and unwelded nanowire networks

The pellets were characterized for thermoelectric properties. These properties are shown in Figure 44**.** Seebeck coefficient was measured using the analogue subtraction method. Magnesium silicide is an n-type material. However the measured seebeck coefficient of the nanowires showed a positive seebeck. This is believed to be due to the silver doping resulting from incomplete removal of silver, which is shown to be a p-type dopant for Mg_2Si. The seebeck coefficient of both welded and unwelded nanowire networks are similar in magnitude. A seebeck coefficient of approximately 500 μV/K was measured at 773K. [41]

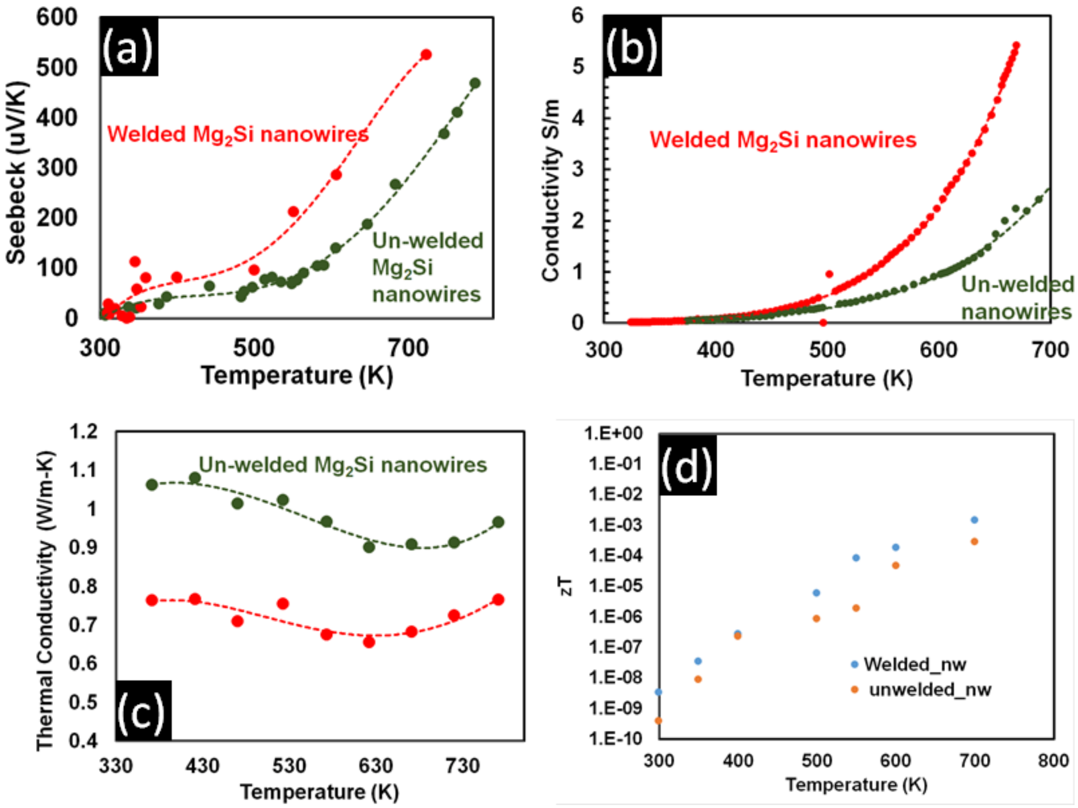

Figure 44 Thermoelectric properties of welded and unwelded magnesium silicide nanowire networks a) seebeck vs temperature b) conductivity vs temperature c) thermal conductivity w.r.t. temperature and d) the thermoelectric figure of merit with respect to temperature

The electrical conductivity of welded nanowire networks was twice that of the unwelded nanowire networks. The increased thermal conductivity of the welded nanowire is due to the formation of Mg_2Si bridges across the nanowire networks. The thermal conductivity of these pellets was measured using the laser flash analysis.

Thermal conductivity of the welded and unwelded nanowire networks are plotted in Figure 44 (c). Though the electrical conductivity of the welded nanowire pellet is greater than that of the unwelded pellet, the thermal conductivity of the welded pellet is lower than the unwelded nanowire pellet. This is due to the single crystalline Mg_2Si bridges between the Mg_2Si nanowires. The bridges act as highway for electron transfer due to the single crystalline nature of the junctions. However the same bridges/welds obstruct the flow of phonons. The electrons have smaller mean free paths than that of phonons allowing them to pass through the welds while the phonons with larger mean free path are scattered by the welds. The thermoelectric figure of merit was calculated from the zT formula $zT = \frac{S^2\sigma T}{\kappa}$.

In short, the welded nanowire pellets have similar seebeck coefficients as the unwelded nanowire pellets, but the welded nanowire pellets have higher electrical conductivity and lower thermal conductivity than the unwelded nanowire pellets. Therefore the welded nanowire pellets have higher thermoelectric figure of merit compared to the unwelded nanowire pellets as show in Figure 44 (d).

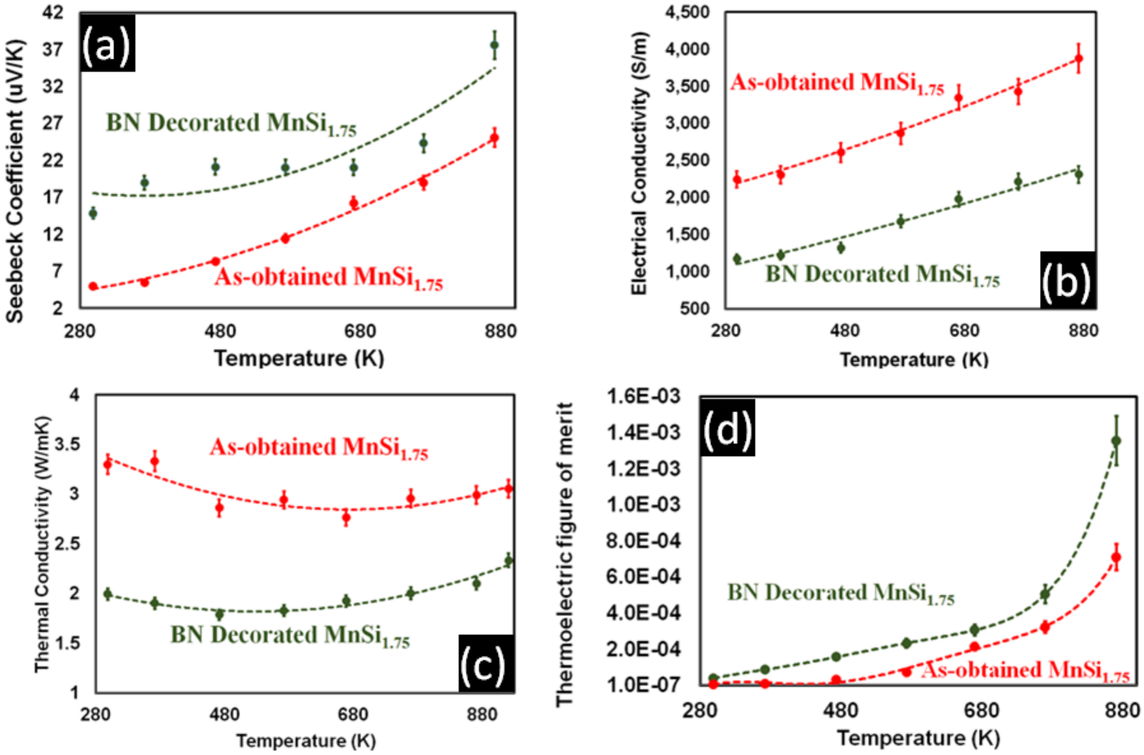

Figure 45 Thermoelectric characterization of $MnSi_{1.75}$ and $BN\_MnSi_{1.75}$ a) seebeck vs temperature b) conductivity vs temperature c) thermal conductivity w.r.t. temperature and d) the thermoelectric figure of merit with respect to temperature

Thermoelectric properties of BN decorated $MnSi_{1.75}$ *micron pellets*

The pellets of higher magnesium silicide were characterized for their thermoelectric properties by individually measuring their seebeck coefficient, electrical conductivity and thermal conductivity. The seebeck coefficient w.r.t. temperature was measure via the analogue subtraction method. The seebeck coefficient of both the pellets i.e. higher manganese silicide (HMS) micron powder pellet and the BN decorated higher manganese silicide micron powder pellet was observed to be positive which is expected of these materials. A peak seebeck coefficient of 25 µV/K was measured for the HMS sample and a peak of 38 µV/K was observed for the BN decorated sample, at 870K. Similarly, the electrical conductivity of these samples were measure to be approximately 3900 S/m and 2300 S/m respectively at 870K. The decreased electrical conductivity of the BN samples is believed to be the reason for the increased seebeck coefficients for these samples. The thermal conductivity of BN decorated samples was found to be 2.33 W/mK compared to the 3.05 W/mK for the undecorated HMS samples. This decrease in thermal conductivity is in line with the previously observed trend in BN decorated samples i.e. BN decorated Zn_3P_2 and CuO have shown lower thermal conductivities than the undecorated pristine samples. The decrease in thermal conductivity is attributed to the increased scattering of phonons caused by the BN decoration in these samples.

The thermoelectric figure of merit (zT), when calculated for the two samples, the BN decorated samples exhibited higher thermoelectric figure of merit compared to the undecorated pristine samples. The decrease in electrical conductivity in BN samples was compensated with the increased seebeck coefficient and decreased thermal conductivity. From Figure 45 (d) it can be observed that the BN decorated samples exhibited two time the figure of merit compare to the undecorated pristine samples.

Conclusion

The work presented in this chapter focused on welding of nanowires and BN decoration as techniques for increasing thermoelectric figure of merit. Nanowires of magnesium silicide were welded to form nanowire assemblies. The welded nanowire networks, compared to their unwelded counterparts, showed an increased electrical conductivity and decreased thermal conductivity, without affecting the seebeck coefficient, there resulting in an increased zT. This is a result of single crystalline welds between the nanowires which allow for the free flow of electrons and scatter the phonons, which have a higher mean free path than the electrons.

Similarly, the BN decorated $MnS_{1.75}$ micron pellets exhibited a higher thermoelectric figure of merit, twice that of the undecorated pristine $MnS_{1.75}$ micron pellets. The BN decorated samples displayed lower thermal and electrical conductivities compared to undecorated samples which lead to the higher zT.

CHAPTER IX

CONCLUSIONS

A pathway for assembling nanowires into bulk devices is essential for the following reasons:

1. To verify and translate the thermoelectric performances reported in individual nanowires to macrodevices based on large-scale nanowire assemblies.
2. Ensure that enhanced thermoelectric performances demonstrated in individual nanowires are possibly further enhanced in these large-scale nanowires assemblies.

Accomplishing such a task requires that nanowires should not only be mass produced, but also assembled in an interface-engineered manner. Furthermore, the nanowires and their assemblies should be stable against degradation at both ambient and elevated temperatures. Building on the work performed in our research group in the past,[125, 126] this work contributed the following towards the aforementioned goals:

1. An assembly technique for consolidating mechanically rigid nanowires into highly dense pellet without the loss of the nanowire morphology in the process. While consolidation of flexible nanowires was achieved in the previous work done by Dr. Brockway in our lab,[131] this work dealt with the simultaneous alignment and consolidation of mechanically rigid nanowires for obtaining highly dense pellets. This is crucial because currently no strategy allows for measuring thermoelectric properties of nanowires in a direction perpendicular

to their lengths. ECAE of silicon nanowires obtained by electroless etching was employed for this purpose. Since this is a room temperature process, there were no major changes to the dimension of the nanowires. This is unlike traditional hot pressing techniques where consolidation of powders leads to grain growth via sintering and alteration of the dimensions of the particles composing the powders. In addition to consolidation, nanowire alignment is also observed in a few regions of the pellets. Based on the results, it was understood that the interlocking of rough surfaces of the nanowires is responsible for the mechanical integrity of the nanowire pellets. Optimization of the ECAE processing conditions further is expected to lead to complete alignment of the nanowires within the pellets.

2. Nanowires composed of earth abundant elements (Zn_3P_2, Mg_2Si and ZnO), were stabilized via non-conformal decoration of their surfaces with BN. In this work, nanowires of Zn_3P_2, ZnO and Mg_2Si were stabilized without majorly impacting their electrical and electronic properties. Zn_3P_2 and ZnO nanowires were exposed to a vapor of tribromoborazine for this purpose. However, BN decorated Mg_2Si nanowires were obtained by decorating silicon nanowires with BN, followed by phase transforming these nanowires into Mg_2Si via solid-state diffusion of magnesium. The morphology and phase of these nanowires were preserved when exposed to water or acid solutions of pH 3. The stabilization of these materials is attributed to the change of the wetting properties of the nanomaterial. Addition of BN on to the nanowires makes their

surfaces non-wettable to aqueous acidic solution, thereby preventing the reaction between the nanomaterial and the acidic solutions.

3. BN decoration of nanowires for stabilizing them also lead to the reduction in thermal conductivity, as expected, without any adverse impact on their electrical and electronic properties. In this part of the study, the nanomaterials were conformally decorated with BN and then these materials were pressed to fabricate pellets for measuring the thermal conductivity. Here, Zn_3P_2 nanowires and CuO micron particles were used as model systems. The thermal conductivity behavior of these samples were compared to those of composites (i.e., mixtures of Zn_3P_2 nanowires and BN micron powder), and pellets made from as-obtained nanowires. It was observed that mere addition of superior thermal conducting filler, BN in this case, to a semiconducting matrix does not improve the overall thermal conductivity of the resulting composites or hybrids, especially if the mixing is performed in the solid state. Contrary to the expectation, addition of filler in nanostructured form to a semiconducting matrix actually results in composites and hybrids that have thermal conductivities lower than those of the individual components. Moreover, addition of filler materials in nanoscale or molecular-scale form allows for lowering the thermal conductivity of nanowire matrices to a maximum, as opposed to adding filler in micron-scale form.
4. Finally, in this work, the assembly and stabilization strategies were utilized to fabricate pellets of BN decorated $MnSi_{1.75}$ micron particles and welded Mg_2Si

nanowire networks to ascertain their thermoelectric performances. An increase in zT was observed in both the scenarios i.e., upon BN decoration or welding of the nanowires in the assemblies or both. However, the zT values realized were very low, much lower than those reported in the literature. The reasons behind these lower zT values and commentary about the future outlook of nanowire-based thermoelectrics are discussed in the next chapter.

CHAPTER X

FUTURE WORK

Strategies for stabilizing and assembling mass produced nanowires have been discussed. The two strategies for improving zT of nanowire forms of materials are; the decoration of nanowire surfaces with BN and nanowire welding during their interface engineered assembly, have proven useful. However, the achieved zT values in these materials have been lower, making them unsuitable for use in the current form in commercial markets. The following describes some of the reasons identified for lower thermoelectric performances obtained in this study. However, it needs to be emphasized that addressing these drawbacks will lead to commercially-viable, nanowire-based thermoelectrics.

Routine materials characterization using XRD and SEM may not be enough to precisely determine the chemical composition of materials and correlating them to their thermoelectric performances. In fact, this may be the reason behind widely varying zT values reported by various research groups for the same material.[38, 40, 43, 46, 112-114, 116, 117, 122-124, 297] For example, most of the Mg_2Si nanomaterials systems may be covered with thin layers of MgO. The ratio of the amounts of MgO to Mg_2Si in the samples depends not only on the methods employed to synthesize the samples, but also on the materials' morphology. Consequently, Mg_2Si nanomaterials have relatively more MgO than bulk Mg_2Si crystals of the same mass. Unless this quantification is reported in studies, it is not possible to accurately compare the thermoelectric performances reported by various research groups. Another example of the shortcoming of routine materials characterization is their inability to detect silver contamination of nanowires obtained by electroless etching (detailed in the section below). This silver contamination was not even detectable by TEM. The sensitivity of these instruments is upwards of 1 wt. %, whereas doping of Mg_2Si with impurities on the order of 0.1 wt. % or less are sufficient to dramatically alter the thermoelectric properties of the material.

As mentioned above, the use of silver nitrate for electroless etching of silicon wafers to obtain silicon nanowires leaves behind a small quantity of silver. Multiple studies incorrectly assume that performing etching at room temperature prevents their contamination.[102, 125] This work indicated that silver cannot be completely removed from nanowires, following their synthesis by using electroless etching. As this silver cannot be detected using routine SEM, XRD or TEM characterization of nanowires, it is incorrectly assumed that no silver contamination of the nanowire occurs. In this work, such an assumption was made initially. No silver was detected in our nanowires in the initial stages. However, shear forces employed via ECAE to align and consolidate nanowires disturbed the nanowire surfaces and thereby made the silver embedded within their surfaces visible, which was not hitherto visible. Such a contamination leads to the unexpected doping of the silicon, thereby compromising the thermoelectric properties of silicide nanowire networks. This is possibly one of the reasons for the poor performances of the silicide nanowire networks. Additional proof of silver contamination is in the thermoelectric performances of Mg_2Si measured in this work. Mg_2Si is inherently an n-type semiconductor, however a p-type behavior was observed in this work. Silver is shown to dope Mg_2Si p-type and this silver is a by-product of the electroless etching.[122] Due to the inability of acids to diffuse into voids between the nanowires, silver is left unreacted despite immersing the etched silicon wafers in boiling concentrated acids for extended periods of time (i.e. > 8 hours). Therefore, shearing nanowires surfaces using a technique such as rolling, before cleaning them with boiling acids, is necessary to completely remove the silver embedded within the surfaces of the nanowires.

Routine XRD and EDS characterization is also insufficient to determine whether the phase transformation of silicon into Mg_2Si is complete. The pellets of magnesium silicide were characterized via XRD and EDAX to confirm their phase, which revealed the presence of pure Mg_2Si phase only. However these techniques are bulk level characterization techniques, i.e. they do not reveal the true composition of the materials, especially at nanoscale, and therefore the conversion might not be complete at the nanoscale. The evidence of a complete phase transformation can only be obtained by utilizing destructive techniques, such as immersing the silicides obtained in concentrated hydrochloric acid and then characterizing the remaining powder. Mg_2Si reacts with hydrochloric acid to form magnesium chloride and silane. However, silicon is stable in such solutions and therefore absence of silicon in the acid treated Mg_2Si would act as evidence of complete phase transformation.

This work demonstrated that both BN decoration of nanowires and assembly of nanowires via welding implemented individually improved the zT of nanowire assemblies. However, a combined approach using both these techniques can lead to the development of higher zT materials and optimizing their thermoelectric performances. In addition, optimal doping of nanowire assemblies by intentionally adding known quantities of impurities is essential to optimize the thermoelectric performances of Mg_2Si nanowire assemblies. The performance of thermoelectric materials, among many factors, depends on the carrier concentration of the material. Optimization of the dopants, which in turn leads to optimization of carrier concentration, has been the focus of many works. Therefore, a logical extension of this strategy in addition to the above mentioned and proven strategies has a greater chance of improving the thermoelectric figure of merit, thereby enhancing the efficiency of the thermoelectric devices.

In this work, welding of nanowires was accomplished by phase transforming SiO_2 decorating silicon nanowires for obtaining Mg_2Si nanowires with Mg_2Si bridges by solid state diffusion of magnesium. This strategy has increased the electrical conductivity and reduced the thermal conductivity. Use of elements such as Sn or Ge for decoration of silicon nanowires will lead to the formation of Mg_2Si-Mg_2Sn hybrids, known to exhibit high zT values.[38, 111, 112] As tin and germanium are isoelectronic dopants to silicon, therefore no deleterious effects are expected due to their presence.

REFERENCES

1. *Annual Energy Review 2011*; Lawrence Livermore National Laboratory and U.S. Department of Energy, DOE/EIA 03842011.
2. Parida, B.; Iniyan, S.; Goic, R., A review of solar photovoltaic technologies. *Renewable and sustainable energy reviews* **2011,** *15*, 1625-1636.
3. El Chaar, L.; lamont, L. A.; El Zein, N., Review of photovoltaic technologies. *Renewable and Sustainable Energy Reviews* **2011,** *15*, 2165-2175.
4. Fradkin, G. M.; Kodyukov, V. M., Radioisotope thermoelectric generators. *At Energy* **1969,** *26*, 193-198.
5. Rowe, D. M., *CRC handbook of thermoelectrics*. CRC press1995.
6. Seebeck, T. J., Ueber die magnetische Polarisation der Metalle und Erze durch Temperatur-Differenz. *Annalen der Physik* **1826,** *82*, 133-160.
7. Snyder, G. J.; Toberer, E. S., Complex thermoelectric materials. *Nat. Mater.* **2008,** *7*, 105-114.
8. Slack, G., New Materials and Performance Limits for Thermoelectric Cooling. In *CRC Handbook of Thermoelectrics*, CRC Press1995; Vol. null.
9. Wu, Y.; Finefrock, S. W.; Yang, H., Nanostructured thermoelectric: Opportunities and challenges. *Nano Energy* **2012,** *1*, 651-653.
10. Schock, A. *RTGs Options for Pluto Fast Flyby Mission*; Fairchild Space and Defense Corporation; International Astronautical Federation1993.
11. Dresselhaus, M. S. In *Careers in thermoelectricity*, Proceedings of the XVII International Conference onThermoelectrics, 24-28 May 1998; pp 29-32.

12. Yang, J.; Stabler, F. R., Automotive applications of thermoelectric materials. *Journal of Electronic Materials* **2009,** *38*, 1245-1251.

13. Miller, E. W.; Hendricks, T. J.; Peterson, R. B., Modeling energy recovery using thermoelectric conversion integrated with an organic Rankine bottoming cycle. *Journal of Electronic Materials* **2009,** *38*, 1206-1213.

14. Riffat, S. B.; Ma, X., Thermoelectrics: a review of present and potential applications. *Applied Thermal Engineering* **2003,** *23*, 913-935.

15. Hsiao, Y.; Chang, W.; Chen, S., A mathematic model of thermoelectric module with applications on waste heat recovery from automobile engine. *Energy* **2010,** *35*, 1447-1454.

16. Xie, M.; Gruen, D. M., Potential Impact of ZT = 4 Thermoelectric Materials on Solar Thermal Energy Conversion Technologies †. *The Journal of Physical Chemistry B* **2010,** *114*, 14339–14342.

17. Tritt, T. M.; Boettner, H.; Chen, L., Thermoelectrics: Direct solar thermal energy conversion. *MRS Bull.* **2008,** *33*, 366-368.

18. SunShot, E. E. *US Department of Energy, 2012. SunShot Vision Study: February 2012. NREL Report No. BK5200-47927*; DOE/GO-102012-3037.

19. Yee, S. K.; LeBlanc, S.; Goodson, K. E.; Dames, C., $ per W metrics for thermoelectric power generation: beyond ZT. *Energy & Environmental Science* **2013,** *6*, 2561-2571.

20. LeBlanc, S.; Yee, S. K.; Scullin, M. L.; Dames, C.; Goodson, K. E., Material and manufacturing cost considerations for thermoelectrics. *Renewable and Sustainable Energy Reviews* **2014,** *32*, 313-327.

21. Anatychuk, L. I.; Luste, O. J. In *Problems of thermoelectric devices reliability*, Thermoelectrics, 1997. Proceedings ICT '97. XVI International Conference on, 26-29 Aug 1997, 1997; pp 632-635.

22. LeBlanc, S., Thermoelectric generators: Linking material properties and systems engineering for waste heat recovery applications. *Sustainable Materials and Technologies* **2014,** *1–2*, 26-35.

23. Amatya, R.; Ram, R. J., Trend for thermoelectric materials and their earth abundance. *Journal of electronic materials* **2012,** *41*, 1011-1019.

24. Rowe, D. M., Thermoelectrics handbook macro to nano. CRC/Taylor & Francis: Boca Raton, 2006.

25. Yaroshevsky, A., Abundances of chemical elements in the Earth’s crust. *Geochemistry International* **2006,** *44*, 48-55.

26. Suess, H. E.; Urey, H. C., Abundances of the elements. *Rev. Mod. Phys.* **1956,** *28*, 53-74.

27. Dresselhaus, M. S.; Chen, G.; Tang, M. Y.; Yang, R. G.; Lee, H.; Wang, D. Z.; Ren, Z. F.; Fleurial, J. P.; Gogna, P., New directions for low-dimensional thermoelectric materials. *Adv. Mater.* **2007,** *19*, 1043-1053.

28. Dresselhaus, M.; Chen, G.; Tang, M.; Yang, R.; Lee, H.; Wang, D.; Ren, Z.; Fleurial, J.; Gogna, P. In *New directions for nanoscale thermoelectric materials research*, MRS Proceedings2005 Cambridge Univ Press.

29. Kanatzidis, M. G.; Mahanti, S. D.; Hogan, T. P., *Chemistry, physics, and materials science of thermoelectric materials : beyond bismuth telluride*. Kluwer Academic/Plenum Publishers: New York, 2003; p 121-146.

30. Hicks, L. D.; Dresselhaus, M. S., Thermoelectric figure of merit of a one-dimensional conductor *Phys. Rev. B* **1993,** *47*, 16631-16634.

31. Hicks, L. D.; Dresselhaus, M. S., Effect of quantum-well structures on the thermoelectric figure of merit *Phys. Rev. B* **1993,** *47*, 12727-12731.

32. Hicks, L. D.; Harman, T. C.; Sun, X.; Dresselhaus, M. S., Experimental study of the effect of quantum-well structures on the thermoelectric figure of merit. *Phys. Rev. B* **1996,** *53*, 10493-10496.

33. Kanatzidis, M. G., Nanostructured Thermoelectrics: The New Paradigm? *Chem. Mat.* **2010,** *22*, 648-659.

34. Zhao, X.; Wei, C. M.; Yang, L.; Chou, M. Y., Quantum Confinement and Electronic Properties of Silicon Nanowires. *Physical Review Letters* **2004,** *92*, 236805.

35. Yoon, J. W.; Sasaki, T.; Roh, C. H.; Shim, S. H.; Shim, K. B.; Koshizaki, N., Quantum confinement effect of nanocrystalline GaN films prepared by pulsed-laser ablation under various Ar pressures. *Thin Solid Films* **2005,** *471*, 273-276.

36. Hanrath, T.; Korgel, B. A., Quantum confinement effects in germanium nanowires studied by electron energy loss spectroscopy (EELS). In *Physical Chemistry of*

Interfaces and Nanomaterials Iii, Hartland, G. V.; Zhu, X. Y., Eds.2004; Vol. 5513, pp 40-47.

37. Park, N.-M.; Choi, C.-J.; Seong, T.-Y.; Park, S.-J., Quantum Confinement in Amorphous Silicon Quantum Dots Embedded in Silicon Nitride. *Physical Review Letters* **2001,** *86*, 1355-1357.

38. Zaitsev, V. K.; Fedorov, M. I.; Gurieva, E. A.; Eremin, I. S.; Konstantinov, P. P.; Samunin, A. Y.; Vedernikov, M. V., Highly effective $Mg_2Si_{1-x}Sn_x$ thermoelectrics. *Phys. Rev. B* **2006,** *74*, 045207.

39. Bux, S. K.; Yeung, M. T.; Toberer, E. S.; Snyder, G. J.; Kaner, R. B.; Fleurial, J.-P., Mechanochemical synthesis and thermoelectric properties of high quality magnesium silicide. *Journal of Materials Chemistry* **2011,** *21*, 12259-12266.

40. Heller, M. W.; Danielson, G. C., Seebeck effect in Mg_2Si single crystals. *J. Phys. Chem. Solids* **1962,** *23*, 601-&.

41. Satyala, N.; Vashaee, D., Modeling of thermoelectric properties of magnesium silicide (Mg2Si). *Journal of electronic materials* **2012,** *41*, 1785-1791.

42. Yi, T.; Chen, S.; Li, S.; Yang, H.; Bux, S.; Bian, Z.; Katcho, N. A.; Shakouri, A.; Mingo, N.; Fleurial, J.-P.; Browning, N. D.; Kauzlarich, S. M., Synthesis and characterization of Mg2Si/Si nanocomposites prepared from MgH2 and silicon, and their thermoelectric properties. *Journal of Materials Chemistry* **2012,** *22*, 24805-24813.

43. Bashir, M. B. A.; Mohd Said, S.; Sabri, M. F. M.; Shnawah, D. A.; Elsheikh, M. H., Recent advances on Mg2Si1−xSnx materials for thermoelectric generation. *Renewable and Sustainable Energy Reviews* **2014,** *37,* 569-584.

44. Zaitsev, V.; Fedorov, M.; Gurieva, E.; Eremin, I.; Konstantinov, P.; Samunin, A. Y.; Vedernikov, M. In *Thermoelectrics of n-type with ZT> 1 based on Mg_2Si-Mg_2Sn solid solutions*, Thermoelectrics, 2005. ICT 2005. 24th International Conference on2005 IEEE; pp 204-210.

45. Muthiah, S.; Pulikkotil, J.; Srivastava, A. K.; Kumar, A.; Pathak, B. D.; Dhar, A.; Budhani, R. C., Conducting grain boundaries enhancing thermoelectric performance in doped Mg2Si. *Applied Physics Letters* **2013,** *103,* -.

46. Kang, Y.; Vaddiraju, S., Solid-State Phase Transformation as a Route for the Simultaneous Synthesis and Welding of Single-Crystalline Mg2Si Nanowires. *Chem. Mat.* **2014**.

47. Eliezer, D.; Alves, H., Corrosion and oxidation of magnesium alloys. *Handbook of materials selection* **2002**, 267-291.

48. Dai, B.; Sholl, D. S.; Johnson, J. K., First-principles investigation of adsorption and dissociation of hydrogen on Mg2Si surfaces. *The Journal of Physical Chemistry C* **2007,** *111,* 6910-6916.

49. Goldsmid, H. J., *Applications of thermoelectricity*. Methuen; Wiley: London,, 1960; p 80.

50. Madsen, G. K. H., Automated search for new thermoelectric materials: The case of LiZnSb. *J. Am. Chem. Soc.* **2006,** *128,* 12140-12146.

51. Mahan, G. D., Figure of merit for thermoelectrics *J. Appl. Phys.* **1989,** *65*, 1578-1583.

52. Vining, C. B., An inconvenient truth about thermoelectrics. *Nat. Mater.* **2009,** *8*, 83-85.

53. Shakouri, A., Recent Developments in Semiconductor Thermoelectric Physics and Materials. *Annual Review of Materials Research* **2011,** *41*, 399-431.

54. Zhao, L.-D.; Lo, S.-H.; Zhang, Y.; Sun, H.; Tan, G.; Uher, C.; Wolverton, C.; Dravid, V. P.; Kanatzidis, M. G., Ultralow thermal conductivity and high thermoelectric figure of merit in SnSe crystals. *Nature* **2014,** *508*, 373-377.

55. Biswas, K.; He, J.; Zhang, Q.; Wang, G.; Uher, C.; Dravid, V. P.; Kanatzidis, M. G., Strained endotaxial nanostructures with high thermoelectric figure of merit. *Nature Chemistry* **2011,** *3*, 160-166.

56. Goldsmid, H. J.; Douglas, R. W., The use of semiconductors in thermoelectric refrigeration. *British Journal of Applied Physics* **1954,** *5*, 386-390.

57. Vining, C. B.; Laskow, W.; Hanson, J. O.; Vanderbeck, R. R.; Gorsuch, P. D., Thermoelectric properties of pressure-sintered Si0.8Ge0.2 thermoelectric alloys *J. Appl. Phys.* **1991,** *69*, 4333-4340.

58. Sharp, J. W.; Jones, E. C.; Williams, R. K.; Martin, P. M.; Sales, B. C., Thermoelectric properties of $CoSb_3$ and related alloys. *J. Appl. Phys.* **1995,** *78*, 1013-1018.

59. Mahan, G.; Sales, B.; Sharp, J., Thermoelectric materials: New approaches to an old problem. *Phys. Today* **1997,** *50*, 42-47.

60. Heremans, J. P.; Thrush, C. M.; Morelli, D. T.; Wu, M.-C., Thermoelectric power of bismuth nanocomposites. *Physical review letters* **2002,** *88*, 216801.

61. Mingo, N., Thermoelectric figure of merit and maximum power factor in III-V semiconductor nanowires. *Applied Physics Letters* **2004,** *84*, 2652-2654.

62. Cornett, J. E.; Rabin, O., Effect of the energy dependence of the carrier scattering time on the thermoelectric power factor of quantum wells and nanowires. *Applied Physics Letters* **2012,** *100*, 242106.

63. Cornett, J. E.; Rabin, O., Universal scaling relations for the thermoelectric power factor of semiconducting nanostructures. *Phys. Rev. B* **2011,** *84*, 205410.

64. Cornett, J. E.; Rabin, O., Thermoelectric figure of merit calculations for semiconducting nanowires. *Applied Physics Letters* **2011,** *98*, 182104.

65. Kim, J.; Bahk, J. H.; Hwang, J.; Kim, H.; Park, H.; Kim, W., Thermoelectricity in semiconductor nanowires. *physica status solidi (RRL)-Rapid Research Letters* **2013,** *7*, 767-780.

66. Tritt, T. M., *Thermal conductivity: theory, properties, and applications*. Springer Science & Business Media2005.

67. Rowe, D. M., *Thermoelectrics handbook: macro to nano*. CRC press2005.

68. Hochbaum, A. I.; Chen, R. K.; Delgado, R. D.; Liang, W. J.; Garnett, E. C.; Najarian, M.; Majumdar, A.; Yang, P. D., Enhanced thermoelectric performance of rough silicon nanowires. *Nature* **2008,** *451*, 163-U5.

69. Tian, Y.; Sakr, M. R.; Kinder, J. M.; Liang, D.; MacDonald, M. J.; Qiu, R. L. J.; Gao, H.-J.; Gao, X. P. A., One-Dimensional Quantum Confinement Effect Modulated Thermoelectric Properties in InAs Nanowires. *Nano Letters* **2012,** *12*, 6492-6497.

70. Zuev, Y. M.; Lee, J. S.; Galloy, C.; Park, H.; Kim, P., Diameter Dependence of the Transport Properties of Antimony Telluride Nanowires. *Nano Letters* **2010,** *10*, 3037-3040.

71. Moon, J.; Kim, J.-H.; Chen, Z. C. Y.; Xiang, J.; Chen, R., Gate-Modulated Thermoelectric Power Factor of Hole Gas in Ge–Si Core–Shell Nanowires. *Nano Letters* **2013,** *13*, 1196-1202.

72. Wu, P. M.; Gooth, J.; Zianni, X.; Svensson, S. F.; Gluschke, J. G.; Dick, K. A.; Thelander, C.; Nielsch, K.; Linke, H., Large Thermoelectric Power Factor Enhancement Observed in InAs Nanowires. *Nano Letters* **2013,** *13*, 4080-4086.

73. Wingert, M. C.; Chen, Z. C. Y.; Dechaumphai, E.; Moon, J.; Kim, J.-H.; Xiang, J.; Chen, R., Thermal Conductivity of Ge and Ge–Si Core–Shell Nanowires in the Phonon Confinement Regime. *Nano Letters* **2011,** *11*, 5507-5513.

74. Boukai, A. I.; Bunimovich, Y.; Tahir-Kheli, J.; Yu, J. K.; Goddard, W. A.; Heath, J. R., Silicon nanowires as efficient thermoelectric materials. *Nature* **2008,** *451*, 168-171.

75. Lee, E. K.; Yin, L.; Lee, Y.; Lee, J. W.; Lee, S. J.; Lee, J.; Cha, S. N.; Whang, D.; Hwang, G. S.; Hippalgaonkar, K.; Majumdar, A.; Yu, C.; Choi, B. L.; Kim, J. M.; Kim, K., Large Thermoelectric Figure-of-Merits from SiGe Nanowires by

Simultaneously Measuring Electrical and Thermal Transport Properties. *Nano Letters* **2012,** *12*, 2918-2923.

76. Liang, W.; Hochbaum, A. I.; Fardy, M.; Rabin, O.; Zhang, M.; Yang, P., Field-effect modulation of Seebeck coefficient in single PbSe nanowires. *Nano letters* **2009,** *9*, 1689-1693.
77. Liang, W.; Rabin, O.; Hochbaum, A. I.; Fardy, M.; Zhang, M.; Yang, P., Thermoelectric properties of p-type PbSe nanowires. *Nano Research* **2010,** *2*, 394-399.
78. Seung Hyun, L.; Wooyoung, S.; So Young, J.; Jong Wook, R.; Philip, K.; Jeunghee, P.; Wooyoung, L., Thermoelectric properties of individual single-crystalline PbTe nanowires grown by a vapor transport method. *Nanotechnology* **2011,** *22*, 295707.
79. Biswas, K.; He, J.; Zhang, Q.; Wang, G.; Uher, C.; Dravid, V. P.; Kanatzidis, M. G., Strained endotaxial nanostructures with high thermoelectric figure of merit. *Nat Chem* **2011,** *3*, 160-166.
80. Biswas, K.; He, J.; Blum, I. D.; Wu, C.-I.; Hogan, T. P.; Seidman, D. N.; Dravid, V. P.; Kanatzidis, M. G., High-performance bulk thermoelectrics with all-scale hierarchical architectures. *Nature* **2012,** *489*, 414-418.
81. Mavrokefalos, A.; Moore, A. L.; Pettes, M. T.; Shi, L.; Wang, W.; Li, X., Thermoelectric and structural characterizations of individual electrodeposited bismuth telluride nanowires. *J. Appl. Phys.* **2009,** *105*, 104318.

82. Zhang, G.; Kirk, B.; Jauregui, L. A.; Yang, H.; Xu, X.; Chen, Y. P.; Wu, Y., Rational Synthesis of Ultrathin n-Type Bi2Te3 Nanowires with Enhanced Thermoelectric Properties. *Nano Letters* **2012,** *12*, 56-60.

83. Zhang, G.; Wang, W.; Li, X., Enhanced Thermoelectric Properties of Core/Shell Heterostructure Nanowire Composites. *Adv. Mater.* **2008,** *20*, 3654-3656.

84. Mingo, N., Thermoelectric figure of merit of II-VI semiconductor nanowires. *Applied Physics Letters* **2004,** *85*, 5986-5988.

85. Bui, C. T.; Xie, R.; Zheng, M.; Zhang, Q.; Sow, C. H.; Li, B.; Thong, J. T. L., Diameter-Dependent Thermal Transport in Individual ZnO Nanowires and its Correlation with Surface Coating and Defects. *Small* **2012,** *8*, 738-745.

86. Zhou, F.; Seol, J. H.; Moore, A. L.; Shi, L.; Ye, Q. L.; Scheffler, R., One-dimensional electron transport and thermopower in an individual InSb nanowire. *Journal of Physics: Condensed Matter* **2006,** *18*, 9651.

87. Abramson, A. R.; Kim, W. C.; Huxtable, S. T.; Yan, H.; Wu, Y.; Majumdar, A.; Tien, C.-L.; Yang, P., Fabrication and characterization of a nanowire/polymer-based nanocomposite for a prototype thermoelectric device. *Microelectromechanical Systems, Journal of* **2004,** *13*, 505-513.

88. Curtin, B. M.; Fang, E. W.; Bowers, J. E., Highly ordered vertical silicon nanowire array composite thin films for thermoelectric devices. *Journal of electronic materials* **2012,** *41*, 887-894.

89. Dávila, D.; Tarancón, A.; Fernández-Regúlez, M.; Calaza, C.; Salleras, M.; San Paulo, A.; Fonseca, L., Silicon nanowire arrays as thermoelectric material for a

power microgenerator. *Journal of Micromechanics and Microengineering* **2011,** *21*, 104007.

90. Keyani, J.; Stacy, A. M.; Sharp, J., Assembly and measurement of a hybrid nanowire-bulk thermoelectric device. *Applied physics letters* **2006,** *89*, 233106.

91. Li, Y.; Buddharaju, K.; Singh, N.; Lee, S., Top-down silicon nanowire-based thermoelectric generator: design and characterization. *Journal of electronic materials* **2012,** *41*, 989-992.

92. Heremans, J.; Thrush, C., Thermoelectric power of bismuth nanowires. *Phys. Rev. B* **1999,** *59*, 12579.

93. Biswas, K. G.; Sands, T. D.; Cola, B. A.; Xu, X., Thermal conductivity of bismuth telluride nanowire array-epoxy composite. *Applied Physics Letters* **2009,** *94*, 223116.

94. Survey, U. S. G. USGS Commodity Statistics and Information. http://minerals.usgs.gov/minerals/pubs/commodity/index.html

95. Casey, M. S.; Fahrenbruch, A. L.; Bube, R. H., Properties of zinc-phosphide junctions and interfaces. *J. Appl. Phys.* **1987,** *61*, 2941-2946.

96. Bhushan, M., Schottky solar cells on thin polycrystalline Zn_3P_2 films. *Applied Physics Letters* **1982,** *40*, 51-53.

97. Satyala, N.; Vashaee, D., The effect of crystallite size on thermoelectric properties of bulk nanostructured magnesium silicide (Mg2Si) compounds. *Applied Physics Letters* **2012,** *100*, 073107.

98. Satyala, N.; Vashaee, D., Detrimental influence of nanostructuring on the thermoelectric properties of magnesium silicide. *J. Appl. Phys.* **2012,** *112,* 093716.

99. Nicolaou, M. *The magnesium silicide germanide stannide alloy: A new concept in ocean thermal energy conversion*; Departamento de Engenharia Mecanica, Faculdade de Tecnologia, Universidade de Brasilia1983.

100. Elrod, U.; Lux-Steiner, M.; Bucher, E.; Hönigschmid, J.; Bickmann, K.; Gain, L., Morphological and structural properties of Zn_3P_2 single crystals grown by recrystallization in a closed system. *Journal of Crystal Growth* **1984,** *67,* 195-201.

101. Chen, X.; Weathers, A.; Carrete, J.; Mukhopadhyay, S.; Delaire, O.; Stewart, D. A.; Mingo, N.; Girard, S. N.; Ma, J.; Abernathy, D. L.; Yan, J.; Sheshka, R.; Sellan, D. P.; Meng, F.; Jin, S.; Zhou, J.; Shi, L., Twisting phonons in complex crystals with quasi-one-dimensional substructures. *Nature Communications* **2015,** *6,* 6723.

102. Hochbaum, A. I.; Chen, R.; Delgado, R. D.; Liang, W.; Garnett, E. C.; Najarian, M.; Majumdar, A.; Yang, P., Enhanced thermoelectric performance of rough silicon nanowires. *Nature* **2008,** *451,* 163-167.

103. Chen, R.; Hochbaum, A. I.; Murphy, P.; Moore, J.; Yang, P.; Majumdar, A., Thermal Conductance of Thin Silicon Nanowires. *Physical Review Letters* **2008,** *101,* 105501.

104. Zhou, F.; Moore, A. L.; Pettes, M. T.; Lee, Y.; Seol, J. H.; Ye, Q. L.; Rabenberg, L.; Shi, L., Effect of growth base pressure on the thermoelectric properties of indium antimonide nanowires. *J. Phys. D-Appl. Phys.* **2010,** *43.*

105. Brockway, L.; Vasiraju, V.; Sunkara, M. K.; Vaddiraju, S., Engineering Efficient Thermoelectrics from Large-Scale Assemblies of Doped ZnO Nanowires: Nanoscale

Effects and Resonant-Level Scattering. *ACS Applied Materials & Interfaces* **2014,** *6*, 14923-14930.

106. Boettcher, S. W.; Spurgeon, J. M.; Putnam, M. C.; Warren, E. L.; Turner-Evans, D. B.; Kelzenberg, M. D.; Maiolo, J. R.; Atwater, H. A.; Lewis, N. S., Energy-Conversion Properties of Vapor-Liquid-Solid-Grown Silicon Wire-Array Photocathodes. *Science* **2010,** *327*, 185-187.
107. Li, Y.; Wu, Y., Coassembly of graphene oxide and nanowires for large-area nanowire alignment. *J. Am. Chem. Soc.* **2009,** *131*, 5851-5857.
108. Smith, P. A.; Nordquist, C. D.; Jackson, T. N.; Mayer, T. S.; Martin, B. R.; Mbindyo, J.; Mallouk, T. E., Electric-field assisted assembly and alignment of metallic nanowires. *Applied Physics Letters* **2000,** *77*, 1399-1401.
109. Venkata, V.; Lance, B.; Shreyas, B.; Arun, S.; Sreeram, V., Shear induced simultaneous consolidation and alignment of silicon nanowires into ingots using equal channel angular extrusion (ECAE). *Materials Research Express* **2015,** *2*, 015013.
110. Segal, V., Materials processing by simple shear. *Materials Science and Engineering: A* **1995,** *197*, 157-164.
111. Zhang, Q.; He, J.; Zhu, T. J.; Zhang, S. N.; Zhao, X. B.; Tritt, T. M., High figures of merit and natural nanostructures in Mg2Si0.4Sn0.6 based thermoelectric materials. *Applied Physics Letters* **2008,** *93*, -.

112. Zhang, X.; Liu, H.; Lu, Q.; Zhang, J.; Zhang, F., Enhanced thermoelectric performance of Mg2Si0.4Sn0.6 solid solutions by in nanostructures and minute Bi-doping. *Applied Physics Letters* **2013,** *103*, -.

113. Jung, J.-Y.; Kim, I.-H., Synthesis and thermoelectric properties of n-Type Mg2Si. *Electron. Mater. Lett.* **2010,** *6*, 187-191.

114. Jung, J.-Y.; Park, K.-H.; Kim, I.-H. In *Thermoelectric Properties of Sb-doped Mg2Si Prepared by Solid-State Synthesis*, IOP Conference Series: Materials Science and Engineering2011 IOP Publishing; p 142006.

115. Khan, A. U.; Vlachos, N.; Kyratsi, T., High thermoelectric figure of merit of Mg2Si0.55Sn0.4Ge0.05 materials doped with Bi and Sb. *Scripta Materialia* **2013,** *69*, 606-609.

116. Luo, W.; Yang, M.; Chen, F.; Shen, Q.; Jiang, H.; Zhang, L., Preparation and Thermoelectric Properties of Bi-Doped Mg2Si0. 8Sn0. 2 Compound. *Materials transactions* **2010,** *51*, 288.

117. Tani, J.-i.; Kido, H., Thermoelectric properties of Al-doped Mg2Si1−xSnx (x<=0.1). *Journal of Alloys and Compounds* **2008,** *466*, 335-340.

118. Zhang, Q.; He, J.; Zhao, X.; Zhang, S.; Zhu, T.; Yin, H.; Tritt, T., In situ synthesis and thermoelectric properties of La-doped Mg2 (Si, Sn) composites. *Journal of Physics D: Applied Physics* **2008,** *41*, 185103.

119. Liu, W.; Tang, X.; Li, H.; Sharp, J.; Zhou, X.; Uher, C., Optimized Thermoelectric Properties of Sb-Doped $Mg_{2(1+z)}Si_{0.5-y}Sn_{0.5}S$ by through Adjustment of the Mg Content. *Chem. Mat.* **2011,** *23*, 5256-5263.

120. Kambe, K.; Udono, H., Convenient Melt-Growth Method for Thermoelectric Mg_2Si. *Journal of Electronic Materials* **2014,** *43*, 2212-2217.

121. Isoda, Y.; Tada, S.; Nagai, T.; Fujiu, H.; Shinohara, Y., Thermoelectric Properties of p-Type Mg2.00Si0.25Sn0.75 with Li and Ag Double Doping. *Journal of Electronic Materials* **2010,** *39*, 1531-1535.

122. Sakamoto, T.; Iida, T.; Matsumoto, A.; Honda, Y.; Nemoto, T.; Sato, J.; Nakajima, T.; Taguchi, H.; Takanashi, Y., Thermoelectric Characteristics of a Commercialized Mg_2Si Source Doped with Al, Bi, Ag, and Cu. *Journal of Electronic Materials* **2010,** *39*, 1708-1713.

123. Tani, J.-i.; Kido, H., Thermoelectric properties of Bi-doped Mg2Si semiconductors. *Physica B: Condensed Matter* **2005,** *364*, 218-224.

124. Tani, J.-i.; Kido, H., Thermoelectric properties of Sb-doped Mg2Si semiconductors. *Intermetallics* **2007,** *15*, 1202-1207.

125. Kang, Y.; Brockway, L.; Vaddiraju, S., A simple phase transformation strategy for converting silicon nanowires into metal silicide nanowires: Magnesium silicide. *Materials Letters* **2013,** *100*, 106-110.

126. Brockway, L.; Van Laer, M.; Kang, Y.; Vaddiraju, S., Large-scale synthesis and in situ functionalization of Zn_3P_2 and Zn_4Sb_3 nanowire powders. *Phys. Chem. Chem. Phys.* **2013,** *15*, 6260-6267.

127. Brockway, L.; Van Laer, M.; Kang, Y.; Vaddiraju, S., Large-scale synthesis and in situ functionalization of Zn_3P_2 and Zn_4Sb_3 nanowire powders. *Physical Chemistry Chemical Physics* **2013,** *15*, 6260-6267.

128. Hochbaum, A. I.; Gargas, D.; Hwang, Y. J.; Yang, P. D., Single Crystalline Mesoporous Silicon Nanowires. *Nano Letters* **2009,** *9*, 3550-3554.

129. Tian, B.; Kempa, T. J.; Lieber, C. M., Single nanowire photovoltaics. *Chemical Society Reviews* **2009,** *38*, 16-24.

130. Mikolajick, T.; Heinzig, A.; Trommer, J.; Pregl, S.; Grube, M.; Cuniberti, G.; Weber, W. M., Silicon nanowires - a versatile technology platform. *Phys. Status Solidi-Rapid Res. Lett.* **2013,** *7*, 793-799.

131. Brockway, L.; Vasiraju, V.; Asayesh-Ardakani, H.; Shahbazian-Yassar, R.; Vaddiraju, S., Thermoelectric properties of large-scale Zn_3P_2 nanowire assemblies. *Nanotechnology* **2014,** *25*, 145401.

132. Law, M.; Goldberger, J.; Yang, P. D., Semiconductor nanowires and nanotubes. *Annual Review of Materials Research* **2004,** *34*, 83-122.

133. Sumirat, I.; Ando, Y.; Shimamura, S., Theoretical consideration of the effect of porosity on thermal conductivity of porous materials. *Journal of Porous Materials* **2006,** *13*, 439-443.

134. Euler, F., Simple Geometric Model for the Effect of Porosity on Material Constants. *J. Appl. Phys.* **1957,** *28*, 1342-1345.

135. Abreu, C. R. A.; Tavares, F. W.; Castier, M., Influence of particle shape on the packing and on the segregation of spherocylinders via Monte Carlo simulations. *Powder Technol.* **2003,** *134*, 167-180.

136. Elnathan, R.; Kwiat, M.; Patolsky, F.; Voelcker, N. H., Engineering vertically aligned semiconductor nanowire arrays for applications in the life sciences. *Nano Today* **2014,** *9*, 172-196.

137. Wang, K.; Wu, H. P.; Meng, Y. N.; Wei, Z. X., Conducting Polymer Nanowire Arrays for High Performance Supercapacitors. *Small* **2014,** *10*, 14-31.

138. Cao, A. P.; Sudholter, E. J. R.; de Smet, L., Silicon Nanowire-Based Devices for Gas-Phase Sensing. *Sensors* **2014,** *14*, 245-271.

139. Rim, T.; Baek, C. K.; Kim, K.; Jeong, Y. H.; Lee, J. S.; Meyyappan, M., Silicon Nanowire Biologically Sensitive Field Effect Transistors: Electrical Characteristics and Applications. *J. Nanosci. Nanotechnol.* **2014,** *14*, 273-287.

140. Li, B. R.; Chen, C. C.; Kumar, U. R.; Chen, Y. T., Advances in nanowire transistors for biological analysis and cellular investigation. *Analyst* **2014,** *139*, 1589-1608.

141. Li, Y.; Qian, F.; Xiang, J.; Lieber, C. M., Nanowire electronic and optoelectronic devices. *Materials Today* **2006,** *9*, 18-27.

142. Yan, R. X.; Gargas, D.; Yang, P. D., Nanowire photonics. *Nat. Photonics* **2009,** *3*, 569-576.

143. Wang, Z. L., ZnO nanowire and nanobelt platform for nanotechnology. *Mater. Sci. Eng. R-Rep.* **2009,** *64*, 33-71.

144. Lance, B.; Venkata, V.; Hasti, A.-A.; Reza, S.-Y.; Sreeram, V., Thermoelectric properties of large-scale Zn 3 P 2 nanowire assemblies. *Nanotechnology* **2014,** *25*, 145401.

145. Yang, P.; Yan, H.; Mao, S.; Russo, R.; Johnson, J.; Saykally, R.; Morris, N.; Pham, J.; He, R.; Choi, H.-J., Controlled growth of ZnO nanowires and their optical properties. *Advanced Functional Materials* **2002,** *12*, 323.

146. Tsakalakos, L.; Balch, J.; Fronheiser, J.; Korevaar, B.; Sulima, O.; Rand, J., Silicon nanowire solar cells. *Applied Physics Letters* **2007,** *91*, 233117.

147. Elias, J.; Tena-Zaera, R.; Lévy-Clément, C., Electrochemical deposition of ZnO nanowire arrays with tailored dimensions. *Journal of Electroanalytical Chemistry* **2008,** *621*, 171-177.

148. Pereira, A.; Gallardo, C.; Espejo, A. P.; Briones, J.; Vivas, L. G.; Vázquez, M.; Denardin, J. C.; Escrig, J., Tailoring the magnetic properties of ordered 50-nm-diameter CoNi nanowire arrays. *J Nanopart Res* **2013,** *15*, 1-8.

149. Park, W. I.; Yi, G. C.; Kim, M.; Pennycook, S. J., Quantum confinement observed in ZnO/ZnMgO nanorod heterostructures. *Adv. Mater.* **2003,** *15*, 526-529.

150. Hu, J.; Odom, T. W.; Lieber, C. M., Chemistry and physics in one dimension: synthesis and properties of nanowires and nanotubes. *Accounts of Chemical Research* **1999,** *32*, 435-445.

151. Yu, G.; Cao, A.; Lieber, C. M., Large-area blown bubble films of aligned nanowires and carbon nanotubes. *Nature nanotechnology* **2007,** *2*, 372-377.

152. Bruce, P. G.; Scrosati, B.; Tarascon, J.-M., Nanomaterials for rechargeable lithium batteries. *Angewandte Chemie-International Edition* **2008,** *47*, 2930-2946.

153. Chen, X.; Mao, S. S., Titanium dioxide nanomaterials: Synthesis, properties, modifications, and applications. *Chemical Reviews* **2007,** *107*, 2891-2959.

154. Moghimi, S. M.; Hunter, A. C.; Murray, J. C., Nanomedicine: current status and future prospects. *The FASEB Journal* **2005,** *19*, 311-330.

155. Rao, C.; Cheetham, A., Science and technology of nanomaterials: current status and future prospects. *J. Mater. Chem.* **2001,** *11*, 2887-2894.

156. Rao, C.; Govindaraj, A.; Vivekchand, S., Inorganic nanomaterials: current status and future prospects. *Annual Reports Section" A"(Inorganic Chemistry)* **2006,** *102*, 20-45.

157. Rao, C. N. R.; Sood, A. K.; Subrahmanyam, K. S.; Govindaraj, A., Graphene: The New Two-Dimensional Nanomaterial. *Angewandte Chemie-International Edition* **2009,** *48*, 7752-7777.

158. Cui, Y.; Zhong, Z.; Wang, D.; Wang, W. U.; Lieber, C. M., High performance silicon nanowire field effect transistors. *Nano Letters* **2003,** *3*, 149-152.

159. Yan, R.; Gargas, D.; Yang, P., Nanowire photonics. *Nat. Photonics* **2009,** *3*, 569-576.

160. Wu, Y. M.; Zhang, X. J.; Pan, H. H.; Deng, W.; Zhang, X. H.; Zhang, X. W.; Jie, J. S., In-situ device integration of large-area patterned organic nanowire arrays for high-performance optical sensors. *Sci Rep* **2013,** *3*, 1-8.

161. Garnett, E. C.; Brongersma, M. L.; Cui, Y.; McGehee, M. D., Nanowire solar cells. *Annual Review of Materials Research* **2011,** *41*, 269-295.

162. Lu, C.-Y.; Shoou-Jinn, C.; Chang, S.-P.; Lee, C.-T.; Che-Fu, K.; Hong-Ming, C.; Chiou, Y.; Cheng-Liang, H.; Chen, I. C., Ultraviolet photodetectors with ZnO

nanowires prepared on ZnO:Ga/glass templates. *Applied Physics Letters* **2006,** *89*, 153101-153101-3.

163. Patolsky, F.; Zheng, G.; Lieber, C. M., Nanowire-based biosensors. *Analytical Chemistry* **2006,** *78*, 4260-4269.

164. Wanekaya, A. K.; Chen, W.; Myung, N. V.; Mulchandani, A., Nanowire-based electrochemical biosensors. *Electroanalysis* **2006,** *18*, 533-550.

165. Garnett, E.; Yang, P., Light trapping in silicon nanowire solar cells. *Nano letters* **2010,** *10*, 1082-1087.

166. Rosfjord, K. M.; Yang, J. K.; Dauler, E. A.; Kerman, A. J.; Anant, V.; Voronov, B. M.; Gol'Tsman, G. N.; Berggren, K. K., Nanowire single-photon detector with an integrated optical cavity and anti-reflection coating. *Optics Express* **2006,** *14*, 527-534.

167. Pyayt, A. L.; Wiley, B.; Xia, Y.; Chen, A.; Dalton, L., Integration of photonic and silver nanowire plasmonic waveguides. *Nature nanotechnology* **2008,** *3*, 660-665.

168. Greytak, A. B.; Barrelet, C. J.; Li, Y.; Lieber, C. M., Semiconductor nanowire laser and nanowire waveguide electro-optic modulators. *Applied Physics Letters* **2005,** *87*, 151103.

169. Chin, A. H.; Ahn, T. S.; Li, H.; Vaddiraju, S.; Bardeen, C. J.; Ning, C.-Z.; Sunkara, M. K., Photoluminescence of GaN nanowires of different crystallographic orientations. *Nano letters* **2007,** *7*, 626-631.

170. Bendall, J. S.; Etgar, L.; Tan, S. C.; Cai, N.; Wang, P.; Zakeeruddin, S. M.; Graetzel, M.; Welland, M. E., An efficient DSSC based on ZnO nanowire photo-anodes and a new D-pi-A organic dye. *Energy & Environmental Science* **2011,** *4*, 2903-2908.

171. Wang, M.; Wang, Y.; Li, J., ZnO nanowire arrays coating on TiO2 nanoparticles as a composite photoanode for a high efficiency DSSC. *Chemical Communications* **2011,** *47*, 11246-11248.

172. Duan, X.; Huang, Y.; Agarwal, R.; Lieber, C. M., Single-nanowire electrically driven lasers. *Nature* **2003,** *421*, 241-245.

173. Kelzenberg, M. D.; Turner-Evans, D. B.; Kayes, B. M.; Filler, M. A.; Putnam, M. C.; Lewis, N. S.; Atwater, H. A., Photovoltaic measurements in single-nanowire silicon solar cells. *Nano letters* **2008,** *8*, 710-714.

174. Meyyappan, M.; Sunkara, M. K., *Inorganic nanowires: applications, properties, and characterization*. CRC Press, Inc.2009.

175. Yao, J.; Yan, H.; Lieber, C. M., A nanoscale combing technique for the large-scale assembly of highly aligned nanowires. *Nature nanotechnology* **2013**.

176. Hangarter, C. M.; Myung, N. V., Magnetic alignment of nanowires. *Chem. Mat.* **2005,** *17*, 1320-1324.

177. Tanase, M.; Bauer, L. A.; Hultgren, A.; Silevitch, D. M.; Sun, L.; Reich, D. H.; Searson, P. C.; Meyer, G. J., Magnetic alignment of fluorescent nanowires. *Nano Letters* **2001,** *1*, 155-158.

178. Lee, S.-W.; Jeong, M.-C.; Myoung, J.-M.; Chae, G.-S.; Chung, I.-J., Magnetic alignment of ZnO nanowires for optoelectronic device applications. *Applied physics letters* **2007,** *90,* 133115-133115-3.

179. Cao, Y.; Liu, W.; Sun, J.; Han, Y.; Zhang, J.; Liu, S.; Sun, H.; Guo, J., A technique for controlling the alignment of silver nanowires with an electric field. *Nanotechnology* **2006,** *17,* 2378.

180. Tao, A.; Kim, F.; Hess, C.; Goldberger, J.; He, R.; Sun, Y.; Xia, Y.; Yang, P., Langmuir-Blodgett silver nanowire monolayers for molecular sensing using surface-enhanced Raman spectroscopy. *Nano Letters* **2003,** *3,* 1229-1233.

181. Yang, P., Nanotechnology: Wires on water. *Nature* **2003,** *425*, 243-244.

182. Fan, Z.; Ho, J. C.; Jacobson, Z. A.; Yerushalmi, R.; Alley, R. L.; Razavi, H.; Javey, A., Wafer-scale assembly of highly ordered semiconductor nanowire arrays by contact printing. *Nano letters* **2008,** *8,* 20-25.

183. Yerushalmi, R.; Jacobson, Z. A.; Ho, J. C.; Fan, Z.; Javey, A., Large scale, highly ordered assembly of nanowire parallel arrays by differential roll printing. *Applied Physics Letters* **2007,** *91*, 203104-203104-3.

184. Ko, D.-C.; Kim, B.-M., The prediction of central burst defects in extrusion and wire drawing. *Journal of Materials Processing Technology* **2000,** *102,* 19-24.

185. Suwas, S.; Arruffat-Massion, R.; Tóth, L.; Eberhardt, A.; Fundenberger, J.-J.; Skrotzki, W., Evolution of crystallographic texture during equal channel angular extrusion of copper: The role of material variables. *Metall and Mat Trans A* **2006,** *37*, 739-753.

186. Robertson, J.; Im, J.-T.; Karaman, I.; Hartwig, K.; Anderson, I., Consolidation of amorphous copper based powder by equal channel angular extrusion. *Journal of non-crystalline solids* **2003,** *317*, 144-151.

187. Furukawa, M.; Horita, Z.; Nemoto, M.; Langdon, T., Review: Processing of metals by equal-channel angular pressing. *Journal of materials science* **2001,** *36*, 2835-2843.

188. Segal, V., Equal channel angular extrusion: from macromechanics to structure formation. *Materials Science and Engineering: A* **1999,** *271*, 322-333.

189. Gholinia, A.; Bate, P.; Prangnell, P., Modelling texture development during equal channel angular extrusion of aluminium. *Acta materialia* **2002,** *50*, 2121-2136.

190. Li, S.; Gazder, A. A.; Beyerlein, I. J.; Pereloma, E. V.; Davies, C. H., Effect of processing route on microstructure and texture development in equal channel angular extrusion of interstitial-free steel. *Acta materialia* **2006,** *54*, 1087-1100.

191. Pithan, C.; Hashimoto, T.; Kawazoe, M.; Nagahora, J.; Higashi, K., Microstructure and texture evolution in ECAE processed A5056. *Materials Science and Engineering: A* **2000,** *280*, 62-68.

192. Iwahashi, Y.; Horita, Z.; Nemoto, M.; Langdon, T. G., The process of grain refinement in equal-channel angular pressing. *Acta Materialia* **1998,** *46*, 3317-3331.

193. Valiev, R. Z.; Langdon, T. G., Principles of equal-channel angular pressing as a processing tool for grain refinement. *Progress in Materials Science* **2006,** *51*, 881-981.

194. Oh-Ishi, K.; Horita, Z.; Nemoto, M.; Furukawa, M.; Langdon, T. G., Optimizing the rotation conditions for grain refinement in equal-channel angular pressing. *Metall and Mat Trans A* **1998,** *29*, 2011-2013.

195. Agarwal, A.; Bakshi, S. R.; Lahiri, D., *Carbon nanotubes: Reinforced metal matrix composites*. Taylor & Francis US2010.

196. Pham, Q.; Jeong, Y. G.; Hong, S. H.; Kim, H. S., Equal channel angular pressing of carbon nanotube reinforced metal matrix nanocomposites. *Key Engineering Materials* **2006,** *326*, 325-328.

197. Pham, Q.; Jeong, Y. G.; Yoon, S. C.; Hong, S. I.; Hong, S. H.; Kim, H. S. In *Carbon nanotube reinforced metal matrix nanocomposites via equal channel angular pressing*, Materials science forum2007 Trans Tech Publ; pp 245-248.

198. Quang, P.; Jeong, Y. G.; Yoon, S. C.; Hong, S. H.; Kim, H. S., Consolidation of 1 vol.% carbon nanotube reinforced metal matrix nanocomposites via equal channel angular pressing. *Journal of Materials Processing Technology* **2007,** *187–188*, 318-320.

199. Kang, Y.; Brockway, L.; Vaddiraju, S., A Simple Phase Transformation Strategy for Converting Silicon Nanowires into Metal Silicide Nanowires: Magnesium Silicide. *Materials Letters* **2013**.

200. Peng, K.; Jie, J.; Zhang, W.; Lee, S.-T., Silicon nanowires for rechargeable lithium-ion battery anodes. *Applied Physics Letters* **2008,** *93*, 033105.

201. Peng, K.; Hu, J.; Yan, Y.; Wu, Y.; Fang, H.; Xu, Y.; Lee, S.; Zhu, J., Fabrication of Single-Crystalline Silicon Nanowires by Scratching a Silicon Surface with Catalytic Metal Particles. *Advanced Functional Materials* **2006,** *16*, 387-394.

202. Youssef, K. M.; Scattergood, R. O.; Murty, K. L.; Horton, J. A.; Koch, C. C., Ultrahigh strength and high ductility of bulk nanocrystalline copper. *Applied Physics Letters* **2005,** *87*, 091904.

203. Cui, H.; Goforth, R.; Hartwig, K., The three dimensional simulation of flow pattern in equal-channel angular extrusion. *JOM-e* **1998,** *50*.

204. Stan, G.; Krylyuk, S.; Davydov, A.; Levin, I.; Cook, R., Ultimate bending strength of si nanowires. *Nano letters* **2012,** *12*, 2599-2604.

205. Kang, Y.; Vaddiraju, S., Solid-State Phase Transformation as a Route for the Simultaneous Synthesis and Welding of Single-Crystalline Mg2Si Nanowires. *Chemistry of Materials* **2014,** *26*, 2814-2819.

206. Holmberg, V. C.; Korgel, B. A., Corrosion Resistance of Thiol- and Alkene-Passivated Germanium Nanowires. *Chem. Mat.* **2010,** *22*, 3698-3703.

207. Adhikari, H.; McIntyre, P. C.; Sun, S.; Pianetta, P.; Chidsey, C. E., Photoemission studies of passivation of germanium nanowires. *Applied Physics Letters* **2005,** *87*, 263109-3.

208. Bashouti, M. Y.; Stelzner, T.; Berger, A.; Christiansen, S.; Haick, H., Chemical Passivation of Silicon Nanowires with C1−C6 Alkyl Chains through Covalent Si−C Bonds. *The Journal of Physical Chemistry C* **2008,** *112*, 19168-19172.

209. Aricò, A. S.; Bruce, P.; Scrosati, B.; Tarascon, J.-M.; Van Schalkwijk, W., Nanostructured materials for advanced energy conversion and storage devices. *Nat. Mater.* **2005,** *4*, 366-377.

210. Cao, G., *Nanostructures and nanomaterials*. Imperial college press2004.

211. Rao, C. N. R.; Müller, A.; Cheetham, A. K., *The chemistry of nanomaterials*. Wiley. com2006; Vol. 1.

212. Wang, D.; Chang, Y.-L.; Liu, Z.; Dai, H., Oxidation resistant germanium nanowires: Bulk synthesis, long chain alkanethiol functionalization, and Langmuir-Blodgett assembly. *J. Am. Chem. Soc.* **2005,** *127*, 11871-11875.

213. Hanrath, T.; Korgel, B. A., Chemical Surface Passivation of Ge Nanowires. *J. Am. Chem. Soc.* **2004,** *126*, 15466-15472.

214. Kimball, G. M.; Bosco, J. P.; Müller, A. M.; Tajdar, S. F.; Brunschwig, B. S.; Atwater, H. A.; Lewis, N. S., Passivation of Zn_3P_2 substrates by aqueous chemical etching and air oxidation. *J. Appl. Phys.* **2012,** *112*, 106101.

215. Nayar, P.; Catalano, A., Zinc phosphide-zinc oxide heterojunction solar cells. *Applied Physics Letters* **1981,** *39*, 105-107.

216. Chopra, K.; Paulson, P.; Dutta, V., Thin-film solar cells: an overview. *Progress in Photovoltaics: Research and Applications* **2004,** *12*, 69-92.

217. Bhushan, M.; Catalano, A., Polycrystalline Zn_3P_2 Schottky barrier solar cells. *Applied Physics Letters* **1981,** *38*, 39-41.

218. Misiewicz, J., Minority-carrier diffusion length in Zn_3P_2. *physica status solidi (a)* **1981,** *65*, K95-K97.

219. Wyeth, N.; Catalano, A., Spectral response measurements of minority-carrier diffusion length in Zn 3 P 2. *J. Appl. Phys.* **1979,** *50*, 1403-1407.

220. Eason, C.; Ross, J.; Blackie, H.; Fairweather, A., Toxicology and ecotoxicology of zinc phosphide as used for pest control in New Zealand. *New Zealand Journal of Ecology* **2013,** *37*, 1-11.

221. Greenberg, J.; Lazarev, V.; Kozlov, S.; Shevchenko, V., The sublimation thermodynamics of Zn_3P_2. *The Journal of Chemical Thermodynamics* **1974,** *6*, 1005-1012.

222. Wang, F.-C.; Bube, R. H.; Feigelson, R. S.; Route, R. K., Single crystal growth of Zn_3P_2. *Journal of Crystal Growth* **1981,** *55*, 268-272.

223. Yin, H.; Christensen, M.; Pedersen, B.; Nishibori, E.; Aoyagi, S.; Iversen, B. B., Thermal Stability of Thermoelectric Zn_4Sb_3. *Journal of electronic materials* **2010,** *39*, 1957-1959.

224. Schlecht, S.; Erk, C.; Yosef, M., Nanoscale zinc antimonides: synthesis and phase stability. *Inorganic chemistry* **2006,** *45*, 1693-1697.

225. Koumoto, K.; Wang, Y.; Zhang, R.; Kosuga, A.; Funahashi, R., Oxide thermoelectric materials: a nanostructuring approach. *Annual Review of Materials Research* **2010,** *40*, 363-394.

226. Srikant, V.; Clarke, D. R., On the optical band gap of zinc oxide. *J. Appl. Phys.* **1998,** *83*, 5447-5451.

227. Tsukazaki, A.; Ohtomo, A.; Onuma, T.; Ohtani, M.; Makino, T.; Sumiya, M.; Ohtani, K.; Chichibu, S. F.; Fuke, S.; Segawa, Y., Repeated temperature modulation epitaxy

for p-type doping and light-emitting diode based on ZnO. *Nat. Mater.* **2004,** *4*, 42-46.

228. Horsthuis, W. H., ZnO processing for integrated optic sensors. *Thin Solid Films* **1986,** *137*, 185-192.
229. Willander, M.; Nur, O.; Zhao, Q.; Yang, L.; Lorenz, M.; Cao, B.; Pérez, J. Z.; Czekalla, C.; Zimmermann, G.; Grundmann, M., Zinc oxide nanorod based photonic devices: recent progress in growth, light emitting diodes and lasers. *Nanotechnology* **2009,** *20*, 332001.
230. Lee, C.-P.; Chou, C.-Y.; Chen, C.-Y.; Yeh, M.-H.; Lin, L.-Y.; Vittal, R.; Wu, C.-G.; Ho, K.-C., Zinc oxide-based dye-sensitized solar cells with a ruthenium dye containing an alkyl bithiophene group. *Journal of Power Sources* **2013**, 1-9.
231. Nesakumar, N.; Thandavan, K.; Sethuraman, S.; Krishnan, U. M.; Rayappan, J. B. B., An electrochemical biosensor with nanointerface for lactate detection based on lactate dehydrogenase immobilized on zinc oxide nanorods. *Journal of colloid and interface science* **2014,** *414*, 90-96.
232. Eda, K.; Iga, A.; Matsuoka, M., Degradation mechanism of non-Ohmic zinc oxide ceramics. *J. Appl. Phys.* **1980,** *51*, 2678-2684.
233. Escalera-Lozano, R.; Gutiérrez-Chavarría, C. A.; Pech-Canul, M. A.; Pech-Canul, M. I. In *Degradation of Al/SiCp Composites Processed with Fly Ash via Reactive Infiltration*, Materials Science Forum2007 Trans Tech Publ; pp 139-144.
234. Hidding, B.; Pfitzner, M.; Simone, D.; Bruno, C., Review of the potential of silanes as rocket/scramjet fuels. *Acta Astronautica* **2008,** *63*, 379-388.

235. Adlkofer, K.; Eck, W.; Grunze, M.; Tanaka, M., Surface engineering of gallium arsenide with 4-mercaptobiphenyl monolayers. *The Journal of Physical Chemistry B* **2003,** *107*, 587-591.

236. Myung, N.; Bae, Y.; Bard, A. J., Effect of surface passivation on the electrogenerated chemiluminescence of CdSe/ZnSe nanocrystals. *Nano Letters* **2003,** *3*, 1053-1055.

237. Wang, X.-S.; Dykstra, T. E.; Salvador, M. R.; Manners, I.; Scholes, G. D.; Winnik, M. A., Surface passivation of luminescent colloidal quantum dots with poly (dimethylaminoethyl methacrylate) through a ligand exchange process. *J. Am. Chem. Soc.* **2004,** *126*, 7784-7785.

238. Holmberg, V. C.; Rasch, M. R.; Korgel, B. A., PEGylation of Carboxylic Acid-Functionalized Germanium Nanowires. *Langmuir* **2010,** *26*, 14241-14246.

239. Jenny, H.; Gessel, S.; Bingham, F., Comparative study of decomposition rates of organic matter in temperate and tropical regions. *Soil Science* **1949,** *68*, 419-432.

240. Tennakone, K.; Wickramanayake, S.; Samarasekara, P.; Fernando, C., Doping of semiconductor particles with salts. *physica status solidi (a)* **1987,** *104*, K57-K60.

241. Kazakov, I. V.; Timoshkin, A. Y., Vaporization and thermal decomposition of B,B′,B″-tribromoborazine. *Russ. J. Inorg. Chem.* **2012,** *57*, 557-563.

242. Murphy, A. B., Band-gap determination from diffuse reflectance measurements of semiconductor films, and application to photoelectrochemical water-splitting. *Solar Energy Materials and Solar Cells* **2007,** *91*, 1326-1337.

243. Bhattacharya, S.; Banerjee, D.; Adu, K. W.; Samui, S.; Bhattacharyya, S., Confinement in silicon nanowires: Optical properties. *Applied Physics Letters* **2004,** *85*, 2008-2010.

244. Han, W.-Q.; Zettl, A., GaN nanorods coated with pure BN. *Applied Physics Letters* **2002,** *81*, 5051-5053.

245. Black, B.; Nelson, D. W.; Webb, C.; Samra, N. In *3D processing technology and its impact on iA32 microprocessors*, Computer Design: VLSI in Computers and Processors, 2004. ICCD 2004. Proceedings. IEEE International Conference on2004 IEEE; pp 316-318.

246. Brooks, D.; Dick, R. P.; Joseph, R.; Shang, L., Power, thermal, and reliability modeling in nanometer-scale microprocessors. *Ieee Micro* **2007**, 49-62.

247. Kursun, E.; Cher, C.-Y.; Buyuktosunoglu, A.; Bose, P. In *Investigating the effects of task scheduling on thermal behavior*, Third Workshop on Temperature-Aware Computer Systems (TACS’06)2006.

248. Li, P.; Pileggi, L. T.; Asheghi, M.; Chandra, R. In *Efficient full-chip thermal modeling and analysis*, Computer Aided Design, 2004. ICCAD-2004. IEEE/ACM International Conference on2004 IEEE; pp 319-326.

249. Yang, J.; Wang, Y.; Chen, Y., GPU accelerated molecular dynamics simulation of thermal conductivities. *Journal of Computational Physics* **2007,** *221*, 799-804.

250. Collange, S.; Defour, D.; Tisserand, A., Power consumption of GPUs from a software perspective. In *Computational Science–ICCS 2009*, Springer2009; pp 914-923.

251. Cebrian, J. M.; Guerrero, G. D.; Garcia, J. M. In *Energy efficiency analysis of GPUs*, Parallel and Distributed Processing Symposium Workshops & PhD Forum (IPDPSW), 2012 IEEE 26th International2012 IEEE; pp 1014-1022.

252. Nolas, G. S.; Morelli, D. T.; Tritt, T. M., Skutterudites: A phonon-glass-electron crystal approach to advanced thermoelectric energy conversion applications. *Annu. Rev. Mater. Sci.* **1999,** *29*, 89-116.

253. Tritt, T. M.; Subramanian, M. A., Thermoelectric materials, phenomena, and applications: A bird's eye view. *MRS Bull.* **2006,** *31*, 188-194.

254. Snyder, G. J.; Christensen, M.; Nishibori, E.; Caillat, T.; Iversen, B. B., Disordered zinc in Zn_4Sb_3 with phonon-glass and electron-crystal thermoelectric properties. *Nat. Mater.* **2004,** *3*, 458-463.

255. Eastman, J. A.; Choi, S.; Li, S.; Yu, W.; Thompson, L., Anomalously increased effective thermal conductivities of ethylene glycol-based nanofluids containing copper nanoparticles. *Applied physics letters* **2001,** *78*, 718-720.

256. Chol, S., Enhancing thermal conductivity of fluids with nanoparticles. *ASME-Publications-Fed* **1995,** *231*, 99-106.

257. Tuckerman, D. B.; Pease, R., High-performance heat sinking for VLSI. *Electron Device Letters, IEEE* **1981,** *2*, 126-129.

258. Kim, W.; Zide, J.; Gossard, A.; Klenov, D.; Stemmer, S.; Shakouri, A.; Majumdar, A., Thermal conductivity reduction and thermoelectric figure of merit increase by embedding nanoparticles in crystalline semiconductors. *Physical Review Letters* **2006,** *96*, 045901.

259. Poudel, B.; Hao, Q.; Ma, Y.; Lan, Y.; Minnich, A.; Yu, B.; Yan, X.; Wang, D.; Muto, A.; Vashaee, D., High-thermoelectric performance of nanostructured bismuth antimony telluride bulk alloys. *Science* **2008,** *320*, 634-638.

260. Wei, N.; Xu, L.; Wang, H.-Q.; Zheng, J.-C., Strain engineering of thermal conductivity in graphene sheets and nanoribbons: a demonstration of magic flexibility. *Nanotechnology* **2011,** *22*, 105705.

261. Abramson, A. R.; Tien, C.-L.; Majumdar, A., Interface and strain effects on the thermal conductivity of heterostructures: A molecular dynamics study. *Journal of Heat Transfer* **2002,** *124*, 963-970.

262. Li, X.; Maute, K.; Dunn, M. L.; Yang, R., Strain effects on the thermal conductivity of nanostructures. *Phys. Rev. B* **2010,** *81*, 245318.

263. Lee, G.-W.; Park, M.; Kim, J.; Lee, J. I.; Yoon, H. G., Enhanced thermal conductivity of polymer composites filled with hybrid filler. *Composites Part A: Applied Science and Manufacturing* **2006,** *37*, 727-734.

264. Yu, A.; Ramesh, P.; Sun, X.; Bekyarova, E.; Itkis, M. E.; Haddon, R. C., Enhanced thermal conductivity in a hybrid graphite nanoplatelet–carbon nanotube filler for epoxy composites. *Adv. Mater.* **2008,** *20*, 4740-4744.

265. Biercuk, M.; Llaguno, M. C.; Radosavljevic, M.; Hyun, J.; Johnson, A. T.; Fischer, J. E., Carbon nanotube composites for thermal management. *Applied physics letters* **2002,** *80*, 2767-2769.

266. Moisala, A.; Li, Q.; Kinloch, I.; Windle, A., Thermal and electrical conductivity of single-and multi-walled carbon nanotube-epoxy composites. *Composites science and technology* **2006,** *66*, 1285-1288.

267. Zheng, X. J.; Zhu, L. L.; Zhou, Y. H.; Zhang, Q. J., Impact of grain sizes on phonon thermal conductivity of bulk thermoelectric materials. *Applied Physics Letters* **2005,** *87*, 242101.

268. Yadav, G. G.; Susoreny, J. A.; Zhang, G.; Yang, H.; Wu, Y., Nanostructure-based thermoelectric conversion: an insight into the feasibility and sustainability for large-scale deployment. *Nanoscale* **2011,** *3*, 3555-3562.

269. Chen, G.; Dames, C., Thermal Conductivity of Nanostructured Thermoelectric Materials. In *Thermoelectrics Handbook*, CRC Press2005.

270. Borca-Tasciuc, D. A.; Chen, G.; Prieto, A.; Martin-Gonzalez, M. S.; Stacy, A.; Sands, T.; Ryan, M. A.; Fleurial, J. P., Thermal properties of electrodeposited bismuth telluride nanowires embedded in amorphous alumina. *Applied Physics Letters* **2004,** *85*, 6001-6003.

271. Brockway, L.; Vasiraju, V.; Vaddiraju, S., Compositional disorder and its effect on the thermoelectric performance of Zn_3P_2 nanowire–copper nanoparticle composites. *Nanotechnology* **2014,** *25*, 125402.

272. Brockway, L.; Vasiraju, V.; Sunkara, M. K.; Vaddiraju, S., Engineering Efficient Thermoelectrics from Large-Scale Assemblies of Doped ZnO Nanowires: Nanoscale Effects and Resonant-Level Scattering. *ACS Applied Materials & Interfaces* **2014**.

273. Zhi, C.; Bando, Y.; Terao, T.; Tang, C.; Kuwahara, H.; Golberg, D., Towards thermoconductive, electrically insulating polymeric composites with boron nitride nanotubes as fillers. *Advanced Functional Materials* **2009,** *19*, 1857-1862.

274. Ishida, H.; Rimdusit, S., Very high thermal conductivity obtained by boron nitride-filled polybenzoxazine. *Thermochimica Acta* **1998,** *320*, 177-186.

275. Yung, K. C.; Liem, H., Enhanced thermal conductivity of boron nitride epoxy-matrix composite through multi-modal particle size mixing. *Journal of Applied Polymer Science* **2007,** *106*, 3587-3591.

276. He, H.; Fu, R.; Han, Y.; Shen, Y.; Song, X., Thermal conductivity of ceramic particle filled polymer composites and theoretical predictions. *Journal of materials science* **2007,** *42*, 6749-6754.

277. Terao, T.; Zhi, C.; Bando, Y.; Mitome, M.; Tang, C.; Golberg, D., Alignment of boron nitride nanotubes in polymeric composite films for thermal conductivity improvement. *The Journal of Physical Chemistry C* **2010,** *114*, 4340-4344.

278. Chopra, N. G.; Luyken, R.; Cherrey, K.; Crespi, V. H.; Cohen, M. L.; Louie, S. G.; Zettl, A., Boron nitride nanotubes. *Science* **1995,** *269*, 966-967.

279. Han, W.-Q.; Wu, L.; Zhu, Y.; Watanabe, K.; Taniguchi, T., Structure of chemically derived mono-and few-atomic-layer boron nitride sheets. *Applied Physics Letters* **2008,** *93*, 223103.

280. Dean, C. R.; Young, A. F.; Meric, I.; Lee, C.; Wang, L.; Sorgenfrei, S.; Watanabe, K.; Taniguchi, T.; Kim, P.; Shepard, K., Boron nitride substrates for high-quality graphene electronics. *Nature nanotechnology* **2010,** *5*, 722-726.

281. Xue, J.; Sanchez-Yamagishi, J.; Bulmash, D.; Jacquod, P.; Deshpande, A.; Watanabe, K.; Taniguchi, T.; Jarillo-Herrero, P.; LeRoy, B. J., Scanning tunnelling microscopy and spectroscopy of ultra-flat graphene on hexagonal boron nitride. *Nat. Mater*. **2011,** *10*, 282-285.

282. Kim, P.; Shi, L.; Majumdar, A.; McEuen, P. L., Thermal Transport Measurements of Individual Multiwalled Nanotubes. *Physical Review Letters* **2001,** *87*, 215502.

283. Xiao, Y.; Yan, X. H.; Cao, J. X.; Ding, J. W.; Mao, Y. L.; Xiang, J., Specific heat and quantized thermal conductance of single-walled boron nitride nanotubes. *Phys. Rev. B* **2004,** *69*, 205415.

284. Touloukian, Y.; Powell, R.; Ho, C.; Klemens, P. *Thermophysical Properties of Matter-The TPRC Data Series. Volume 1. Thermal Conductivity-Metallic Elements and Alloys*; DTIC Document1970.

285. Lindsay, L.; Broido, D., Enhanced thermal conductivity and isotope effect in single-layer hexagonal boron nitride. *Phys. Rev. B* **2011,** *84*, 155421.

286. See, K. C.; Feser, J. P.; Chen, C. E.; Majumdar, A.; Urban, J. J.; Segalman, R. A., Water-Processable Polymer−Nanocrystal Hybrids for Thermoelectrics. *Nano Letters* **2010,** *10*, 4664-4667.

287. Reddy, P.; Jang, S. Y.; Segalman, R. A.; Majumdar, A., Thermoelectricity in molecular junctions. *Science* **2007,** *315*, 1568-1571.

288. Vasiraju, V. R. K.; Kang, Y.; Vaddiraju, S., Non-conformal Decoration of Semiconductor Nanowire Surfaces with Boron Nitride (BN) Molecules for Stability

Enhancement: Degradation-resistant Zn3P2, ZnO and Mg2Si Nanowires. *Physical Chemistry Chemical Physics* **2014,** *16*, 16150-16157.

289. Pal, R., On the Lewis–Nielsen model for thermal/electrical conductivity of composites. *Composites Part A: Applied Science and Manufacturing* **2008,** *39*, 718-726.
290. Elrod, U.; Luxsteiner, M. C.; Obergfell, M.; Bucher, E.; Schlapbach, L., Surface-chemistry of Zn_3P_2 single-crystals studied by XPS. *Applied Physics B-Photophysics and Laser Chemistry* **1987,** *43*, 197-201.
291. Rai, B. P., Cu_2O solar cells: A review. *Solar Cells* **1988,** *25*, 265-272.
292. Klesnar, H.; Rogl, P., Phase relations in the ternary systems rare-earth metal (RE)-boron-nitrogen, where RE. *High Temperatures. High Pressures* **1990,** *22*, 453-457.
293. Kurdyumov, A.; Ostrovskaya, N.; Pilyankevich, A.; Dubitskii, G.; Slesarev, V. In *Crystal structure of wurtzite-type boron nitride prepared at high static pressures*, Soviet Physics Doklady1976; p 402.
294. Eichhorn, K.; Kirfel, A.; Grochowski, J.; Serda, P., Accurate structure analysis with synchrotron radiation. An application to borazone, cubic BN. *Acta Crystallographica Section B: Structural Science* **1991,** *47*, 843-848.
295. Zhou, J.; Jin, C.; Seol, J. H.; Li, X.; Shi, L., Thermoelectric properties of individual electrodeposited bismuth telluride nanowires. *Applied Physics Letters* **2005,** *87*, 133109.
296. Wang, H.; Zhang, X.; Meng, X.; Zhou, S.; Wu, S.; Shi, W.; Lee, S., Bulk Preparation of Si–SiOx Hierarchical Structures: High-Density Radially Oriented Amorphous

Silica Nanowires on a Single-Crystal Silicon Nanocore. *Angewandte Chemie International Edition* **2005,** *44*, 6934-6937.

297. Satyala, N. T.; Krasinski, J. S.; Vashaee, D. In *Thermoelectric Properties of Mg2Si Doped with Bi and Al with Conductive Glass Inclusion*, Green Technologies Conference, 2012 IEEE, 19-20 April 2012, 2012; pp 1-5.
298. Sze, S. M.; Ng, K. K., *Physics of semiconductor devices*. 3rd ed.; Wiley-Interscience: Hoboken, N.J., 2007; p x, 815 p.
299. Martin, P.; Aksamija, Z.; Pop, E.; Ravaioli, U., Impact of Phonon-Surface Roughness Scattering on Thermal Conductivity of Thin Si Nanowires. *Physical Review Letters* **2009,** *102*.
300. Markussen, T.; Jauho, A. P.; Brandbyge, M., Surface-Decorated Silicon Nanowires: A Route to High-ZT Thermoelectrics. *Physical Review Letters* **2009,** *103*, 055502.
301. Luisier, M., Thermal transport and Matthiessen's rule in ultra-scaled Si nanowires. *Applied Physics Letters* **2013,** *103*, -.
302. Tavendale, A. J.; Pearton, S. J., Deep level, quenched-in defects in silicon doped with gold, silver, iron, copper or nickel. *Journal of Physics C: Solid State Physics* **1983,** *16*, 1665.
303. Sze, S. M., *Semiconductor devices, physics and technology*. Wiley: New York, 1985; p 38-39, 493-497.

APPENDIX A: THERMAL CONDUCTIVITY IN NANOWIRES

Matthiessen's rule

The thermal or electrical resistivity of a material is the sum of resistivities caused by several scattering processes if each of them were present independently.[298]

Hochbaum *et al.* showed that the introduction of roughness on the surface of the silicon nanowire can reduce the thermal conductivity of the nanowire nearly to its amorphous limit at room temperature.[102] The roughness on the nanowires reduces the phonon mean free path and thereby reduces the thermal conductivity. However, such a low conductivity is only possible if all the following scattering processes are included: transverse and longitudinal scattering, anharmonic phonon-phonon scattering, impurity scattering, boundary scattering and scattering due to roughness. All the contributions from the above scattering mechanisms can be combined using matthiessen rule to obtain the total thermal conductivity of the given material. Mathession rule was employed in many theoretical studies to show the combined effect of all the scattering processes, and it used to calculate the combined effect when the scattering mechanisms are independent of each other. Mathematical form of Mathession rule is as follows:

$$\frac{1}{\kappa_{total}} = \frac{1}{\kappa_{longitudanal}} + \frac{1}{\kappa_{transverse}} + \frac{1}{\kappa_{impurity}} + \frac{1}{\kappa_{boundary}} + \frac{1}{\kappa_{roughness}}$$

In the above formula all the scattering phenomenon except boundary and roughness scattering are geometry independent and are dependent on the properties of the material. The boundary scattering depends on the phonon wavelength (i.e. boundary scattering is more pronounced if the wavelength of the phonon is small) and the number of boundaries present in the chosen sample. Phonon scattering due to roughness of the nanowire is dependent on the diameter (D) and the rms roughness value (Δ) as shown in Figure 46. The thermal conductivity dependence is mathematically shown as follows.[299]

$$\kappa_{roughness} \propto \left(\frac{D}{\Delta}\right)^2 \ for \ \frac{D}{\Delta} < 20$$

$$\kappa_{roughness} \propto \left(\frac{D}{\Delta^2}\right) \ for \ \frac{D}{\Delta} > 20$$

The effect of surface roughness was seen to be highest for nanowires with diameters less than 50nm. The effect of scattering due to roughness is more pronounced when the dimensions of the roughness on the surface is comparable to the phonon velocity. When a phonon hits a rough surface, the phonon is scattered by the rough surface and some time is lost before it enters the wire, thereby localizing the phonons. The contribution of surface roughness to thermal resistivity increases by 7 times from a nanowire diameter of 115 nm to 22 nm. The effect of surface roughness also varies with the frequency of the incident phonons, low frequency phonons are not scattered as much as the medium frequency phonons.[74, 300] There is a certain range of phonons which are scattered more than other due to surface roughness. Surface roughness scatter is lower in low energy phonons. Martin et al calculated the phonon average life time to be 15s or roughness of 3A and characteristic length of 6nm. The average lifetime decreases with increase in surface roughness as follows lifetime = k* Δ^{-2}. The thermal phonon-surface scattering rate follows Bose-Einstein statistics.[299]

The scattering rate in each mechanism is given as follows:

Table 4 Various scattering mechanisms and their corresponding scattering rate dependence on temperature and frequency[298]

Phenomenon	Scattering Rate (τ^{-1})
Longitudinal Phonon-Phonon Scattering:	$= B_L T^3 \omega^2$
Transverse Phonon – phonon scattering	$= B_T T e^{-\theta/T} \omega^2$
Impurity Scattering	$= C\omega^4$
Boundary Scattering	$= v_i D^{-1} \sqrt{1 + 4\omega c_i / v_i}$

<u>Deviation from mathession rule:</u>

Mathieu Luisier, showed that mathession rule at nanoscale gives the same behavior as obtained by molecular dynamic simulations but thermal conductivity obtained using mathession rule underestimates the thermal conductivity by 18% in silicon nanowires.[301] The phonon scattering due to roughness and annharmoic oscillations are not independent scattering mechanisms and are dependent on each other. The reduced thermal conductivity due just the roughness of the nanowires is attributed to the presence of non-propagating phonon modes (20 – 25 mev) with a quasi-null velocity, but a fraction of these phonons, due to the anharmonic phonon-phonon interactions decay into lower energy phonons

(10mev) but with higher velocity and thereby contribute to the thermal conductivity. Therefore the two scattering mechanism cannot be treated independently. The assumption in most of the calculations is that the boundary scattering process is elastic in nature and no phonons are emitted into surrounding environment.

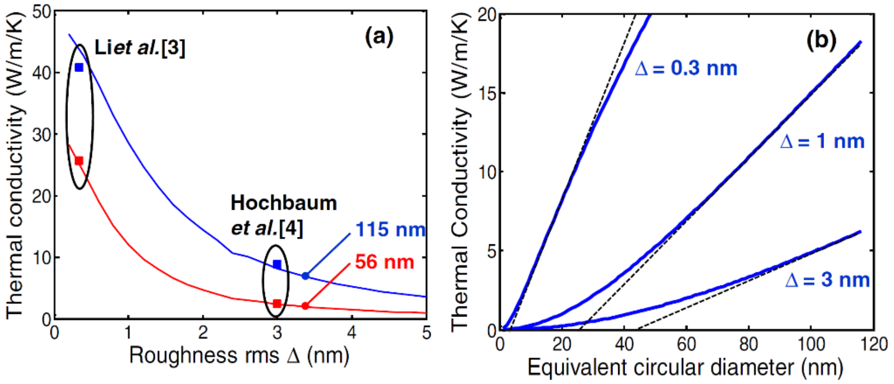

Figure 46 Dependence of thermal conductivity on a) roughness of the nanowire for a given nanowire diameter and b) Diameter of the nanowire for a given roughness value.[299]

Temperature dependence on thermal conductivity

The thermal conductivity of material is given as follows

$$\kappa = \frac{1}{3} C \upsilon \tau$$

At low temperatures the thermal energy is low so there are fewer phonons. Due to this the phonon-phonon interaction/scattering is not prominent, in addition, the phonons have a large wavelength therefore interaction with imperfections and boundaries is also minimum, thereby having large mean free path of phonons.[298] At high temperatures the phonon-phonon scattering increases due to increased number of phonons. Also due to the shorter wavelength of phonons (due to high thermal energy) the impurity scattering increases. Another effect, which must be considered to calculate the thermal conductivity, is heat capacity, which decreases for temperatures below Debye temperature and eventually goes to zero. For most materials as the temperature decreases the thermal conductivity increases and then starts to decreases after certain temperature and drops to zero. The temperature at which thermal conductivity is maximum is $\theta_D/10$ where θ_D is the Debye temperature in Kelvin, for silicon θ_D is 645K.

Widemann-Franz law

This law states that the electronic thermal conductivity is directly proportional to the electrical conductivity of the material and is given by

$$\kappa_e(T) = L * T * \sigma(T)$$

Here κ_e = electronic thermal conductivity, T = temperature, σ = electrical conductivity and L = the Lorentz number. This law implies that the electrical conductivity and electronic thermal conductivity cannot be tuned independently. Therefore the zT could be increased by reducing the lattice thermal conductivity without adversely affecting the electrical conductivity.

Phonon and electron confinement in silicon nanowires

The average wavelength of an acoustic phonon at room temperature is 1nm and mean free path is on the order of 200nm. The average wavelength decreases as temperature increases. Prasher *et al.* showed that the bulk to 1D transition at 6K and 24 k occurs in nanowires of diameters 10.8 and 2.7 nm.

Electrons and acoustic phonons are confined in two dimensions in silicon nanowires. Mobility decreases with decreasing cross section and the rate of decrease increases with decreasing cross section. Silicon oxide is a soft acoustic material and the phonon group velocity decreases into half compared to that of silicon.

Table 5 Physical and electronic properties of magnesium silicide.[97, 98, 297]

Phonon mean free path	10 nm
Electron mean free path	1 – 2 nm changes with doping (decreases with increased doping)
Debye temperature	160 C
Density	1.88 g/cm^3
Band gap	Indirect band gap of 0.74ev
Melting point	1102 C
Heat capacity at RT	67.87 J/mol/K

APPENDIX B: ROLE OF CONTAMINATION IN SILICON NANOWIRES

Unintentional contamination in silicon nanowires during their growth or synthesis leads to a change in their electronic properties. Silicon is an indirect band gap material with a band gap of 1.12eV. Contamination of silicon nanowires leads to the formation of deep level defects as shown in Figure 47. Silver doping leads to formation of a acceptor level defect at 0.48ev from the valence band.[302, 303] As the seebeck coefficient, electrical conductivity and even the thermal conductivity in a semiconductor depend on the band gap and the fermi level position, unintentional contamination would lead to unpredictable changes in these properties.

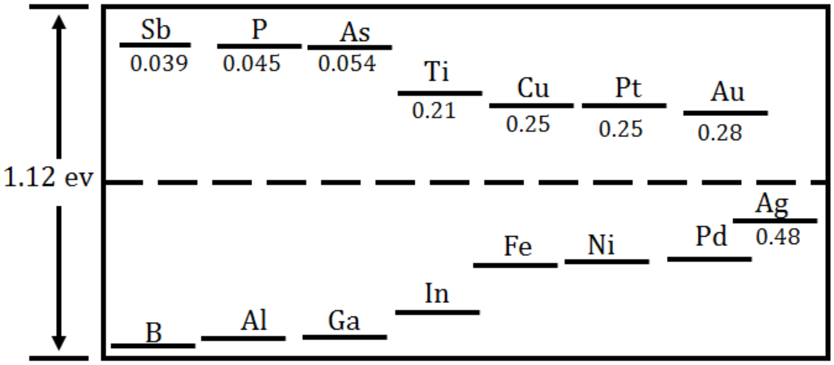

Figure 47 Band diagram of silicon showing the defect states created in the forbidden region on addition of various impurities.[302, 303]